Understanding Changes in Precipitation, Wildfires, and Possible Governing Factors over Central Equatorial Africa

by

Yan Jiang

A Dissertation

Submitted to the University at Albany, State University of New York

in Partial Fulfillment of

the Requirements for the Degree of

Doctor of Philosophy

College of Arts and Sciences

Department of Atmospheric and Environmental Sciences

2022

ABSTRACT

Tropical rainforests are global epicenters of biodiversity and modulators of climate. A long-term drying trend has occurred in the Congo Basin since the 1980s and this raises great concerns for sustaining the Congolese rainforest and local rain-fed agriculture. Motivated by documented rainfall changes and the need to improve understanding of main factors influencing precipitation variability and changes in Central Equatorial Africa (CEA), this dissertation conducts synthesized studies on 1) quantifying variations in precipitation seasonality by focusing on dry season duration, 2) estimating cascading wildfire risks associated with changes in precipitation patterns, and estimating impacts of 3) the tropical Indian Ocean and 4) rainforest evapotranspiration (ET) on precipitation.

First, combining multiple datasets of precipitation, vegetation greenness, canopy water content and photosynthesis, a trend analysis is conducted to assess variations in dry season length (DSL). The boreal summer dry season (mainly during June-August) has become longer in the Congo Basin over the period 1979-2015. The onset of the dry season has become earlier based on precipitation data, which was associated with the strong drying trend during April-June. A delayed end of the dry season was indicated by vegetation products and was attributed to a prolonged deficit in root-zone soil moisture during the dry season.

Second, using the latest satellite-derived burned area products and an advanced labeling method, changes in total burned area, frequency, and size of different fire categories are quantified over Central Africa. The random forest model is applied to identify leading factors regulating wildfires and their changes. Wildfires commonly occur during dry seasons. Total burned area has declined by ~1.3% yr^{-1} from 2003-2017, particularly in northern Central Africa. This decline was due to significant decreases in both fire frequency and size, particularly for large fires (>100 ha).

Declined burned area mainly occurred in savannas and grasslands and was attributed to decreased fuel load, which was associated with decreased rainfall and increased DSL. Nevertheless, burned area has increased in the southern edge of the Congolese rainforest, which might result from reduced rainfall and warmer temperature.

Third, the association between the Indian Ocean Dipole (IOD) and CEA rainfall is estimated. Combining partial correlation and composite analyses, IOD's independent impact and its combined impact with the Madden-Julian-Oscillation (MJO) on precipitation are identified. There is a significant positive correlation between CEA rainfall and the IOD during September-December (SOND) over the period 1981-2019. During a positive IOD events, the warmer western Indian Ocean enables stronger convection and a wetter troposphere to enhance rainfall amount and frequency over CEA. An increase in CEA rainfall has been observed since the 1990s and is concurrent with the increasing correlation between IOD and rainfall. The increasing IOD index might contribute to much of the rainfall trends over the western, southern, and eastern Congo basin.

Last, the impact of rainforest ET on precipitation over the Congo Basin is estimated by using satellite isotopic data and running the International Centre for Theoretical Physics Regional Climate Model (RegCM4.9.3). Sensitivity experiments with ET perturbations via prescribed changes in leaf area index (LAI) and stem area index (SAI) are conducted to quantify precipitation sensitivity to ET changes. Estimates by satellite data indicate that ET contributes to atmospheric moisture for precipitation and sustains moisture convergence over the Congo Basin during March-May and June-August. Simulated precipitation increases (decreases) linearly with enhanced (reduced) ET over the Congo Basin. The sensitivity of precipitation to ET changes is mainly attributed to the sensitivity of precipitation intensity to ET. Model simulations suggest that ET

affects precipitation by modulating atmospheric moisture distribution in the lower troposphere. The results imply a positive feedback loop for declined ET to exacerbate the aridity.

ACKNOWLEDGMENTS

It still feels surreal how my dream to become a climate scientist started from a normal day in my last summer of high school. I turned to my parents and thrilly acclaimed "*I want to become a cool climate scientist and save the world!*", right after watching the movie "*The day after tomorrow*". Nine years later, though I start to wonder whether people really need me to save the world, I am more excited to notice how far I have reached and how close I am to my goal. This journey would never be achieved without supports from my mentors, friends, and family.

First and foremost, I would like to thank my advisor, Dr. Liming Zhou for his support and guidance through my doctoral study. Everyone can easily dream, it is you who taught me how to dream. You inspired and led my very first research project in my graduate school when I felt totally lost as entering a brand-new place and field. I can never stop appreciating your patience with my extremely poor writing skills at the beginning, as I still remember your help on countless revisions and tiny details of my very first published paper. You opened my mind to research and taught me how to raise and solve questions. The mindsets for research and life that I learned from you are always the most precious knowledge I gained in my life. I also want to appreciate your endless support and encouragement for me to embrace new ideas and challenges in research and my career, where I obtained so many skills and opportunities. I am absolutely blessed to have been advised by you.

I would like to thank the remainder of my committees: Drs. Aiguo Dai, Brian Rose, and Robert Fovell for their insights and guidance on my dissertation. I completed the majority of my graduate-level courses tutored by members of my PhD committees. I learned how to run climate models from Dr. Brian Rose. I obtained insights on climate dynamics from Dr. Aiguo Dai. I studied the details of different model schemes from Dr. Robert Fovell. My discussions with each of these

fantastic scientists helped me build up the structure of my thesis and guided me to address critical research questions. I would not have completed this dissertation without their mentorship.

I want to extend my appreciation to the rest of the faculty, staff, and students at the Department of Atmospheric and Environmental Science (DAES). It is difficult for me to name all colleagues and friends who have enlightened my graduate school life here. I am so lucky to study and work in a warm, kind, supportive, and diverse atmosphere. I obtained multiple opportunities to train my leadership and advisement skills and received so much helpful feedback and suggestions on my research from the Climate Group Meeting. I want to particularly acknowledge Dr. Paul Roundy's guidance on one of my research projects and Kevin Tyle's help to set up the model used in my dissertation.

I would also like to thank friends and fellow students for their companies and help at Albany. I want to particularly thank Dr. Wenjian Hua, a previous senior member of our group, for his guidance and help on my research. My research siblings Geng Xia, Ajay Raghavendra, Kathrin Alber, Stephen Solimine, Alejandro Ayala, Li Zhuo help set a helpful and supportive team for me to learn new skills and share research. In particular, Geng and Ajay are the very first friends I made at Albany and who I have grown the closest to through my study at DAES. I would like to thank my office mates at ES330, Cameron Rencurrel, Dylan Card, Emily Paltz, Krista Dotterer, other friends Di Chen, Fangze Zhu, Heather Sussman, Minghao Zhou, Shenzhen Chen, for sharing celebrating moments and happiness, and my good friends Bo Yan, Lucy Paltz for their supporting during the Covid Era.

I also want to thank Dr. Song Yang, the advisor of my undergraduate thesis from Sun Yet-Sen University, who was incredibly encouraging of me when I applied for the PhD program and felt confused about my future. As the first advisor of my research, he did not only teach me basic

research and presenting skills, but also shared his academic insights and career advice with me. Without his inspiration and encouragement, I would not be able to take my step and make it here today.

Finally, I will save my gratitude to my family. My parents have been sending endless support and encouragement to me. They have always been staying by my side for sorrow and exciting moments, listening to all my crazy thoughts and ideas, supporting my decisions, praising my achievements, embracing my insufficiency, and telling me that "You can do it as always!" when I feel stressed and anxious. With their love and encouragement, I am confident and brave enough to explore the unknown, dream the unreal, reach places where I have never been.

This research was supported by the National Science Foundation Awards (NSF AGS-1535426 and AGS-1854486).

Statement of Publication

The materials in Chapter 2, Chapter 3, and Chapter 4 have been peer-reviewed and published. Materials from the articles were reproduced with permission from the publisher. Applicable electronic permissions are attached in Appendices. The articles were incorporated into this dissertation as the work from each article is an integral component of the dissertation. Minor changes were made to ensure the format and continuity of the dissertation.

Since the author of this dissertation was the lead author of the publication, it is appropriate to include the articles in this dissertation. The articles can be accessed through the following citations:

Jiang, Y., Zhou, L., Tucker, C.J., Raghavendra, A., Hua, W., Liu, Y.Y. and Joiner, J., 2019: Widespread increase of boreal summer dry season length over the Congo rainforest. *Nature. Climate. Change*, **9**, 617-622. **Used with permission**.

Jiang, Y., Zhou, L. and Raghavendra, A., 2020: Observed changes in fire patterns and possible drivers over Central Africa. *Environmental Research Letters*, **15**, 0940b8. **Used with permission under the CC BY license**.

Jiang, Y., Zhou, L., Roundy, P.E., Hua, W. and Raghavendra, A., 2021: Increasing Influence of Indian Ocean Dipole on Precipitation over Central Equatorial Africa. *Geophysical Research Letters*, **48**, e2020GL092370. **Used with permission**.

LIST OF TABLES

LIST OF FIGURES

TABLE OF CONTENTS

Chapter 1 Introduction

1.1 Background and Motivation

Precipitation is an essential part of the Earth system and the water cycle. Variations in precipitation might arise from, either single or a combination of, distinctive shifts in large-scale atmospheric circulations, disturbances in atmosphere-land-ocean interactions, and external forcing (Held and Soden 2006; Seidel et al. 2007; Guan et al. 2018). Chronic and acute changes in precipitation would shed tremendous impacts on natural ecosystems and societies. Due to precipitation's geographic dependence, and complicated and various biogeophysical and biogeochemical interactions at different spatial and temporal scales (Stott et al. 2010; Marvel and Bonfils 2013; Tan et al. 2015), changes in precipitation are among the most important yet least well-understood questions.

Central Equatorial Africa (CEA) is one of three key convection regions on the planet and the epicenter of biodiversity. The African continent holds the world's second largest rainforest and one third of the global dry and semi-dry ecosystems, which are highly constrained by and sensitive to variabilities and changes in precipitation patterns (Engelbrecht et al 2007; Good and Caylor 2011; Fauset et al 2012; Guan et al 2014). With the great richness in various biomes, these ecosystems are important to millions of people by providing food, building materials, medicines, and other products (Ellwood and Foster 2004; Lawrence et al. 2005; Prance 2002; Lewis 2006). What's more, rainforest evapotranspiration (ET) contributes to rainfall, alters cloud cover and soil moisture, and could even affect climate at both global and regional scales (Betts 2004; Chagnon et al. 2004; Delire et al. 2004). The Congo Basin provides crucial freshwater for agriculture development and hydropower generation in the majority of African countries, where the population is expected to increase about 50% by 2030 (Lumbroso et al. 2015; UNDESA 2017;

Sridharan et al. 2019). Thus, changes in precipitation patterns would not only directly affect the regional hydrological cycle and ecosystems but can also hurt rain-fed agriculture and the accessibility to electricity power across multiple African countries.

The global atmosphere is undergoing a period of rapid human-driven change (IPCC 2002). Some large-scale changes in precipitation, inferred from theoretical deduction, observations, and climate model predictions, are expected in a warming world (Stott et al. 2010). Though a conventional paradigm characterizes changes in rainfall patterns as 'wet-gets-wetter' and 'warmer-gets-wetter' (Held and Soden 2006; Chou et al. 2009; Allan et al. 2010; Seager et al. 2010), tropical rainforests regions can span and experience a wide range of rainfall variability and changes (Malhi and Wright 2004). Due to a relative paucity of meteorological data and limited long-term records available in remote tropical rainforests, the answers to "how have precipitation patterns varied in CEA" were once ambiguous with little agreement (Malhi and Wright 2004; Washington et al. 2013). Recently, there has been a surge in research focusing on hydroclimate and its changes over CEA (Vizy and Cook 2012; James et al. 2013). In particular, an exclusive long-term drying trend has been observed in the Congo Basin rather than in the Amazon and Southeast Asia, home to the first and third largest rainforests on Earth and the two intensively studied rainforests related to climate change and deforestation (Malhi and Wright 2004; Asefi-Najafabady and Saatchi 2013; Zhou et al. 2014). This drying trend raises big concerns about sustainability for indigenous ecosystems, biomes, and local societies which are highly dependent on precipitation. It highlights the need and urgency to detect and attribute changes in precipitation characteristics, to explore relevant physical mechanisms, to better understand regional climate responses to global warming, and ultimately to improve climate predictions and risk assessments over the CEA.

1.2 Literature Review

1.2.1 Observed Long-term Changes in Precipitation in the Congo Basin

Compared with other tropical rainforests, the Congolese rainforest is drier, more fragmented, and with a higher percentage of semi-evergreen trees (Adams 1998; Ashton et al. 2012; Potapov et al. 2017). It may be more tolerant to short-term rainfall disturbances but would reach a critical tipping point and then shift to a lower-biomass forest easier once a long-term drought happens (Lewis 2006; Enquist and Enquist 2011; Fauset et al. 2012; Asefi-Najafabady and Saatchi 2013). Nevertheless, the Congo rainforest receives less academic and public attention than rainforests in the Amazon and Southeast Asia. Impacts of the changing climate on hydroclimate and ecosystems in the Congo are less addressed or even downplayed (Atyi et al. 2019; White et al. 2021). During the satellite data era, there are increasing studies on quantifying hydroclimatic changes and responses of African forests to the changing climate. In particular, a continuation of the drying trend since around the 1980s has been confirmed in CEA (Zhou et al. 2014; Hua et al. 2016).

Robust widespread warming and drying trends have been identified over CEA during 1960-1998 based on available gauge observations. The drying trend was concurrent with a steadily intensifying dry-season aridity and became strong since the mid-1970s (Nicholson et al. 2000a; Malhi and Wright 2004). Combining gauge observation records and satellite observation, this documented drying trend continued into the 2010s (Asefi-Najafabady and Saatchi 2013; Zhou et al. 2014; Hua et al. 2016). Newly available satellite datasets provide efficient proxies to measure vegetation and thus its responses to the long-term drying trend. Previously, only forests near the savanna boundary in West Africa and in fragmented landscapes of the northern Congo Basin showed canopy disturbances in response to the strong drought-induced water deficit (Asefi-Najafabady and Saatchi 2013). Using the latest satellite-derived datasets measuring vegetation

greenness, productivity, terrestrial water context via independent sensors, widespread and continuous decreases in plant greenness, photosynthetic capacity, and terrestrial water in the Congo Basin have been observed over much of the Congo Basin (Zhou et al. 2014).

Multiple climate simulations have predicted continuous drying trends or even more severe and frequent droughts in Central Africa in the next 30-90 years (Kumar et al. 2004; Bosilovich et al. 2005; Dai 2013). The relatively drier Congolese rainforest might have adapted to short-term droughts and temporal water deficit. However, the long-lasting water deficit may ultimately alter forest species composition and structure and could further affect biodiversity and carbon storage (Enquist and Enquist 2011; Fauset et al. 2012; Zhou et al. 2014). These results raise big concerns for the scientific community and highlight the priority to address some key scientific questions concerning the Congo rainforest including changes in precipitation, wildfire risks, and possible remote and local factors affecting precipitation variability and changes in CEA.

1.2.2 Precipitation Seasonality

To fully characterize the long-term drying trend in the Congo Basin, it requires not only the consideration of annual or seasonal total rainfall, but also a comprehensive estimation of variations in the magnitude, timing, and duration of rainfall (Feng et al. 2013; Guan et al. 2014). In particular, the dry season, during which precipitation is relatively lower than the annual mean state, is closely connected with annual rainfall pattern and drought occurrence. It is crucial to sustain vegetation composition and distribution as well. Rainy/dry season length determines the favorable conditions of soil water supply to support plant growth (Guan et al. 2018), affects fire season and fuel load, and possibly imposes extra physical constraints on ecosystem structure and dynamics (Bond et al. 2005; Sankaran et al. 2005; Archibald et al. 2009; Lehmann et al. 2014). In addition, precipitation

seasonality has an important indication for society. The timing and duration of rainfall activity directly affect the management of water resources and the development of rain-fed agriculture (Kumar 2013). What's more, changes in dry/rainy season length have been found to induce more dramatic ecosystem responses compared with similar changes in rainfall frequency and intensity (Guan et al. 2014).

Changes in rainfall seasonality have been found in various tropical regions and have been projected to continue for the future climate (Biasutti and Sobel 2009; Feng et al. 2013; Seth et al. 2013). Strong increases in the variability of seasonal rainfall magnitude and timing have been identified in northeastern Brazil. For tropical Africa, considerable decreases in the rainfall magnitude and duration have been observed in West Africa over 1930-1990 (Feng et al. 2013). The results were consistent with the previously detected decrease in precipitation seasonality due to the shortening rainy season and decreased rainfall frequency (Biasutti and Sobel 2009; Shongwe et al. 2009). Whereas CEA showed a significant increase in the variability of seasonal timing, the full picture of changes in dry/rainy season length and intensity is still missing.

The bimodal rainfall pattern is a distinct characteristic of precipitation activity in CEA. As the rain belt moves northward and southward periodically, CEA experiences two rainy seasons during March-May (MAM) and September-November (SON), and two dry seasons during June-August (JJA) and December-February (DJF). This unique precipitation seasonality is critical for maintaining the complicated and widely varied vegetation types ranging from moisture rainforest to woody savannas and grasslands in CEA. A strong decrease in precipitation during April-June has been observed since the 1980s (Zhou et al. 2014; Hua et al. 2016). Possibly, the decrease in seasonal rainfall may modify the transpiration period and regional carbon budget and boost the competitive advantage of deciduous species at the expense of evergreen rainforests (Yoshifuji et

al. 2006; Enquist and Enquist 2011; Feng et al. 2013). Hence, the very first objective of the dissertation is to address potential changes in dry season length and intensity along with the long-term drying trend.

1.2.3 Wildfire Risks in CEA

Fires are an integral part of the Earth system, interacting with climate, ecosystem, and human activities. Hot, dry, and windy conditions typically lead to severe fires (Jolly et al. 2015). Humans influence fire regimes directly by igniting and suppressing fires but also indirectly by modifying the vegetation structure and composition (Lasslop and Kloster 2017). On the other hand, frequent fires are integral for savannas and grasslands, supporting a large range of endemic species, large mammals, and other wildlife (Scholes and Archer 1997). Inter-annual variability in wildfire extent largely drives variations in global carbon dioxide and aerosols (Patra et al. 2005; Schultz et al. 2008). Thus, understanding variations of fire regimes not only has implications for societal and economic developments but is also an urgent issue for studies on fire-climate-ecosystem interactions and fire prediction and management.

Central Africa is one of the hot spots of wildfires and contributes to ~70% of global burned area (Andela and van der Werf 2014). As the dry season length increases when moving away from the equator, the highest annual burned area emerges in savannas with intermediate levels of precipitation and productivity (van der Werf et al. 2008). Fire plays an important role to sustain savannas by managing fuel loads and the competition between woody and herbaceous species. It is also a powerful tool to recycle nutrients to conserve grasslands that support grazing, wildlife, and agriculture purposes (Shaffer 2010).

Though fires are mostly human ignited, precipitation patterns largely govern the occurrence of fires and thus influence interannual variability of wildfire activity. Wildfires commonly occur during dry seasons. Precipitation amount during precedent rainy seasons directly affects vegetation productivity available for burning. Thus, changes in precipitation patterns may modulate year-to-year variations in ignition efficiency and fire size (Andela et al. 2017). Increased precipitation can enhance active fires by increasing plants productivity and flammable fuel. It can also limit burned area by shortening the dry season length (van der Werf et al. 2008; Archibald et al. 2010). Wildfires are usually blocked out of the dense and moist rainforests. Nevertheless, given the continuous drying trend in CEA and gradually fragmented Congolese rainforest, it exerts the jeopardization of increasing wildfires licking into rainforests and enhances the possibility to break the balance sustaining African savannas. Thus, the question regarding how wildfires have changed related to precipitation variations needs to be addressed.

1.2.4 Possible Factors Influencing Precipitation in CEA

Precipitation in CEA is sustained by both moisture sources remotely from surrounding oceans and recycled moisture locally from the rainforest (Dominguez and Kumar 2008; Dominguez et al. 2008). When and to what extent does each component impact precipitation activity are important questions. Answers to these questions will provide insights into regulations on precipitation variability and changes over CEA and facilitate understanding of regional climate dynamics.

Oceans are suggested to largely affect regional precipitation by exerting a major influence on atmospheric circulation patterns and moisture advection (Dyer et al. 2017). Tropical oceanic conditions, particularly seas surface temperatures (SSTs), have been highlighted as the major driver for rainfall variations over Africa and other regions (Giannini et al. 2003; Lu and Delworth

2005; Hoerling et al. 2006; Shanahan et al. 2009; Dai 2013; Hua et al. 2016). The interannual variability of the tropical Pacific Ocean, the El Niño Southern Oscillation, is negatively correlated with rainfall anomalies in western equatorial Africa during February-August (Balas et al. 2007). It suggests that the tropical Indian Ocean contributes about 21% of the moisture for both rainy seasons in the Congo Basin (Dyer et al.2017). The interannual variability of the tropical Indian Ocean, the Indian Ocean Dipole (IOD), is associated with reduced rainfall during the dry season over Central Africa (Otto et al. 2013). In addition, high tropical Atlantic SSTs can enhance Central African rainfall in dry seasons (Otto et al. 2013).

The drying trend during April-June in CEA has been associated with declined moisture transported from the tropical Indian Ocean in this season (Hua et al. 2016). The suppressed ascent over the basin was induced by the westward extended Walker Circulation over the Indo-Pacific Ocean, which was caused by the La Niña-like SST anomalies during 1980-2014 (Ma and Zhou 2016; Hua et al. 2018). The weaker meridional pressure gradient between the cold Atlantic subtropical high and the Sahara low also contributed to a weaker monsoon flow during boreal spring and summer (Hua et al. 2016). Impacts of the tropical Indian Ocean on CEA rainfall in the SON rainy season were less clear. In addition, active interactions among different tropical oceans have been noticed (Cai et al. 2019), which can enhance or suppress their individual effects on precipitation. And significant interannual variations in tropical oceans including the tropical Indian and Pacific Oceans have been observed during the past decades (Cai et al. 2013). This might indicate secular associations among precipitation and different oceanic modes. A better analysis of tropical oceanic impacts on CEA rainfall embracing these considerations is thus required.

While rainforest's ET also contributes to local precipitation, as the annual mean recycling ratio of moisture is about 28% in the Congo Basin (Dyer et al. 2017), its influence on precipitation

pattern and feedbacks on precipitation disturbance have not been well studied yet. Terrestrial ET is a critical variable in the water cycle, which serves as a diagnostic of ecosystem activity and is expected to be influenced by atmospheric and precipitation variabilities (Miralles et al. 2014; Martens et al. 2018). It thus acts as a nexus between the water and carbon cycle (Le Quéré et al. 2016; Cheng et al. 2017). About 117,600 km^3 of water falls onto the terrestrial surface as precipitation each year, less than 45,800 km^3 (39%) water comes from the ocean while the majority of water (71,800 km^3, or 61%) derives from the land (Trenberth et al. 2011; Schneider et al. 2017). According to the conservation of water in Earth system, variations in precipitation may result in similar disturbances in ET (e.g., decreased precipitation would result in reduced ET) (Rosenfeld et al. 2008). Previous research has implied that increasing frequency and severity of droughts and floods appear to follow disruptions in the terrestrial water cycle (Millán 2014; Hirsch and Archfield 2015; Erfanian et al. 2017).

Observations in the tropics show that evergreen forests maintain relatively high humidity year-round including dry seasons (Bunyard 2014). Recent studies indicate that the ability to maintain ET in the dry season plays a key role in conducting shallow convection and determining the dry-to-wet season transition in the southern Amazon (Wright et al. 2017). A novel theory—the 'biotic pump'—suggests that ET can exert a major influence on atmospheric dynamics by developing lower-pressure zones to actively drive moisture upward (Makarieva et al. 2013). In general, reduced or degraded forests often correlate with some declines in rainfall and cloud cover. In this way, positive feedback may arise between the vegetation and precipitation. However, interactions between vegetation and precipitation are hard to quantify due to the lack of direct detections (Sheil 2018). The emerge of global-scale satellite measurements and advanced physical climate models

with improved parameterization of vegetation functions and dynamics makes an integral establishment of ET-precipitation interaction in CEA possible.

1.3 Research Questions & Organization of Dissertation

Motivated by the long-term drying trend observed in the Congo Basin, the dissertation aims to quantify changes in precipitation seasonality and wildfires and estimate the influences of factors from remote tropical oceans and local rainforest ET on precipitation variability and changes in CEA. To address the objectives of this dissertation, the following research questions will be addressed herein:

1. Whether and how has the dry season length changed in the Congo Basin along with the long-term drying trend?
2. How have wildfires varied in Central Africa considering significant changes in precipitation amount and dry season length?
3. What is the association between the tropical Indian Ocean and CEA rainfall?
4. How does rainforest ET impact precipitation activity in CEA?

The dissertation comprises 6 chapters. Chapter 1 contains the background and literature reviews on precipitation changes, precipitation seasonality and wildfires in CEA, possible regulations of tropical SSTs and rainforest ET on regional hydroclimate, and key questions requiring attention and research. Analyses on trends in the dry season length using various precipitation and vegetation products are presented in Chapter 2. Variations in burned area, frequency and size of different fire categories are fully quantified in Chapter 3. The tropical Indian Ocean's independent effect and combined impacts with the Madden-Julian-Oscillation on CEA

rainfall are analyzed in Chapter 4. In Chapter 5, sensitivity experiments with different ET disturbances are conducted via a regional climate model to quantify precipitation's response to ET changes and elucidate related physical mechanisms. Each of these chapters includes an introduction, descriptions of used datasets and methods, and results and discussions addressing the research question raised. Final conclusions and potential future work are outlined in Chapter 6.

Chapter 2 Widespread Increase of Boreal Summer Dry Season Length over the Congo Rainforest

2.1 Introduction

One distinct feature of tropical rainforest is the seasonal transition between dry and wet seasons. In the tropics, dry seasons represent periods with low rainfall and coincide with the seasonal shift of the rain belt over the course of the year (Nicholson 2018a). Dry season length (DSL) strongly influences tropical rainforest vegetation and is largely determined by precipitation patterns (Lewis 2006; Engelbrecht et al. 2007). Tropical rainforests are often considered as light-limited rather than water-limited given to persistent cloudiness and adequate water availability (Wright and Van Schaik 1994). Previous studies based on in situ and satellite observations over the Amazon suggested that peak photosynthesis coincides with peak of irradiance over humid rainforest in the dry season (Wright and Van Schaik 1994; Huete et al. 2006). Photosynthesis continues because the deep roots of trees can access ground water, allowing them to grow during the sunnier and drier part of the year (Huete et al. 2006). However, soil moisture becomes a limiting factor due to enhanced evapotranspiration and low rainfall as the dry season progresses, making tropical rainforests water-limited rather than light-limited (Guan et al. 2015). Any large change in rainfall seasonality that modifies the DSL and intensity, rainfall amount and insolation availability may influence the photosynthesis and productivity of a tropical rainforest.

Dry season duration is closely related to the frequency of droughts and affects the composition of local vegetation. Short-term droughts have immediate impacts on vegetation greenness. Three major droughts in 2005, 2010, and 2016, occurred in the Amazon, causing decreases in the water level of the Amazon River and in forest photosynthetic capacity (Marengo et al. 2008; Marengo et al. 2011; Erfanian et al. 2017). The dry season has also increased owning to its delayed end since

1979 (Fu et al. 2013). A more intense and longer dry season will enhance the frequency and intensity of short-term droughts and eventually alter the distribution and structure of forest vegetation (Fauset et al. 2012).

The Congo Basin has experienced a long-term drying trend. Consequently, forest browning, reduced canopy water content and decreased rainfall have been detected by multiple satellites in recent decades (Zhou et al. 2014; Hua et al. 2016). However, changes in dry season duration have never been studied and are poorly understood in the Congolese rainforest. Unlike the Amazon, the Congo has a drier climate with less annual rainfall, more fragmented forest surrounded by tropical savannas with high fire counts and a higher percentage of semi-deciduous vegetation. Therefore, the Congo rainforest is thus more sensitive and less resilient to climate changes (Hirota et al. 2011). The Congolese rainforest might be tolerant to short-term rainfall reduction, but long-term drying may result in a transition from higher-biomass and closed-canopy forests to lower-biomass and open-canopy forests (Zhou et al. 2014). Hence, variations in the DSL over the Congo have important ecological, societal, and climate implications. Furthermore, previous studies on DSL changes in the Amazon were based on analyses from the hydrological perspective only, while little attention was paid to the ecological perspective (Fu et al. 2013). Here we analyzed the DSL changes over the Congo Basin from both hydrological and ecological perspectives.

2.2 Data and Methods

2.2.1 Study Region

One difficulty in studying the DSL variations over the Congo is the complicated seasonality of precipitation. The seasonality varies with distance to the equator and along a west-to-east gradient. A zonal strip (4°N-4°S) extending over equatorial Africa is identified as a region of

bimodal precipitation (Fig. 2.1a). Peak rainfall in the bimodal region occurs during transitional seasons, corresponding to the northward and southward passages of the rain belt (Figs. 2.1b-e). This study focuses on the Congo Basin (12°E-32°E, 5°N-6°S) during the June-August (JJA) dry season given the long-term drying trend observed in equatorial Africa during the pre-dry season (April-June, AMJ) (Hua et al. 2016), which is expected to affect the following dry season. The study domain is carefully chosen to cover the contiguous forested area with similar precipitation patterns and limited anthropogenic and orographic influences (Figs. 2.1f-g, 2.2).

2.2.2 Precipitation Datasets and Vegetation Variables

Considering the paucity of observations and the low-gauge density over the Congo Basin (Washington et al. 2013), various precipitation data and satellite-retrieved geophysical variables are used to quantify variations in the JJA dry season. This study adopted three widely used precipitation datasets that combine ground observations and satellite retrievals and one reanalysis dataset (Table 2.1). We used the observational gridded daily rainfall data from the Global Precipitation Climatology Center (GPCC) at 1°×1° resolution (1988-2013) (Schamm et al. 2015), the pentad (5-day) data from the Global Precipitation Climatology Project (GPCP) at 2.5°×2.5° resolution (1979-2014) (Xie et al. 2003) and the Climate Prediction Center (CPC) Merged Analysis of Precipitation (CMAP) at 2.5°×2.5° resolution (1980-2015) (Xie and Arkin 1997). The daily GPCC data were produced based on abundant in situ observations and high-tech interpolation methods conducted by the World Meteorological Organization (WMO) (Schamm et al. 2015). Both the GPCP and CMAP precipitation have the advantage of combining gauge (including GPCC) and satellite observations. Another hourly reanalysis data from the National Aeronautics and Space Administration (NASA) Modern-Era Retrospective Analysis for Research and Applications, version 2 (MERRA2), with land surface diagnostics at 0.625°×0.5° resolution for the period 1980-

2015 was utilized as well (Gelaro et al. 2017). MERRA2 can reproduce the observed rainfall climatology, patterns, and variability over central equatorial Africa more efficiently than other available reanalysis products (Molod et al. 2015; Hua et al. 2019). Monthly reanalysis root zone soil moisture (RZSM) data for the period 1980-2015 from CPC (at 0.5° resolution) (Fan and van den Dool 2004), MERRA2 (at 0.625°×0.5° resolution) (Reichle et al. 2017) and ERA-Interim (at 1.0° resolution) (Albergel et al. 2012) were used as auxiliary parameters to measure water availability.

Three satellite-derived vegetation datasets were analyzed to quantify the variations in the JJA DSL over the Congo Basin from the ecological perspective. We chose the widely used biweekly maximum value composite Normalized Difference Vegetation Index (NDVI3g) from the third generation Global Inventory Modeling and Mapping Studies (GIMMS) generated based on the Advanced Very High Resolution Radiometer (AVHRR) data at 8 km resolution from 1982 to 2015 (Pinzon and Tucker 2014). This dataset has been verified as having the best calibration and is the most accurate in terms of temporal changes in vegetation (Beck et al. 2011). Nevertheless, as calculated from the red and near-infrared solar reflectance, NDVI over tropical forests is probably impacted by clouds and atmospheric aerosols, which raise data uncertainties and noise in surface reflectance data (Asefi-Najafabady and Saatchi 2013). Hence, empirical orthogonal functions were applied to decompose the NDVI data into various spatial and temporal components for the long-term large-scale pattern analysis (Eastman and Fulk 1993; Anyamba and Tucker 2012). Combined with the cloud mask available within this dataset, the first six components explaining 77% of the original data variance were used to reconstruct the NDVI data.

A newly merged daily vegetation optical depth (VOD) at 0.25° spatial resolution from 1993 to 2012 (Liu et al. 2013) was derived from a series of passive microwave satellite sensors,

including Special Sensor Microwave Imager, Advanced Microwave Scanning Radiometer, Fengyun-3B Microwave Radiometer Imager and Windsat. VOD measures the dynamics of water content within vegetation and is less sensitive to abundant clouds and atmospheric aerosols than the NDVI dataset. In addition, to make results comparable to precipitation, these two vegetation datasets were remapped on 1.0° grid box using the nearest neighbor interpolation.

A newly developed dataset of solar-induced fluorescence (SIF v27) from 2007 to 2016 (Joiner et al. 2013; Joiner et al. 2016) was also used from the Global Ozone Monitoring Experiment instrument on the MetOp-A satellite. SIF is emitted from chlorophyll during photosynthesis and is primarily driven by the amount of absorbed photosynthetic radiation (Sun et al. 2018). Although chlorophyll fluorescence has been a major tool for basic research in photosynthesis for many years (Krause and Weis 1991), it was discovered recently that SIF can be retrieved from space using moderate spectral resolution radiances and has provided a new proxy for global plant photosynthesis (Sun et al. 2018). Here, the 40 km x 80 km individual SIF observations were processed into 5-day time steps at a spatial resolution of 2.5°.

2.2.3 Definition of Dry Season Onset and End

The variety of rainfall regimes over Central Africa complicates the characterization of the seasonality. Rather than setting a unified precipitation threshold, such as 100 mm/day as done in previous studies, the method based on calculating cumulative rainfall anomaly (Liebmann et al. 2012; Dunning et al. 2015) was adjusted and applied to identify the onset and end of the dry season. First, the climatological pentad (5-day) mean rainfall rate $\bar{P}$ was calculated using the data from all months in all years, and from this the annual cumulative pentad rainfall anomaly on pentad d, *A(d)* was found:

$$A(d) = \sum_{j_0}^{d} P_j - \bar{P} \quad (2.1)$$

where P_j is the rainfall on pentad j and j ranges from March (j_0) to the pentad d being considered. *A(d)* was calculated from March to November to include the JJA dry season. *A(d)* increases when the pentad precipitation is above the climatological mean and decrease when the precipitation is below the climatological mean and decrease when the precipitation is below the climatological mean 5-d rainfall (Fig. 2.3). Thus, the day of maximum *A(d)* is the dry season onset (DSO) and the day of minimum *A(d)* is the dry season end (DSE). This method was applied to all the datasets mentioned above to explore the spatial pattern of climatology and trends of the dry season.

2.2.4 Long-term Trend Analysis

Before conducting the trend analysis, all precipitation and vegetation datasets were interpolated onto the unified pentad (5-day) temporal resolution. After identifying the DSO and DSE, annual DSL in days can be calculated as the difference between DSE and DSO within each grid box over the study region. Two methods were used to quantify and validate the temporal changes at both the grid and regional level. First, the linear trend of annual DSL time series was estimated using the ordinary least squares regression over the same time period for each grid box. Its statistical significance level (*P*) was assessed by the two-tailed Student's t-test to verify whether the trend was statistically significant rather than random noise. Trends of DSO and DSE were estimated similarly. Second, the non-parametric Mann-Kendall (MK) trend test was applied on the time series of DSL, DSO and DSE to detect whether a significant monotonic increasing or decreasing trend exists. The *P* value was also measured by the two-tailed Student's t-test. The MK test provides additional verification for the robustness of the linear regression trend analysis, as it is less sensitive to the beginning and end of the analysis period. In particular, for the spatial pattern

of DSL trends, results were only plotted for grids with annual rainfall > 250 mm and a dry spell of at least 5 d, to avoid singular and inauthentic trends over extreme dry or wet grids (Yang et al. 2015). Similarly, trends were only shown for grids with annual mean NDVI > 0.3 (Pinzon et al. 2014; Zhou et al. 2014), VOD > 0.4 (Liu et al. 2013), SIF > 0.4 (Joiner et al. 2011), and a dry spell of at least 5 d for satellite-derived vegetation variables. Finally, to maximize the large-scale features while minimizing local-scale variability and noise, the time series of DSL/DSO/DSE at the regional aggregated level were calculated using area-weighted averaging over the study region. The corresponding linear trends of DSL/DSO/DSE at the regional level were estimated as done at the grid level.

2.3 Results

2.3.1 Observed Changes in DSL by Precipitation Datasets

The spatial patterns of DSL trends derived from GPCC, GPCP, CMAP and MERRA2 are shown in Fig. 2.4. Although differing in spatial resolution and data sources, all rainfall datasets show a lengthening DSL ($P \leq 0.1$) over the Congo Basin, particularly over the central and south basin and part of the north basin, which is usually wet during JJA. GPCC and GPCP detected a longer DSL in the northwest basin as well, while CMAP and MERRA2 showed stronger drying in the east. Overall, we observed a strong drying trend over the Congo Basin, where all gridded precipitation datasets show a maximum DSL increasing rate of 30 days per decade.

Figure 2.5 shows the interannual variations in DSL spatially averaged over the Congo Basin from the four precipitation datasets. The DSL increased significantly by 6.4-10.4 days decade^{-1} for the period 1988-2013, with a rapid increase around the early 2000s matching previous records of droughts in Central Africa (Masih et al. 2014). The increased DSL is attributed to an earlier DSO

by 6.6-7.4 days decade^{-1}, with an insignificant delay in the DSE (not shown). The advanced DSO is consistent with the observed long-term decline in rainfall during AMJ.

2.3.2 Observed Changes in DSL by Vegetation Products

Since rainforest is largely determined by precipitation patterns, the satellite-derived vegetation variables NDVI, VOD and SIF were utilized to provide ecological verifications for the above results. Seasonal cycles of rainfall, NDVI, VOD and SIF show that peak geophysical vegetation values lag behind peak rainfall. Vegetation variables are significantly correlated with rainfall in earlier months: NDVI lags the rainfall by about one month (R=0.86, P=0.000), VOD lags by two months (R=0.84, P=0.000) and SIF lags by half month (R=0.89, P=0.000) (Fig. 2.6). Vegetation variables may detect different DSO or DSE dates due to the lagged correlations with precipitation, but the seasonal cycle in vegetation is comparable to the bimodal precipitation cycle observed over the Congo.

Figure 2.7 shows changes in DSL according to NDVI and VOD. DSL increased by 10.5-18.2 days decade^{-1} for the period 1993-2012, particularly over the east and west basin. NDVI detected a significant increase in DSL in the central basin as well. There are a few grid boxes showing decreasing DSL near the edges of the rainforest according to the VOD data. This is probably due to the uncertainty attributable to drought-tolerant shrublands constituting a varying mixture of grass and woody components containing high water content, which may have resulted in relatively high VOD values leading to shorter DSL (Liu et al. 2013). The lengthened DSL can mainly be attributed to a delayed DSE, which is delayed by 9.9-18.4 days decade^{-1} (P = 0.001), indicating a delayed start in next growing season.

We then analyzed the newly developed SIF data and compared the results to NDVI data for the period 2007-2015 given the exacerbated drying trend since the 2000s (Fig. 2.8). DSL increased

steadily and rapidly over the north, south and east Congo Basin by 24.4-40.6 days decade^{-1}. The sharply increased DSL is attributed to an earlier DSO rather than to a delayed DSE, as detected by the long-term datasets over different periods.

2.3.3 Discrepancies in Hydrological and Ecological Measurements due to Precipitation-soil-vegetation Interactions

Differences in the spatial patterns of DSL trends among precipitation and vegetation variables are expected. Besides uncertainties in rainfall datasets, the complex lagged correlation among rainfall-RZSM-vegetation, differences in drought tolerance among plant species and forest fragmentation also contribute to the differences (Lewis 2006; Fauset et al. 2012). Dense forest with deep roots has access to groundwater, delaying the inception of moisture stress through redistribution of soil moisture. Open forest with semi-deciduous vegetation has less resilience to drought and is thus more sensitive to hydrological disturbances (Hirota et al. 2011; Zhou et al. 2014).

The delayed DSE detected by NDVI and VOD coincides with the earlier DSO detected by precipitation. Higher rainfall in the months preceding the dry season replenishes groundwater, providing a water source that plants can access using deep root systems during the drier months. Therefore, the decline in precipitation during AMJ would reduce soil moisture, resulting in water stress and affecting soil rehydration and vegetation growth in the next wet season (Ridolfi et al. 2006).

RZSM data from CPC, MERRA2 and ERA-Interim were analyzed. Figure 2.9 shows the correlation between soil moisture and rainfall. Soil moisture significantly lags rainfall in the precedent wet season, while autocorrelation within rainfall anomalies is much smaller and

insignificant (Fig. 2.9b). Precipitation and soil moisture have both decreased since the 1980s: Precipitation declines dramatically from March to June, by 0.24-0.42 mm day^{-1} $decade^{-1}$ ($P = 0.001$) (Fig.2.9a). Consequently, soil moisture decreased dramatically and was not fully replenished during JJA. Vegetation variables declined during JJA, presumably due to the water deficit (Fig. 2.9c). Thus, more rainfall was required to replenish soil water deficit to stimulate rainforest growth in next wet season (September-November). Water stress in the pedosphere elucidates how reduced precipitation at the DSO affects the vegetation phenology and leads to a delayed ecological DSE. Besides water availability, rainforests are also affected by light. However, increased photosynthetically active radiation may actually enhance water stress and adversely influence plant growth, by exacerbating water deficits during long-term droughts and longer DSL (Zhou et al. 2014). This is demonstrated by the observed delay in DSE and decline in vegetation greenness (Figs. 2.8g-h, 2.9c).

The exacerbated lengthening in the DSL and an earlier DSO observed by the NDVI and SIF during the past decade can be explained by seasonal variations in precipitation and soil moisture as well. Soil moisture has declined during JJA since the 1980s, resulting in water deficit during August-September at the DSE. However, the DSE water deficit reduced and recovered by approximately 2005, probably attributable to a recent increase in precipitation and soil moisture during August-September, while the decline in rainfall continued during AMJ (Fig. 2.10). This shifts the water deficit to April-May, resulting in an earlier DSO driving the increase in DSL for the period 2007-2015.

2.4 Conclusions and Discussions

Due to insufficient observations over the Congo Basin, we used reanalysis and satellite datasets to study the variations in precipitation and vegetation seasonality. Our analyses indicate a comparable and consistent increasing trend in the JJA DSL from all datasets for the period 1979-2015 and similar peaks of DSL around 2004 and 2005 at the regional level. However, there are some discrepancies in the magnitude and spatial distribution of DSL trends that may have resulted from data uncertainties and the different approaches used to generate homogeneous climate records.

For the precipitation datasets, gauge-based GPCC and satellite-combined CMAP and GPCP are quite sensitive to the number and density of observations used (Schamm et al. 2015; Xie et al. 2003; Xie and Arkin 1997). Due to sparse observational stations over the Congo Basin, different interpolation methods were adopted to fill data gaps, which might have generated errors in the rainfall products. For satellite-retrieved vegetation variables, effects of satellite change-over, orbital drifts, volcanic aerosols, and changes of solar zenith angles have been corrected, but residual non-vegetation signal may still remain. Despite intensive cloud screening and preprocessing, NDVI may still contain residual non-vegetation signals due to contaminations of sub-pixel clouds and biomass burning, which can cause spurious NDVI changes (Tucker et al. 2005). In addition, bi-weekly temporal resolution may miss the detailed temporal evolution of NDVI phenology on time scales shorter than two weeks. VOD is less affected by clouds and aerosols because it measures water content contained in biomass via passive microwave radiation. Nevertheless, VOD is underestimated when there are substantial open water bodies in the observation footprint (Liu et al. 2013; Liu et al. 2015). The SIF dataset includes bias due to

instrument degradation (Joiner et al. 2016). Overall, these issues probably introduce some uncertainties in our estimates of dry season changes.

Attributing the DSL variations is an important question and warrants a better understanding of precipitation over Central Africa, which is influenced by moisture transport, circulations, local ET, and orography. During the DSO, the AMJ rain belt shrank and weakened during the dry period (2000-2014) (Fig. 2.10c), and this coincided with less moisture transported from the Indian Ocean due to abnormal subsidence in Central Africa and the intensification and eastward extension of the Walker circulation over the Indo-Pacific Ocean (Hua et al. 2016). In addition, the Congo Basin is characterized by a large recycling ratio (~25%) (Dyer et al. 2017). ET provides considerable moisture, and land-atmosphere interactions play an important role during the dry season, particularly at the DSE, since moisture fluxes from the oceans are much weaker in August-October than in AMJ (Fig. 2.11). Quantifying the contributions of different processes to the lengthened DSL should be the focus of future work.

Our research highlights an important scientific issue of dry season changes over the Congolese rainforest and their association with precipitation, vegetation, and water availability under global warming. Historical records and climate models indicate increased aridity since the 1950s over Central Africa (Dai 2013). Our results show that the JJA dry season has lengthened over the Congolese rainforest since the 1980s. Consequently, the longer DSL has increased land evaporative demand, reduced cloud cover and increased surface incoming solar radiation, which in turn amplified the aridity (Berg et al. 2016). In addition, the Congo Basin stores extensive above-ground and underground carbon (Lewis 2006; Dargie et al. 2017). The local intact rainforest has become increasingly fragmented since 2000 (Potapov et al. 2017), and widespread above-ground carbon loss has been observed during the latest decade in the central and north basin (Baccini et

al. 2017), coinciding with the significant increasing DSL trends reported in this study. If the long-term drying continues, the carbon sink is unlikely to continue but may transform to a carbon source and thus accelerate global warming (Cox et al. 2000). This underscores the importance of studying lengthened DSL over tropical rainforests.

Tables and Figures

Table 2.1 Rainfall products used in this study.

PRODUCT	TIME	INPUTS	RESOLUTION		GAUGE USE
			spatial	temporal	
GPCC full data daily version 1.0	1988-2013	gauges	1.0 °	daily; monthly	Gauge only
GPCC V7	1901-present				
GPCP V2.2	1979-present	IR, MW, gauges	2.5 °	pentad; monthly	Adjusted
GPCP V2.2					
CMAP (enhanced)	1979-present	Infrared (IR), microwave (MW), gauges	2.5 °	pentad	Merged
MERRA-2	1980-present	reanalysis	0.625°×0.5°	hourly	Validated by GPCP

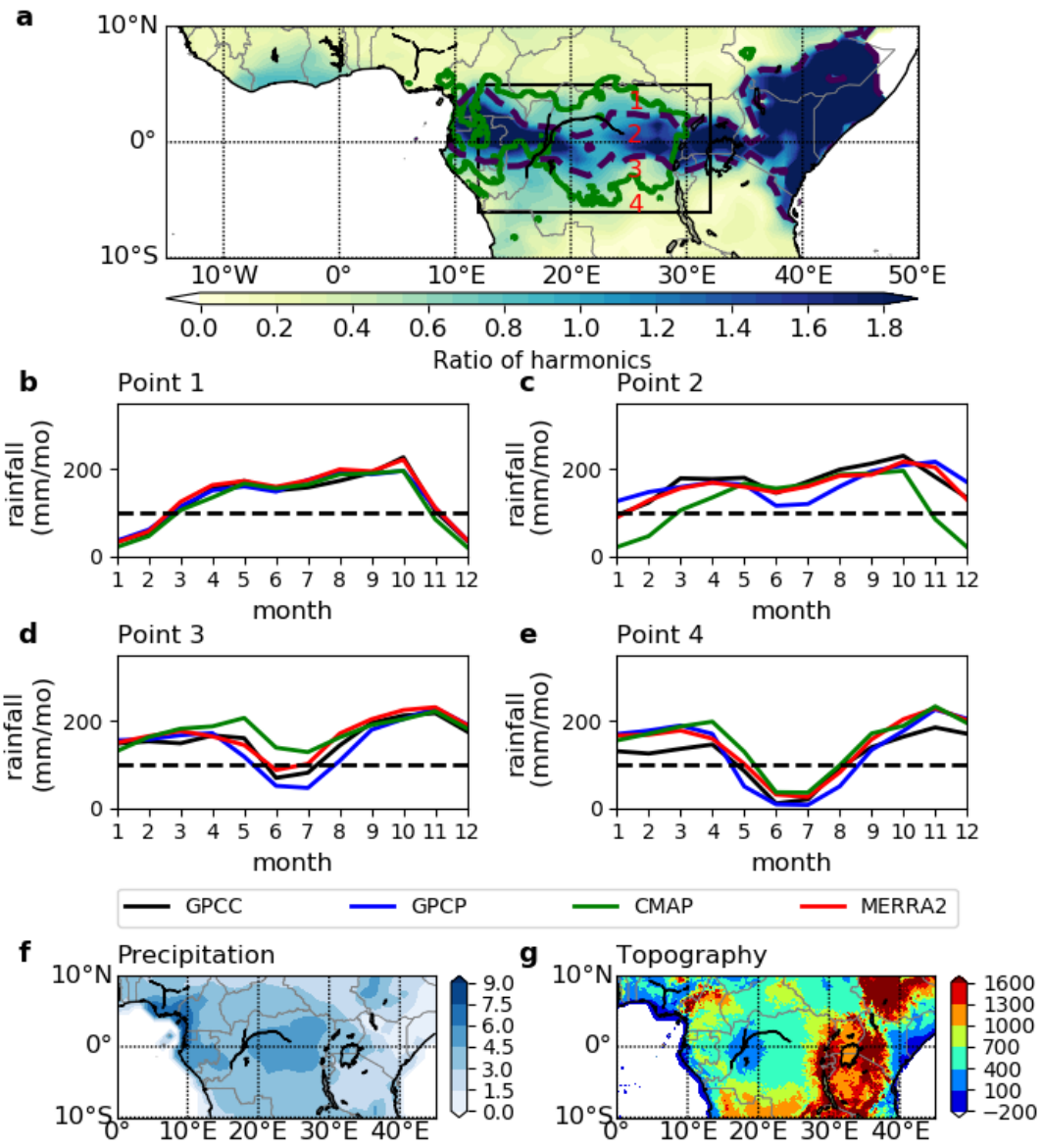

Figure 2.1 Precipitation seasonality and climatology over equatorial Africa: (a) The ratio of amplitudes of the harmonics at frequency of two and one cycle per year via Fourier Analysis (Dunning et al. 2016) for each grid box based on the monthly GPCC rainfall data set (1980-2015) (Schneider et al. 2015). The dashed contour marks the boundaries with the ratio of 1.0, inside which grid boxes have two wet seasons and two dry seasons per year. The black rectangle delineates the study region (12°E-32°E, 5°N-6°S). The green line delineates the boundary of the Congolese rainforest. For illustrative purposes, typical rainfall seasonal cycles are shown for four different points at the same longitude (25.5°E) at (b) 3.5°N, (c) 0.5°N, (d) 2.5°S and **e,** 4.5°S from the GPCC, GPCP, CMAP and MERRA-2 datasets for the period 1980-2015. (f) Climatological annual mean precipitation (mm/d) for the period 1980-2015 from GPCC. (g) Topography (m) of Central Equatorial Africa from SRTM30_PLUS (Becker et al. 2009).

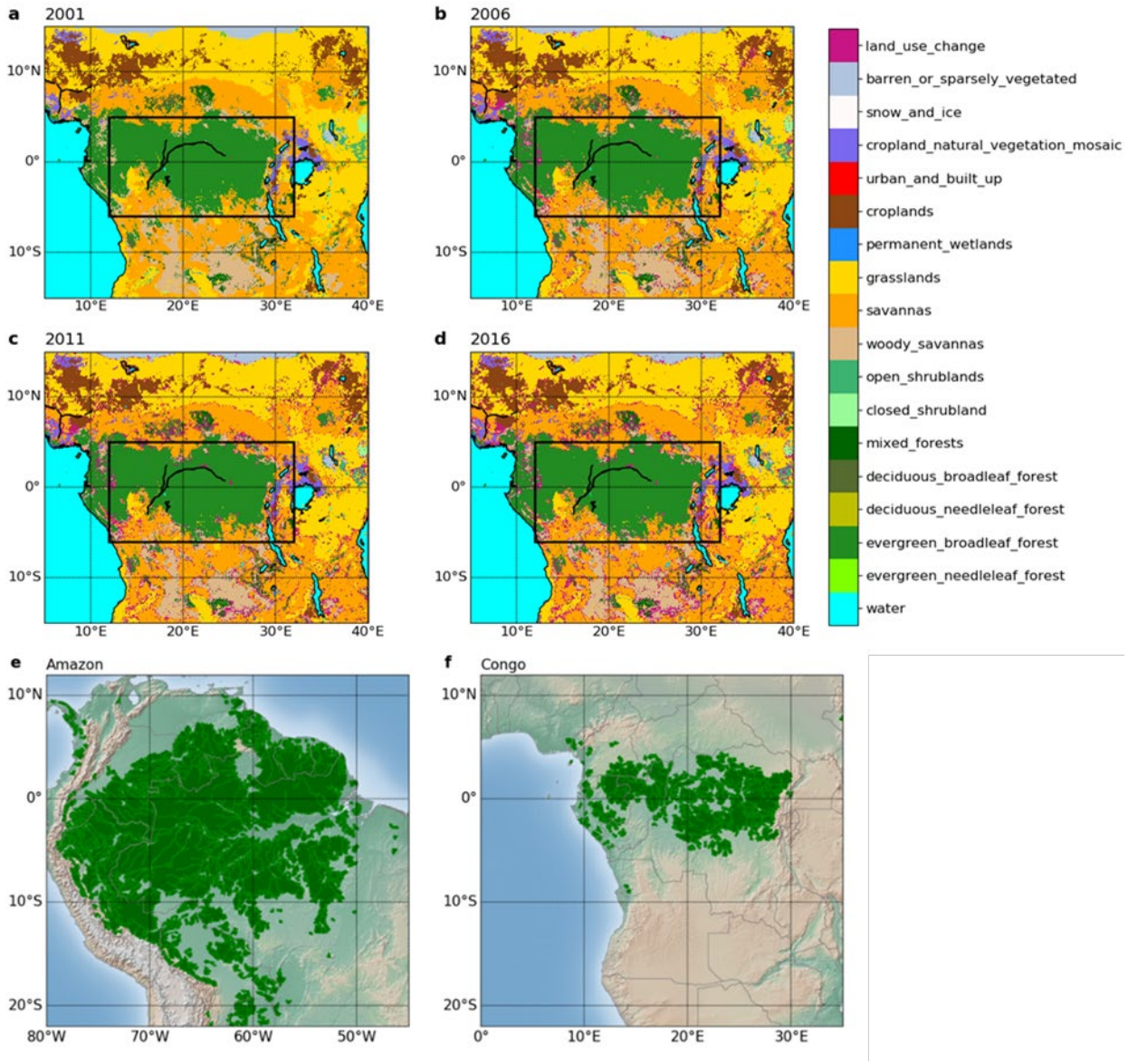

Figure 2.2 Maps of land cover types and intact forest landscape. Land cover/use types and changes over Central Africa in (a) 2001, (b) 2006, (c) 2011 and (d) 2016 estimated by the MODIS land cover product (MCD12C1) based on the International Geosphere-Biosphere Programme (IGBP) classification scheme (Friedl et al. 2010). Maps of intact forests (Potapov et al. 2008) in (e) the Amazon and (f) the Congo in 2000 based on the Landsat image collection, which exhibit no remotely detected signs of human activity or habitat fragmentation.

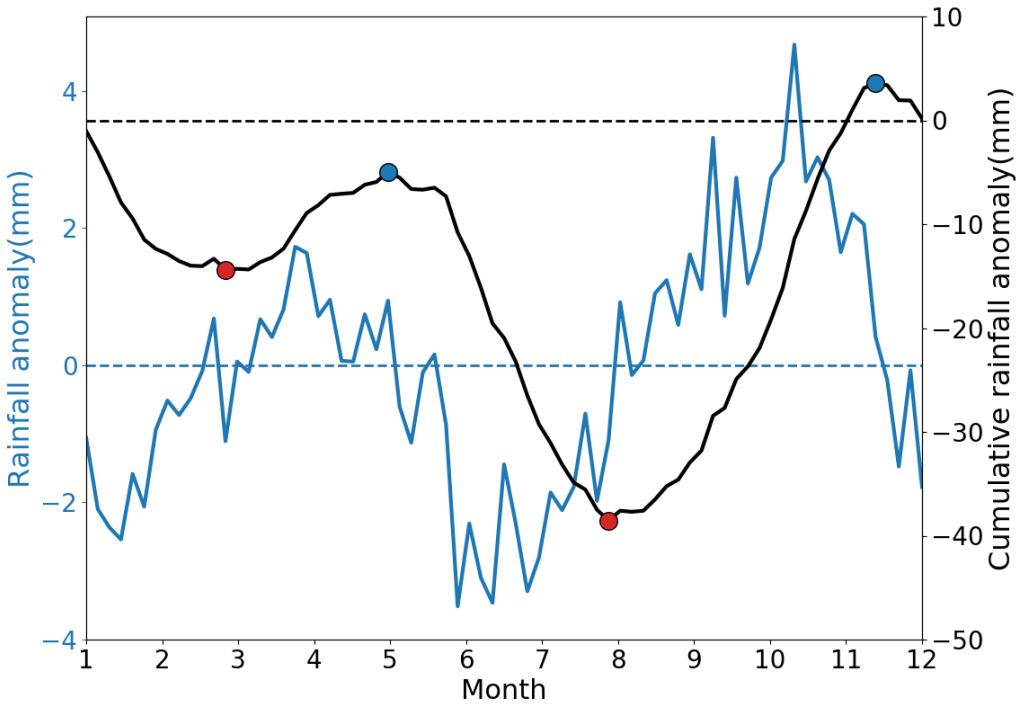

Figure 2.3 Climatological 5-day mean rainfall anomaly (blue) and cumulative 5-day mean rainfall anomaly (black) for the grid box centered at 1.5°S, 21.5°E from the daily GPCC dataset for the period 1988-2013 (see Eq. 2.1). Blue dots mark the onset of dry seasons, while red dots mark the end of dry seasons.

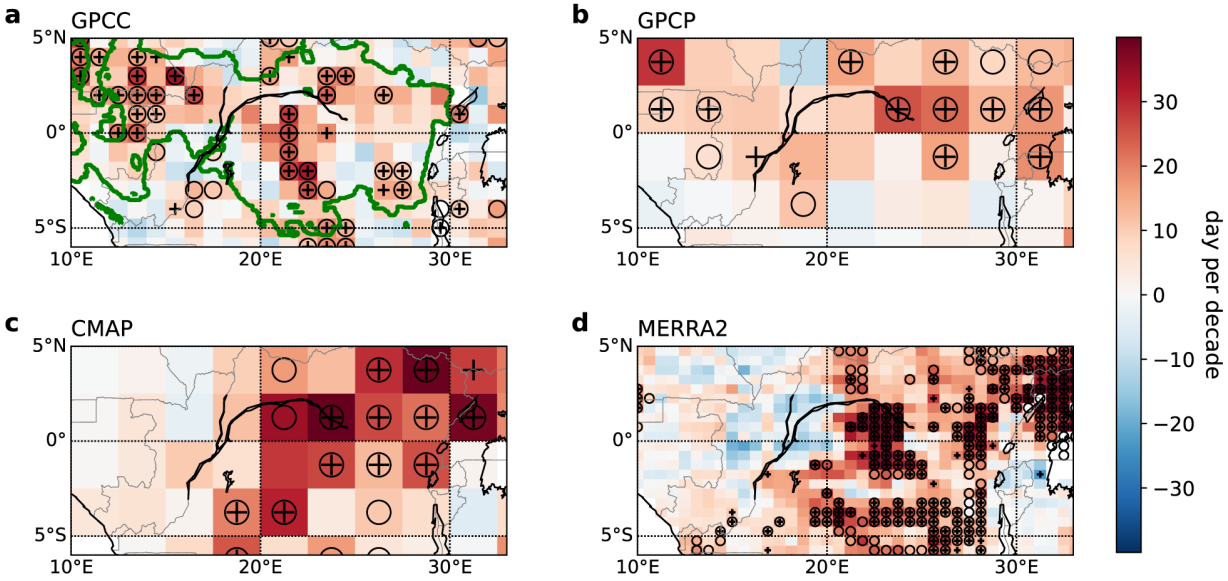

Figure 2.4 Spatial patterns of linear trends of the JJA DSL from four precipitation datasets for the period 1988- 2013: (a) GPCC, (b) GPCP, (c) CMAP and (d) MERRA2. The green line delineates the boundary of the Congolese rainforest. Grid boxes with crosses have a significant linear trend at $P < 0.1$. Grid boxes with circles pass the Mann-Kendall (MK) trend test and have increasing trends at the 10% significance level.

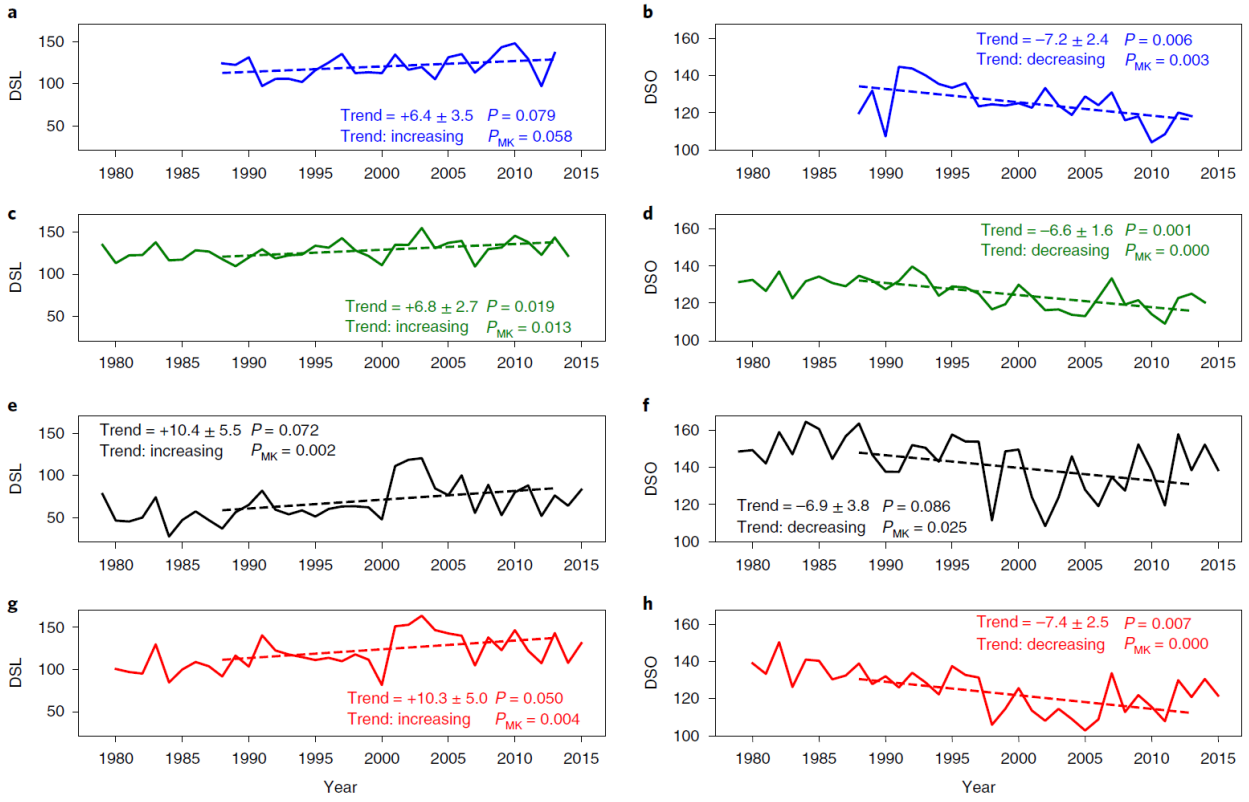

Figure 2.5 Regionally aggregated interannual variations (solid lines) and linear trends (dashed lines) of the JJA DSL and DSO. (a-b) GPCC (1988-2013), (c-d) GPCP (1979-2014), (e-f) CMAP (1979-2015) and (g-h) MERRA2 (1980-2015). The linear trend (d decade^{-1}) and its significance level *P* for the period 1988-2013 are shown. Results and significance level of the MK trend test over the full temporal span of each precipitation dataset are included.

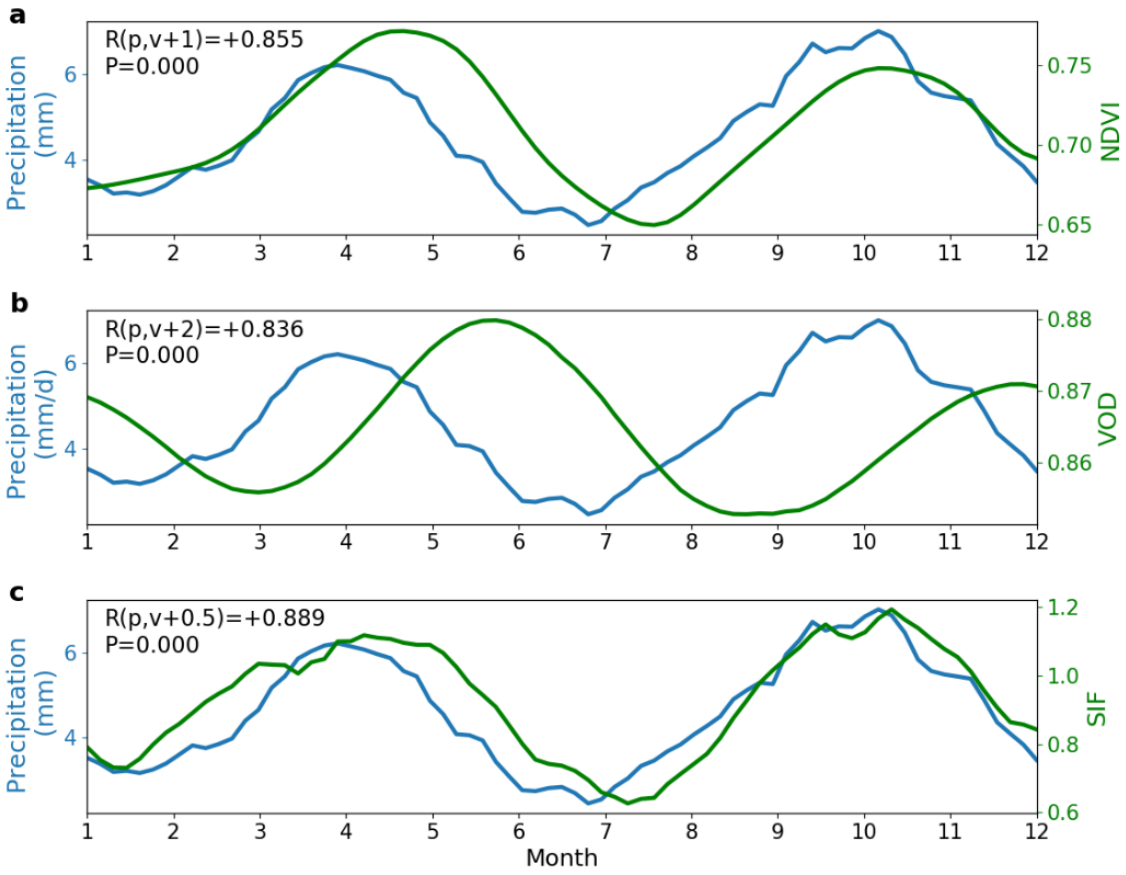

Figure 2.6 Climatological regional mean seasonal cycles of rainfall from the 15-day smoothed daily GPCC dataset superimposed with (a) preprocessed NDVI for the period 1982-2015, (b) VOD for the period 1993-2012 and (c) 15-day smoothed SIF for the period 2007-2016 over the Congo Basin. The lagged correlation between precipitation and vegetation index and its significance level *P* are shown.

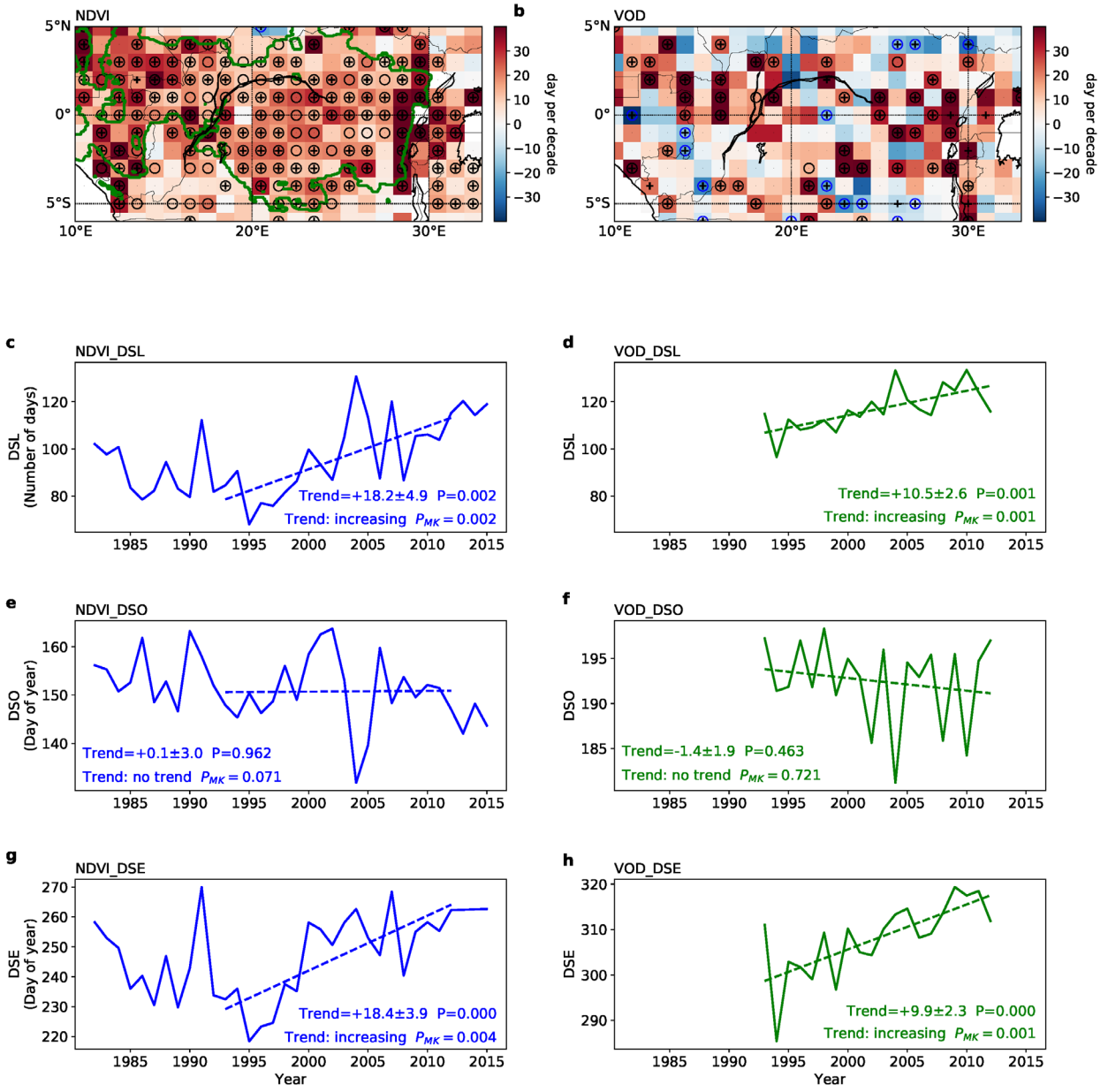

Figure 2.7 The JJA dry season changes estimated using satellite derived NDVI (1982-2015) (left panels) and VOD (1993-2012) (right panels): Spatial patterns of linear trends of the DSL estimated by (a) NDVI and (b)VOD for the period 1993-2012. The green line delineates the boundary of the Congolese rainforest. Grid boxes with crosses have significant linear trends ($P < 0.1$using least squares regression), and grid boxes with circles pass the MK trend test at the 10% significance level. Regional aggregated interannual variations (solid lines) and linear trends (dashed lines) of the DSL from (c) NDVI and (d) VOD. (e-f) Same as (c-d) but for the DSO. (g-h) Same as (c-d) but for the DSE. The linear trend (d decade^{-1}) and its significance level P for the period 1993–2012 are shown. Results and significance level of the MK trend test over the full temporal span of each dataset are also included.

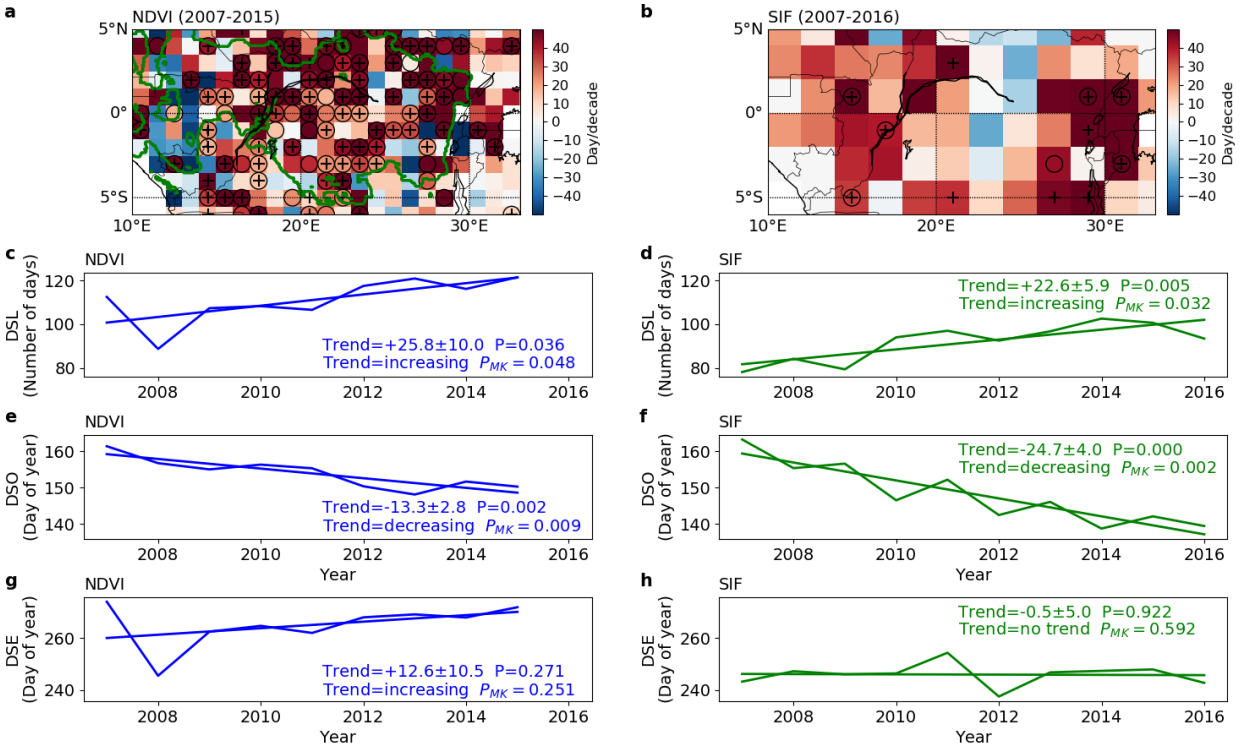

Figure 2.8 JJA dry season changes estimated by NDVI and SIF for the period 2007-2015: Spatial patterns of linear trends of the DSL from (a) NDVI and (b) SIF. The green line delineates the boundary of the Congolese rainforest. Grid boxes with black crosses dots have significant linear trends (P < 0.1using least squares regression), and grid boxes with circle pass the MK trend test at the 10% significance level. Regional aggregated interannual variations and linear trends of the DSL from (c) NDVI and (d) SIF. (e-f) Same as (c-d) but for the DSO. (g-h) Same as (c-d) but for the DSE. over the Congo Basin. The linear trend (d decade^{-1}) and its significance level *P* are shown. Results and significance level of the MK trend test are included.

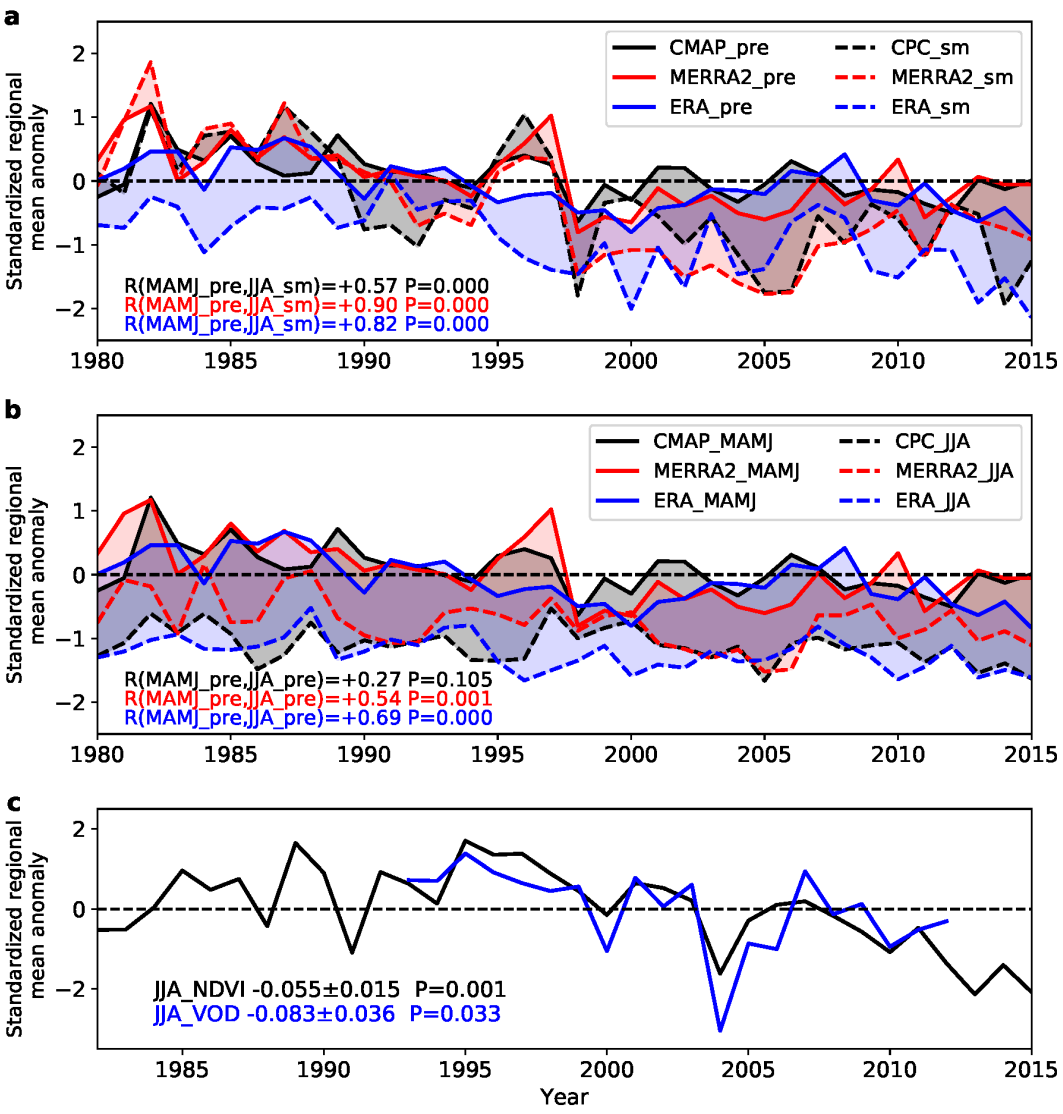

Figure 2.9 Interannual variability of standardized regional mean precipitation (pre), soil moisture (sm) and vegetation parameters (NDVI and VOD) for the period 1980-2015: (a) Soil moisture anomaly (dashed line) in JJA and its relationship with rainfall anomaly (solid line) during March-June from the CPC, MERRA2 and ERA-Interim. The lagged correlation *R* between soil moisture and rainfall and its significance level *P* are shown. (b) Rainfall anomaly in JJA and its relationship with rainfall anomaly during March-June from the CPC, MERRA2 and ERA-Interim reanalysis datasets. The autocorrelation *R* and its significance level *P* are shown. (c) Vegetation anomalies during JJA. Trends and significance level *P* are included.

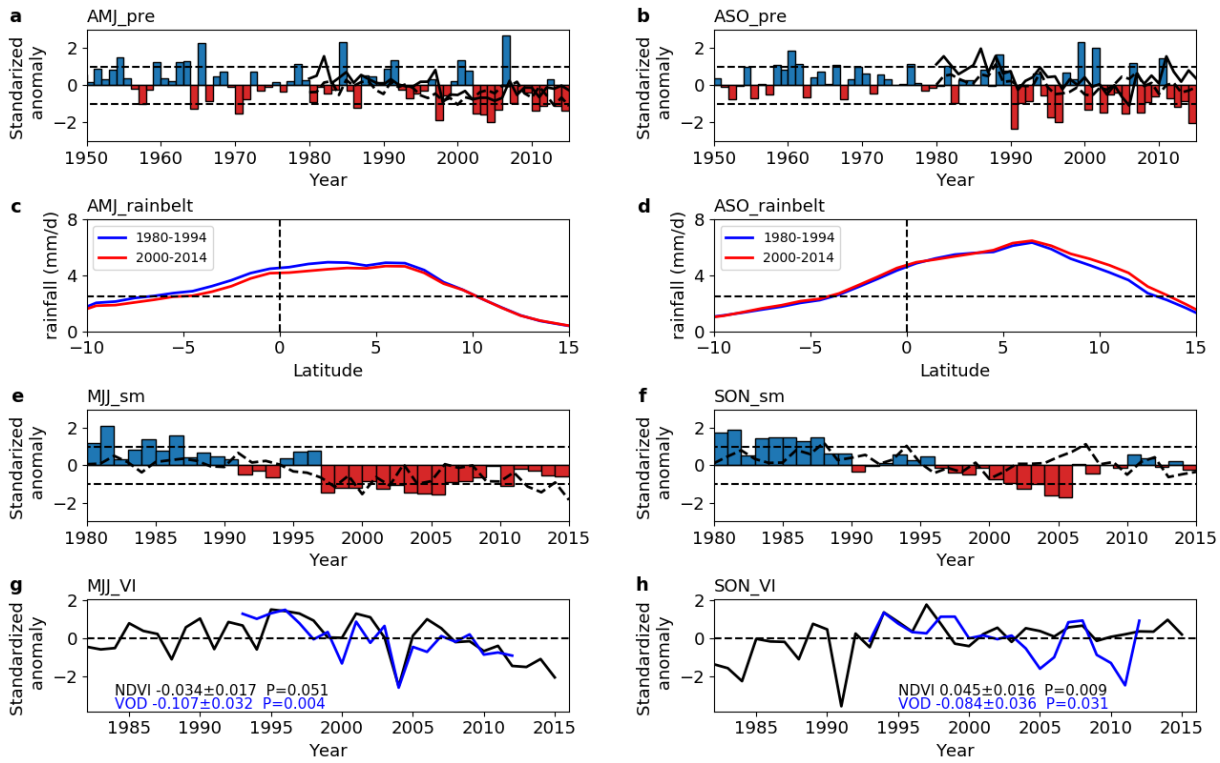

Figure 2.10 Standardized precipitation anomalies over the Congo Basin during (a) April-May-June (AMJ) and (b) August-September-October (ASO) from GPCC (1950-2015; bar), MERRA2 (1980-2015; solid line) and ERA-Interim (1980-2015; dashed line). Climatological zonal mean (10°E-40°E) rain belt from April to August in the wet period 1979/1980-1993 and the dry period 2000-2014 (Hua et al. 2016) from GPCC in (c) AMJ and (d) ASO. The dashed line marks the rainfall rate of 2.5 mm/day, which is usually used as the threshold to define the tropical rain belt. Standardized soil moisture anomalies over the Congo Basin during (e) May-June-July (MJJ) and (f) September-October-November (SON) from MERRA2 (1980-2015; bar) and ERA-Interim (1980-2015; dashed line). Standardized vegetation anomalies over the Congo Basin during (g) MJJ (h) SON from NDVI (1980-2015), VOD (1993-2012). Trend and *P* value are available.

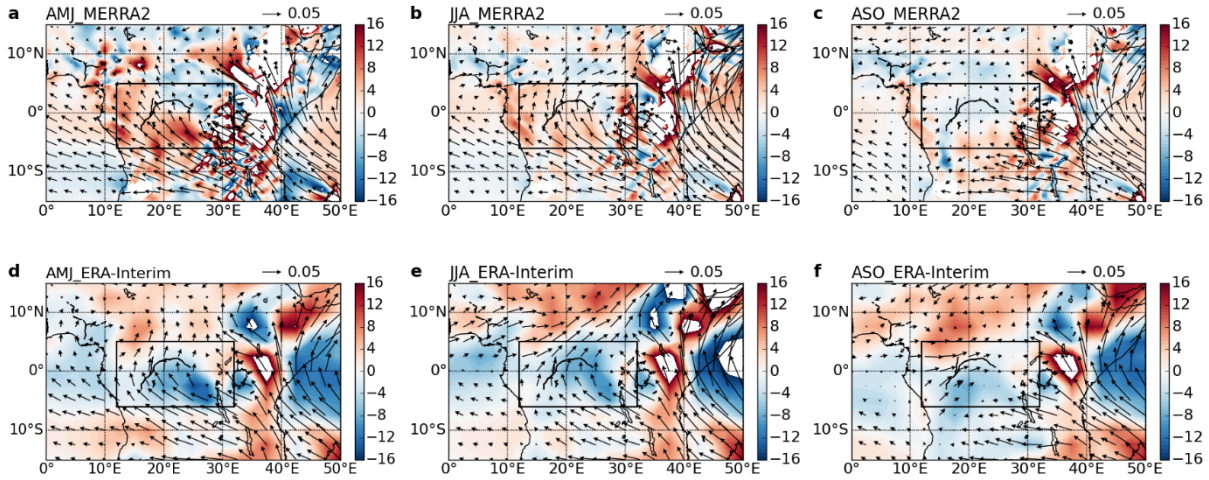

Figure 2.11 Climatological mean moisture flux (kg· kg^{-1}· m· s^{-1}, vector) and divergence (10^{-8} kg· kg^{-1}· s^{-1}, convergence is shaded in blue) at 850hPa for the period 1980-2010 from MERRA2 in (a) AMJ, (b) JJA and (c) ASO. (d-f) Same as (a-c) but from ERA Interim.

Chapter 3 Observed Changes in Fire Patterns and Possible Drivers over Central Africa

3.1 Introduction

It is estimated that Africa is responsible for ~70% of global burned area and ~50% of fire-related carbon emissions, mostly from local savanna ecosystems (Andela and van der Werf 2014). Central Africa contains complex savanna, grassland and rainforest ecosystems and is a crucial hot spot for wildfires. It has experienced a long-term drying trend and a widespread increase in the boreal summer DSL since the 1980s (Zhou et al. 2014; Hua et al. 2016; Hua et al. 2018; Nicholson et al. 2018b; Jiang et al. 2019), which may have exposed local ecosystems and societies to a greater risk of wildfires.

Though increasing wildfire risk is suggested under the warming and drying climate (Pechony and Shindell 2010), a complex big picture of prospective global and regional fire trends is emerging based on recent satellite observations (Aldersley et al. 2011; Andela et al. 2017). Increasing wildfire and burned area have been observed over the mid-latitude and subtropical forests in the Northern Hemisphere (Westerling et al. 2006; Riaño et al 2007). In contrast, over the tropics, large decreases in burned area occurred in the savannas of South America, Africa, and grasslands across the Asian steppes (Andela et al. 2017). On average, global burned area declined by 24% over the period 1996-2015, and there was a potential shift in global pyrogeography from savanna-dominated to forest dominated (Andela et al. 2017). The documented decrease in observed fires over Africa (Andela and van der Werf 2014, Andela et al 2017) based on the satellite-derived MODerate resolution Imaging Spectroradiometer (MODIS) Collection 5 burned area data, however, suffered large uncertainties, including the occurrence of false alarms caused

by small forest clearings, the omission of large fires obscured by thick smoke and small fires by the limited algorithm, and sensor degradation (Giglio et al. 2016).

A holistic characterization of fire changes requires not only the consideration of the mean state of burned area but also variations in fire frequency and size. Fire frequency and size exert first-order impacts on biomass accumulations and land cover types (Yates et al 2009). Naturally, examining spatiotemporal variability in frequency and size of individual fires provides important information on changes in burned area. Previous studies suggested that decreased global burned area was mainly attributed to decreased fire frequency, while regional changes in fire frequency and size varied geographically (Andela et al 2017). Nevertheless, relatively few studies have examined the changes in frequency and size of different wildfire categories over the tropic hotspot.

Recent studies have documented regulations of weather or anthropogenic factors on wildfires by applying first-order linear statistic models (Flannigan et al 2009, Archibald et al 2010, Forkel et al 2019). One major challenge is determining the dominant factors which provide cross-scale insights for fire predictions under a changing climate (Archibald et al 2018). The complex interactions among fires, weather conditions and vegetation fuel make predictions difficult. Climatic and anthropogenic factors often show antagonistic and non-linear behaviors with respect to fire occurrence (Aldersley et al 2011). For instance, increased population density is associated with increased fire numbers, but it also reduces fuel load, which reduces fire spread (Lasslop and Kloster 2017). Recently, the random forest regression model has been applied to study drivers of fire to better interpret the explanatory nature of the independent variables (Archibald et al 2009, Aldersley et al 2011, Mayr et al 2018). This advanced model provides a promising new approach to deal with unprecedented amounts of data and to understand fire trends.

The availability of an improved MODIS fire product provides a great opportunity to investigate robust trends in fires and possible drivers over Central Africa. The Collection 6 burned area mapping algorithm and product have several algorithmic improvements and calibration adjustments, which address the aforementioned data quality issues (Giglio et al 2018). This improved dataset also allows us to better separate contributions from different fire categories and different land cover types. With these in mind, we analyzed fire changes and possible drivers over Central Africa. Combining the utility of the random forest model, we aimed to answer the following questions: 1) Is there a decreasing trend in burned area over Central Africa as reported at the global scale? If yes, how does this change vary by land cover and attribute to changes in fire frequency and size? 2) Which factors are primarily responsible for the changes?

3.2 Study Region, Data, and Methods

3.2.1 Study Region

This study focused on Central Africa (10°E-40°E, 15°N-15°S) covering the Congo Basin and surrounding savannas. This domain was carefully chosen given that it has the highest fire frequency and the most extensive burned area in the world. Human influences vary from the minimum in the rainforest to the maximum in the savannas and grasslands (Zhou et al. 2014). These features make Central Africa an ideal target to study the wildfire change in a warming climate and attribute the human and climate drivers.

3.2.2 Satellite-retrieved Burned Area and Land Cover Products

Two global satellite-derived burned area products were used. One was the monthly burned area variable at 500-m spatial resolution (MCD64A1 Collection 6, 2001-2018) combining Terra

and Aqua satellites from NASA (Giglio et al. 2018). It provides the approximate date of burning by detecting changes in daily surface reflectance to study the size distribution of individual fires (Andela et al. 2017). The Collection 6 algorithm offers better detection of small fires and detects about 20% more burned area in Africa (Giglio et al. 2018). Burned area can be detected for many weeks after the fire occurred and takes advantage of temporal and spatial structural changes in fires (Andela et al. 2017). Since the Terra satellite was launched in December 1999 and the Aqua satellite was launched later in May 2002, the burned area trend combined from both satellites was quantified from 2003-2017 to reduce instrumental uncertainties. Only pixels marked as valid observations by the pixel-level quality assurance (QA) information associated with the MCD64A1 dataset were used.

The other burned area product was the monthly Global Fire Emissions Dataset Version 4 (GFED4s, 1997-2016) at 0.25° spatial resolution (Randerson et al 2012, Giglio et al 2013). This product used the 500-m MCD64A1 Collection 5.1 product as its primary data layer and incorporated small fires using active fire detections from the Tropical Rainfall Measuring Mission (TRMM), Visible Infrared Scanner (VIRS) and the Along-Track Scanning Radiometer (ATSR) (Giglio et al 2013).

Both the MODIS and GFED4s products depict a similar annual cycle of burned area (Fig. 3.1). Burned area reaches the maximum in December north of the equator and in August south of the equator. A fire year was defined as 5 months before and 6 months after the peak fire month (Archibald et al. 2009). The annual total burned area was calculated as 3 months before and 4 months after the peak fire month to include more than 90% of total burned area (van der Werf et al. 2008). Then, the linear trend of annual burned area was estimated using ordinary least squares

regression. The two-tailed Student's t-test was applied to assess whether the trend was statistically significant.

Next, the changes of burned area by land cover were examined. The annual MODIS land cover product (MCD12C1, 2001-2018) (Friedl and Sulla-Menashe 2015) at 0.05° resolution was used to identify the land cover type of each pixel in the study domain. There are total 17 land cover types classified based on the International Geosphere-Biosphere Programme (IGBP) classification scheme (Table 3.1). Seven major land cover types including evergreen broadleaf forest, deciduous broadleaf forest, mixed forest, woody savanna, savanna, grassland, and croplands (including croplands with natural vegetation mosaics) cover up to 97% terrestrial area of the study region (Fig. 3.2, Table 3.1), and about 96% burned area has occurred in these seven land cover types. The land cover type for each burning pixel was first assigned using the MCD12C1 and then the total burned area for each of the seven land cover types was spatially aggregated. Thus, the burned area in the study region was divided into seven sub-regions by land cover.

3.2.3 The Connected Component Labeling

A 3-D (latitude, longitude, time) connected-component labeling (CCL) algorithm was adopted to identify individual fires (Archibald and Roy 2009; Hernandez et al. 2015; He et al. 2017). It labels an individual fire based on the following rules. First, a fire ID is given to the first burned pixel when all pixels begin as unclassified. Then, pixels neighboring this labeled pixel including diagonals (8 possible neighbors) are identified. If any of these pixels are recorded as burned within 8 days of the date when the central pixel burns, they are labeled with the same fire ID (Archibald and Roy 2009). The CCL algorithm was repeated until all burned pixels were allocated with an individual fire ID. Eight days was used as a cut-off given the temporal duration window of the

original MODIS data (Giglio et al. 2018). Fire events were categorized into six different types: <100 ha (1 km2, small fire), 100-500 ha, 500-1000 ha, 1000-10000 ha, 10000-50000 ha and > 50000 ha (Archibald and Roy 2009). Due to the limited spatial resolution of the MODIS product, fires smaller than 25 ha were not considered in this study. Linear trends and their statistical significance in fire frequency and size were calculated in the same manner as the annual burned area detailed in section 3.2.2.

3.2.4 Random Forest Regression Model

A random forest regression model was applied to identify main factors associated with burned area variations in three land cover types (savannas, grasslands, and evergreen forest) that showed strong interannual variations and trends in burned area (see more in section 3.3.3). A single regression tree is a hierarchical classifier that predicts class membership by recursively partitioning data into more homogeneous subsets without assumptions concerning the statistical distribution of the data. It explains the variation in a given response variable by repeatedly splitting the input data into mutually exclusive and homogeneous groups, known as nodes. It continues to grow nodes until a maximal explanation of the response variable is achieved (Aldersley et al. 2011). However, a single output tree is sensitive to small differences in input datasets. As a bootstrapping procedure, random forest grows a bunch of regression trees to improve the predictive ability of a single regression tree and reduce overfitting (Aldersley et al. 2011). Random forest splits nodes in each tree using the best split subset among a randomly selected subset of the input variables. This ensures a high predictive power and keeps correlations among trees to a minimum. Though it does not include interpretations of physical processes, random forest can provide useful metrics indicating the relative importance of different predictor variables (Breiman and Cutler 2003).

Details regarding the spatially resolved data used in the model and the random forest sets are described next.

Nine variables were included in the conceptual model as explanatory variables, which are highly associated with fire activities documented in previous studies (Table 3.2). Annual precipitation (P) and DSL were calculated by the 3-hourly TRMM (3B42) precipitation product (Huffman et al. 2007). Annual precipitation was calculated starting 12 months before the peak fire month up to and including the peak fire month (total 13 months) (van der Werf et al. 2008). Daily rainfall estimates during a fire year within each grid were ranked and summed in descending order until at least 98% of annual rainfall was reached. The remaining number of days was the length of the dry season for that pixel (Guan et al. 2018). The 98% threshold was chosen to consider highly varied rainfall seasonality over different ecologic regions in Central Africa (Jiang et al. 2019). Fuel availability was quantified by the biweekly MODIS Terra NDVI product at 0.05° resolution (MOD13C1, 2000-present) (Didan 2015). A high NDVI value, referring to high vegetation productivity, indicates sufficient biomass favoring burning. The annual 250 m MODIS tree cover product (MOD44B, 2003-2017) (Dimiceli et al. 2015) was applied as well. Large tree cover is adverse for grass growth and thus reduces the accumulation of biomass supporting burning (Laris 2011).

Climate conditions, including surface wind speed, surface air temperature and specific humidity, from the monthly MERRA2 (1980-present) at 0.625°×0.5° resolution were used (Gelaro et al. 2017). Monthly mean weather variables during the fire season were calculated. Lightning strikes are a prominent ignition source (Aldersley et al. 2011). It was indirectly measured by monthly thunderstorm frequency using the 3-hour gridded infrared (IR) channel brightness temperature (T_b) dataset at 0.07° resolution (GridSat-B1, 1982-2016; Knapp et al. 2011). T_b

ranging between -40 to -70 °C was used to quantify thunderstorm activity in tropical latitudes (Raghavendra et al. 2018). Since total climatological lightning flash rates correspond well to changes in the number of storms (Williams et al. 2000; Cecil 2015), thunderstorm event records would provide reliable information about lightning strikes.

Human activities affect fuel load and continuity as well as ignition frequencies (Archibald et al. 2009). However, anthropogenic factors were limited to cropland extent in this study due to the lack of continuous records for road nets and population density. Cropland extent variations in different land cover types were calculated from the MODIS land cover product to quantify the impacts of agricultural expansion on fires. For easier comparison, all datasets used in this study were remapped on a 0.25° grid box using nearest neighbor resampling.

Grids with significant ($p < 0.1$) burned area trends were classified into low ($<30^{th}$ percentile) and high ($>70^{th}$ percentile) burned area to conduct the random forest analysis. There are fewer fires in the rainforest, so we extended the definition of high burned area ($> 65^{th}$ percentile) to enlarge the training data size. First, all datasets, including burned area, were randomly partitioned into training (90% of total data) and test (10% of total data) datasets in the random forest model. Then, 1000 trees were grown to guarantee model stabilization. Each tree used a different random bootstrap subset of predictor and burned area variables (about 66% of the training sets). For split conditions at each node, one third of the total number of predictor variables (i.e., 3 out of 9 variables) were recommended based on the estimate of the Gini impurity (Breiman and Cutler 2003). No further splitting was performed when nodes had less than five cases (Breiman 2001). The accuracy of the random forest regression was assessed by two methods (Breiman 2001; Mayr et al. 2018). One is the out-of-bag score, which calculates the squared correlation coefficient (r_o) between burned area predicted by the model trained by the 66% training sets and observations

from the rest of the training sets (33%). The other method calculates the Pearson correlation coefficient (r_p) between the burned area predicted by the test datasets and the model and observed burned area. The results provide relative contributions of individual physical variables and their critical values favoring or suppressing fire activities.

3.3 Results

3.3.1 Trends in Annual Burned Area

Annual mean burned area is shown in figures 3.3a-b. There is a high level of burned area over northern Central Africa (including the Central African Republic and southern Sudan) and southern Central Africa (including Angola and southern Democratic Republic of Congo) but less burning over the wet Congo rainforest in general. The maximum annual mean burned area reaches 96% within in a single grid box in northern Central Africa estimated by both burned area products.

Figures 3.3c-d display the spatial patterns of burned area trends from MODIS (2003-2017) and GFED4s (2003-2016). In northern and northwestern Central Africa, there is a significant negative trend ($p < 0.05$) in burned area, with a maximum decreasing rate of about 2% yr^{-1}. A mild, decreasing trend exists in southern Central Africa and parts of the Ethiopian highlands in the east. A significant increase in burned area occurs in the southwestern and northwestern edges of the Congo rainforest as well, which highlights the increasing risk of wildfire leakage into the rainforest.

Figures 3.3e-f show the interannual variations in burned area spatially averaged over northern and southern Central Africa. Though the GFED4s data detected more annual burned area than the MODIS data, both products observed similar interannual changes in burned area. The annual burned area has decreased dramatically by 1.8-2.5 Mha (10^4 km^2) yr^{-1} (p = 0.00) in the north,

particularly over tropical savannas and grasslands. Burned area decreased at a lower rate by 0.7-0.9 Mha yr^{-1} ($p < 0.1$) in the south.

3.3.2 Changes in Fire Frequency and Size

The histograms of fire frequency are shown in figures 3.4a. Small fires (<100 ha) contribute to 66% and 64% of total fire numbers north and south of the equator, respectively. Mega fires (>1000 ha) only count for about 5% in the north and 4% in the south. The annual fire frequency has decreased in the north at a rate of 2000 yr^{-1} (about 0.75% yr^{-1}), while it has varied little in the south (Figs. 3.4b-c). The significant decline in fire frequency in the north was mainly attributed to dramatic decreases in large fires (>100 ha). Fires larger than 500 ha have decreased at a rate of about 1.5% per year, and small fires have also slightly decreased at a rate of about 0.5% (Fig. 3.4d). Though there was no significant trend in fire frequency in the south, decreases also occurred with large fires larger than 1000 ha (Fig. 3.4e).

Next, changes in fire size were studied. In general, small fires contribute to 7.6% and 10% of total burned area in the north and south, respectively. Though large fires only count for about 30% of total fire events, they contribute up to about 90% of the total burned area (Fig. 3.5a). Significant decreases in the mean size of different fire categories have occurred in the north, particularly for mega fires larger than 50000 ha whose size decreased by 1.6% yr^{-1} (Fig. 3.5b). Small fires have slightly decreased by about 0.2% yr^{-1}. Mild, but non-significant, decreasing trends in large fire size have happened in the south as well (Fig. 3.5c).

3.3.3 Dependence of Burned Area Changes on Land Cover Types

Most fires happened over savannas (about 53%) and grasslands (about 30%), particularly in the north. A small percentage of burned area occurred over forested regions (about 10%) in the south (Fig. 3.6a). The long-term trends in annual burned area within savanna and grassland ecosystems are shown in figures 3.6b-c. Burned area has decreased significantly by 1.41-1.77 Mha yr^{-1} ($p < 0.01$) for the period 2003-2017 in the north and decreased by 0.48-0.83 Mha yr^{-1} in the south. Decreases in burned area in savannas and grasslands substantially contributed to the total decline in burned area in Central Africa (70-80% in the north, 69%-89% in the south). Though only about 4% burned area occurred in croplands, burned area decreased significantly by 0.31-0.53 Mha yr^{-1} ($p < 0.01$) in croplands north of the equator.

Figures 3.6d-e show the interannual variations in burned area in forested regions. Annual burned area slightly decreased by 0.07-0.08 Mha yr^{-1} in the north. Conversely, it increased significantly by 0.13-0.15 Mha yr^{-1} ($p < 0.05$) in the south. The increased burned area in forested regions was mainly attributed to increased burned area over mixed forests. In particular, burned area has increased in the rainforest edges by 0.012 Mha yr^{-1} ($p = 0.15$) (about 1.14% yr^{-1}) according to the MODIS product. To disentangle drivers of burned area changes in savannas, grasslands and rainforest edges, the random forest regression was applied next.

3.3.4 Possible Drivers of Burned Area Changes

First, all potential variables affecting burned area were assessed by calculating the climatological mean values for the period 2003-2017 over savannas and grasslands, and rainforest edges (Table 3.3). Savannas and grasslands, with more burnings and significantly decreasing burned area trends, are characterized by higher precipitation, shorter DSL and higher 2-m temperature during the fire season than those with less burnings. Though a short DSL implies a

short fire season. High precipitation enables relatively high vegetation productivity in the semi-dry ecosystem. Combining high temperature, these weather conditions might lead to more fires. The southern edge of the Congo rainforest, with a positive burned area trend, is characterized by a lower precipitation amount and longer DSL. Distributions of burned area grids in savannas and grasslands show that the decreasing burned area in savannas and grasslands may be attributed to a decrease in the occurrence of high burned area and an increase in the occurrence of low burned area (Figs. 3.7a-b). These results are consistent with the decreasing trends in the frequency and size of large fires. The increasing burned area over the southern Congolese rainforest edges may be attributed to an increase in the occurrence of high burned area (Fig. 3.7c).

According to the random forest analysis, NDVI ranks as the most important variable and is followed by DSL and precipitation in northern savannas and grasslands (Table 3.4). Grids with a higher NDVI value, shorter DSL and higher precipitation amount are favorable for high burned area (Figs. 3.8a-d). The random forest model characterized the training dataset well, with high out-of-bag correlation coefficient ($r_o = 0.91$), and predicted burned area using the test datasets with a high Pearson correlation coefficient ($r_p = 0.81$, $p = 0.00$). Comparisons between the composites of the three most important variables between 2003-2008 and 2012-2017 indicate that the decrease in the number of grids with high burned area is attributed to decreasing NDVI values and precipitation amount and increasing DSL (Figs. 3.8e-g). Positive correlation was observed between precipitation and NDVI ($r = 0.83$, $p = 0.0$), and negative correlation existed between DSL and NDVI ($r = -0.87$, $p = 0.0$). These results are consistent with previous studies indicating that lower moisture availability in arid or semi-arid ecosystems can decrease fuel build-up and burned area in the following years over longer time scales (van der Werf et al. 2008; Archibald et al. 2010; Bistinas et al. 2014; Lehmann et al. 2014).

The random forest model worked well for savannas and grasslands in the south with $r_o = 0.88$ and $r_p = 0.74$ ($p = 0.00$). NDVI, DSL and surface specific humidity are the three most important variables influencing fires. Similarly, a higher NDVI value and shorter DSL favor high burned area (Figs. 3.9a-d). Depending on the scenario, both positive and negative specific humidity anomalies can favor burning. Low humidity dries out plants, increasing the flammability of fuel. High humidity favors plant growth, increasing the amount of fuel. The mild decreasing trend in high burned area was mainly attributed to a decreased NDVI, longer dry season and slightly drier conditions (Figs. 3.9e-g). Longer DSL suppresses the accumulation of fuel, as seen by the negative correlation ($r = -0.57$, $p = 0.0$) between DSL and NDVI.

The random forest model was applied to the southern Congolese rainforest edge as well. Precipitation amount, surface wind speed and temperature significantly affect burned area ($r_o = 0.83$ and $r_p = 0.63$). Precipitation around 1585 mm, 10-m wind speed around 5.5 m/s and temperature around 295.3 K during the fire season facilitate fire activities (Figs. 3.10a-d The increasing high burned area in the southern edge of the Congo rainforest is attributed to reduced precipitation and increased temperature (Figs. 3.10e-g).

3.4 Conclusions and Discussions

Using advanced satellite observations, we found that burned area has decreased by 2.7-3.2 Mha yr-1 since the early 2000s in Central Africa. While previous analyses documented downward trends in the north but upward trends in the south (Andela et al. 2017), our results indicate that burned area has declined in both northern and southern Central Africa. Both fire frequency and size have declined, particularly for large fires (>100 ha) in the north. In addition, the decrease in fire frequency slightly outweighs the decrease in fire size.

Most of the burned area and decreased burned area trends occur in the savannas and grasslands. The highest level of fire activities observed in the savanna ecosystems are characterized by intermediate levels of precipitation and distinct wet and dry seasons favoring fuel build-up and dry out (van der Werf et al. 2008; Andela and van der Werf 2014). Most of the fire emissions originate from the savanna ecosystems and exert strong effects on atmospheric carbon dioxide and methane concentrations, which are crucial climate drivers (van der Werf et al. 2010). Decreases in the frequency of large fires and burned area in tropical savannas and grasslands may support global warming mitigation by acting as a carbon sink but would run counter to conservation objectives in fire-dependent ecosystems. Increasing burned area in forested areas was observed in the south, including the edge of the southern Congolese rainforest. The local intact rainforest has become increasingly fragmented since 2001 (Potapov et al. 2017). Forest edges are often juxtaposed with frequently burned pastures and degraded by selective deforestation (Cochrane and Laurance 2002). Increased burning may initiate a positive loop, which augments the rainforest fragmentation and affect its carbon storage (Cochrane et al. 1999; Nepstad et al. 1999).

We used the MODIS and GFED4s burned area products in this study. Boosted by better fire mapping algorithms, both burned area products have been improved to detect small fires. The MODIS product also provided information about changes in different categories of fires. Nevertheless, smaller fires < 25 ha were not included due to the constraint of imagery spatial resolutions. Poor measurements of these small fires would introduce large uncertainties when studying fire variations in regions such as croplands where smaller fires are relatively important (van der Werf et al. 2017; Giglio et al. 2018). These sub-grid small fires are likely to increase total burned area and carbon emissions by 35% globally (Randerson et al. 2012). Though it is impossible to quantify the contribution of these smaller fires to total burned area and fire events,

our results of fires between 25 and 100 ha in Central Africa suggest that this contribution is non-negligible to fire events but may be minor to total burned area. In addition, the diurnal cycle of individual fires cannot be documented by the fire products due to the constraint of imagery temporal resolution. Though the overall burned area trends were comparable from both the MODIS and GFED4s products, knowing more details about sub-grid fires and individual fires evolutions would facilitate our understanding of burned area changes and their physical mechanisms.

Our random forest analysis analytically revealed that the decreasing trend of burned area in savannas and grasslands was mainly attributed to changes in precipitation activities and vegetation fuel. A positive correlation between precipitation and NDVI and a negative correlation between DSL and NDVI indicate that moisture availability is crucial for fuel build-up in these semi-arid ecosystems. The decreased high burned area was mainly attributed to longer DSL, decreased precipitation and suppressed fuel build-up. Decreased precipitation and increased temperature were responsible for increased burned area at the southern rainforest edge. Increased agricultural activities were considered as the primary drivers of declining fire activities in the tropics and subtropics (Malhi et al. 2008; Andela et al. 2017). The machine learning method highlights the impacts of vegetation fuel and weather factors on local wildfire variability under the changing climate. To better examine anthropogenic effects on fires, additional continuous records of population density, agricultural practice, road density, and grazing intensity are required. Detailed vegetation-fire interaction and explicit physical mechanisms need further study via advanced land model simulations and causality analysis.

Tables and Figures

Table 3.1 Land cover types in Central Africa based on the IGBP classification scheme (Friedl et al., 2010).

Land cover type	Pixel number	Fractional coverage (%)
Water	21030	5.8
Evergreen needleleaf forests	0	0
Evergreen broadleaf forests	66474	18.3
Deciduous needleleaf forests	0	0
Deciduous broadleaf forests	6576	1.8
Mixed forests	5754	1.6
Closed shrublands	561	0.2
Open shrublands	2040	0.6
Woody savannas	27980	7.7
Savannas	104046	28.7
Grasslands	98249	27.1
Permanent wetlands	817	0.2
Croplands	18620	5.1
Urban and built-up lands	136	0.03
Cropland/natural vegetation mosaics	3873	1.1
Permanent snow and ice	0	0
Barren	6249	1.7

Table 3.2 Datasets of variables used as predictors in the random forest model.

Variables	Time	Spatial resolution	Temporal resolution	Dataset
precipitation (P) dry season length (DSL)	1998-present	0.25°	3-hourly	TRMM 3B42
NDVI	2000-present	0.05°	biweekly	MOD13C1
tree cover	2003-2017	250m	yearly	MOD44B
surface wind speed surface air temperature surface specific humidity	1980-present	0.625°×0.5°	monthly	MERRA-2
number of thunderstorm events	1982-2016	0.07°	3-hourly	GridSat-B1
cropland extent	2001-2018	0.05°	yearly	MCD12C1

Table 3.3 Long-term mean values of potential explanatory variables in different ecosystems for the period 2003-2017.

Land cover type	BA (%)	pre (mm)	DSL (day)	tree cover (%)	crop (%)	NDVI	T (K)	W (m/s)	q (g/kg)	number of thunderstorm events
SGN	21	923	269	3.7	5.5	0.47	295	4.3	12	5.5
SGN_{ST}	28	1043	263	3.7	7	0.52	298	4.0	13	5.9
SGS	21.9	1119	257	45.1	1.2	0.60	294	5.5	11	2.9
SGS_{ST}	21.6	1144	259	45.5	1.0	0.61	297	5.5	11	3.2
EGS	3.2	1782	215	58	0.18	0.76	296	5.7	10	4.8
EGS_{ST}	4.0	1755	217	62	0	0.77	296	5.5	10	5.2

Note: SG–savannas and grasslands; EG–evergreen forest; N/S–northern/southern Hemisphere; "ST" refers to the grids with significant burned area trends. BA–burned area. pre–precipitation. DSL–dry season length. crop–cropland extent. T–surface air temperature. W–surface wind speed. q–surface specific humidity. The definition and calculation for each variable are detailed in section 2.4.

Table 3.4 Summary of relative contributions (%) of each explanatory variable for savannas and grasslands north and south of the equator, and the southern rainforest edges estimated by the random forest classification.

Land cover type	pre (mm)	DSL (day)	tree cover (%)	crop (%)	NDVI	T (K)	W (m/s)	q (g/kg)	number of thunderstorm events
SGN_{ST}	**13.2**	**16.7**	6.4	6.7	**25.6**	5.7	6.6	11.3	8.1
SGS_{ST}	11.3	**15.6**	9.4	2.5	**22.5**	5.2	5.9	**14.3**	13.2
EGS_{ST}	**19.9**	11.1	5.0	0.0	11.2	**13.8**	**14.1**	13.1	11.9

Note: The values in bold represent the three most important variables affecting burned area. Within each region, the summation of each variable's contribution is close to 100%. SG–savannas and grasslands; EG–evergreen forest; N/S–northern/southern Hemisphere; "ST" refers to the grids with significant burned area trends. The variables "pre", "DSL", "crop", "T", "W" and "q" are defined as in table S2.

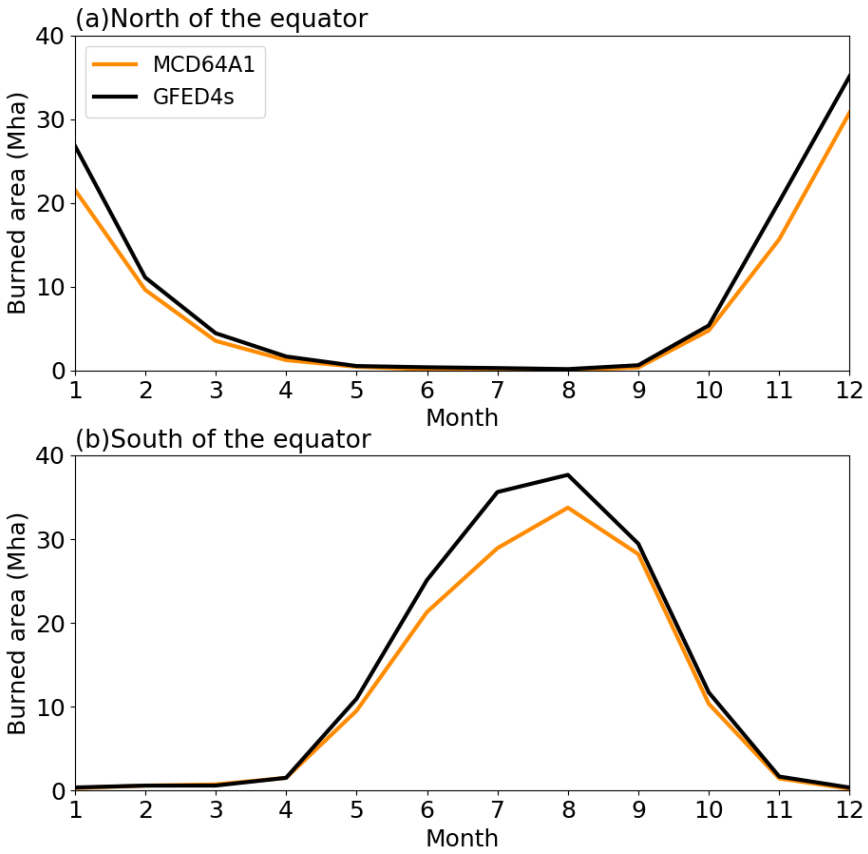

Figure 3.1 Seasonal cycles of burned area in (a) north of the equator and (b) south of the equator over Central Africa based on satellite observations from the MODIS (orange lines, 2003-2017) and GFED4s (black lines, 2003-2016) burned area products.

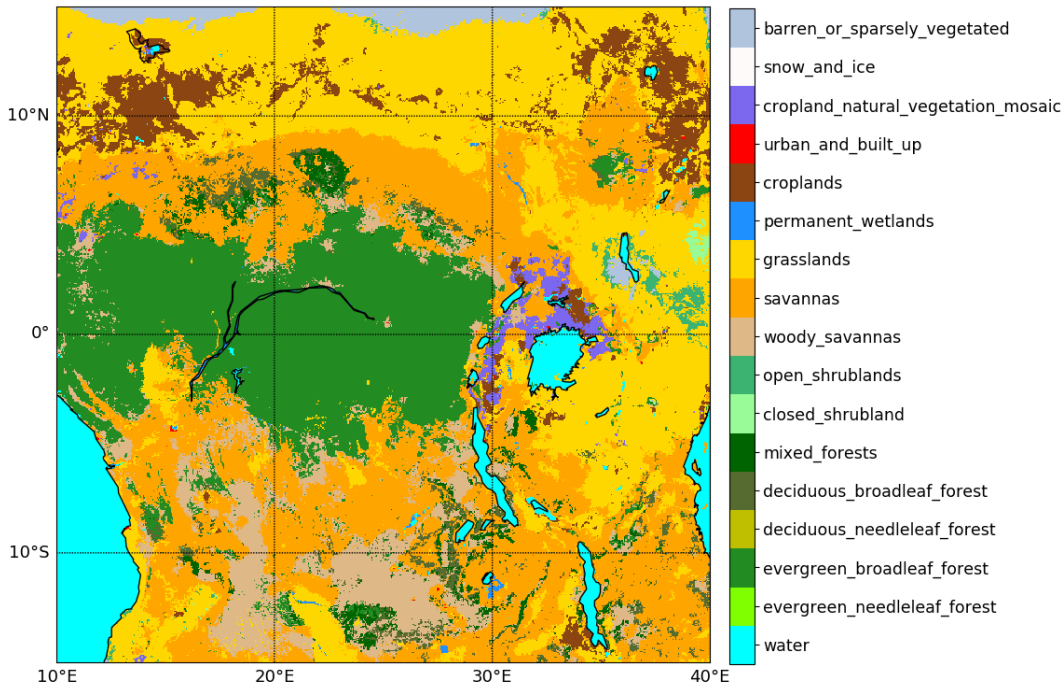

Figure 3.2 Land cover types over Central Africa in 2010 estimated from the MODIS land cover product (MCD12C1) based on the IGBP classification scheme (Friedl et al., 2010).

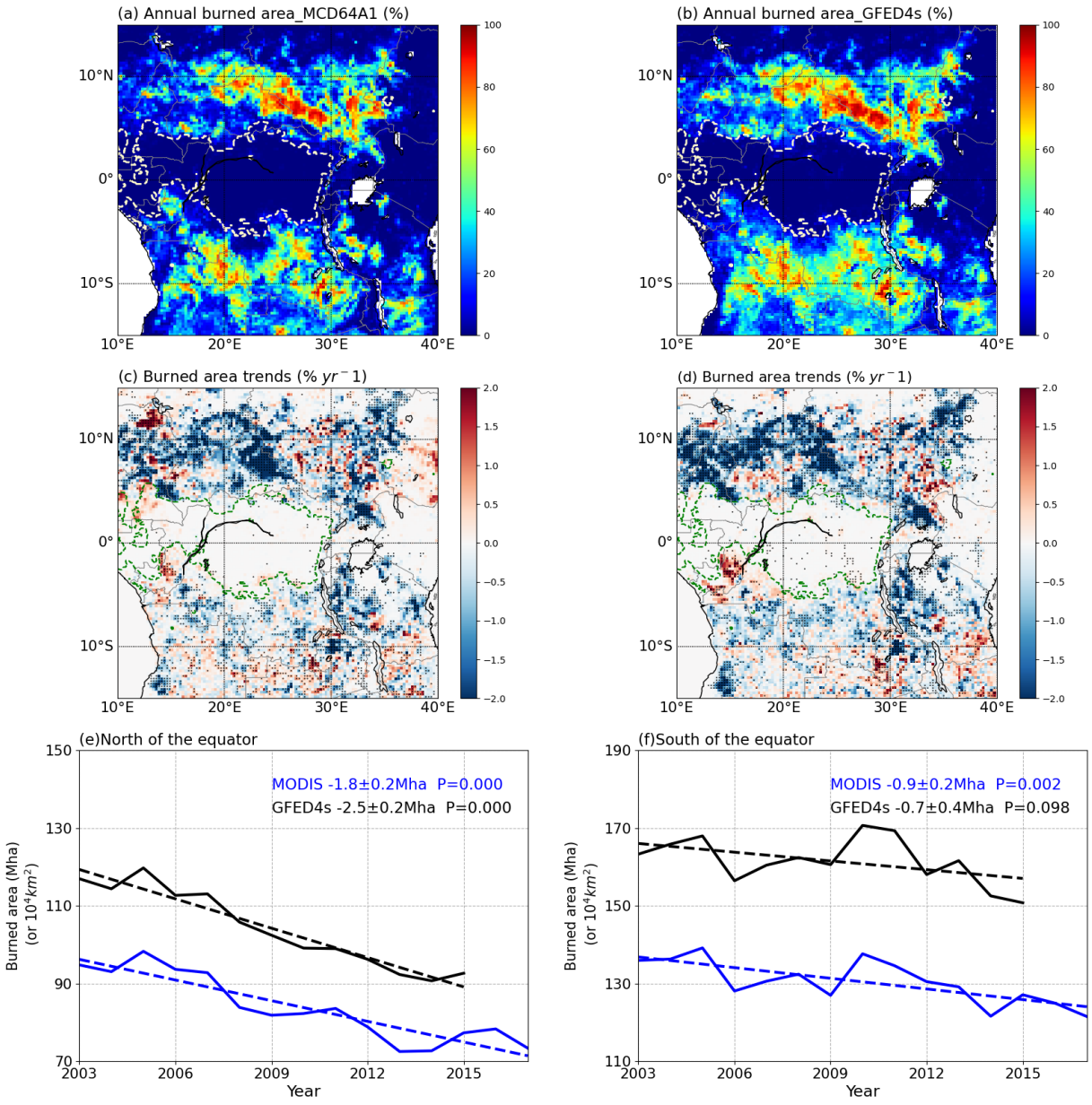

Figure 3.3 Spatial patterns of annual mean burned area from (a) MODIS and (b) GFED4s, and linear trends of annual mean burned area for the period 2003-2016/17 from (c) MODIS and (d) GFED4s. The dashed line delineates the boundary of the Congolese rainforest. Grid boxes with black dots have a significant trend at $P < 0.05$. Regionally aggregated interannual variations (solid line) and linear trends (dashed line) of annual mean burned area: (e) north and (f) south of the equator estimated from the MODIS and GFED4s. The linear trend and its significance level P are shown.

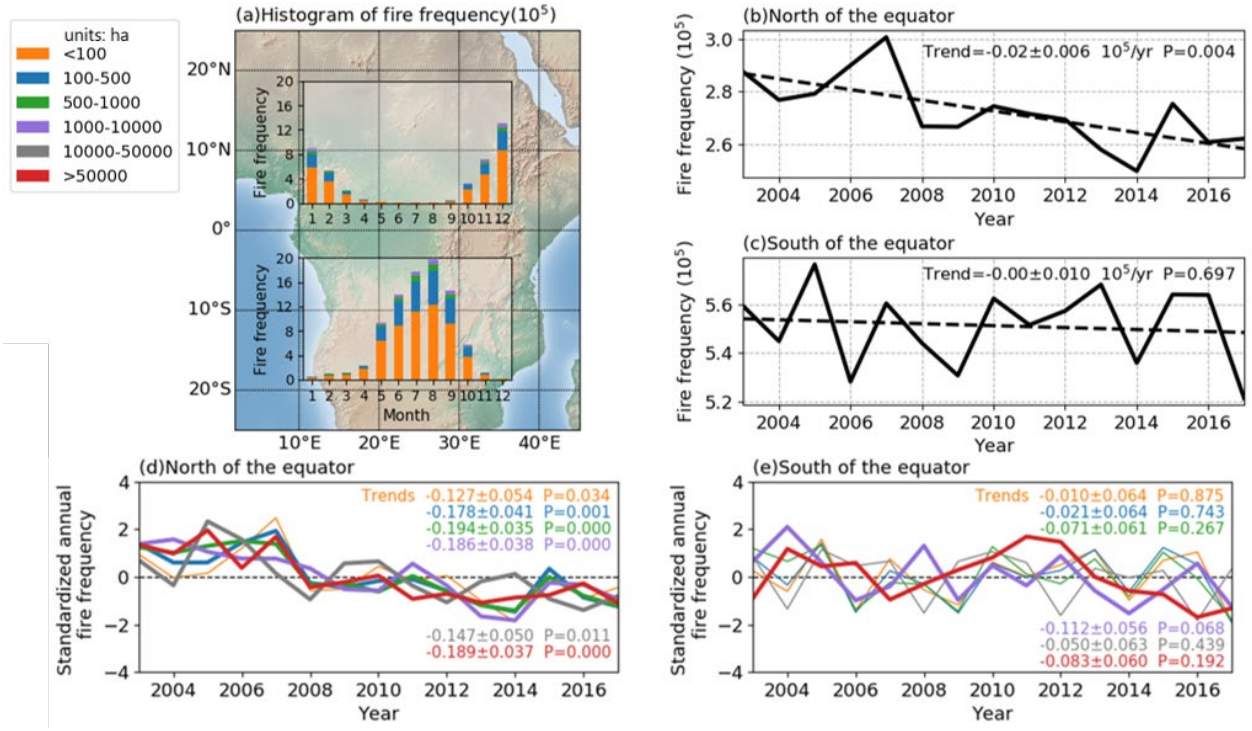

Figure 3.4 Histogram and variations of fire frequency over Central Africa estimated by the MODIS product for the period 2003-2017. (a) The histogram of fire frequency for different fire categories. Interannual variations and linear trends of total fire frequency (b) north and (c) south of the equator. Interannual variations and linear trends of standardized fire frequency in different categories (d) north and (e) south of the equator. Linear trends and significance levels are shown.

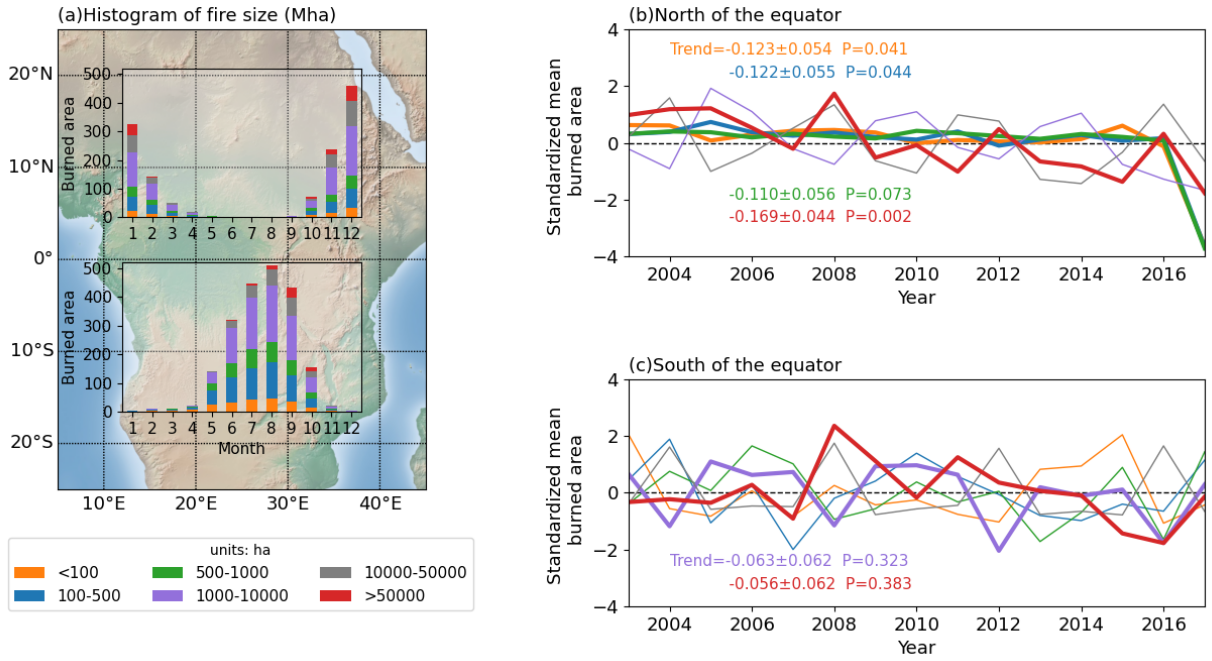

Figure 3.5 Histogram and variations of fire size over Central Africa estimated by the MODIS product for the period 2003-2017. (a) The histogram of contributions from different fire categories to total burned area. Interannual variations and linear trends of standardized mean fire size in different categories (b) north and (c) south of the equator. Linear trends and significance levels are shown.

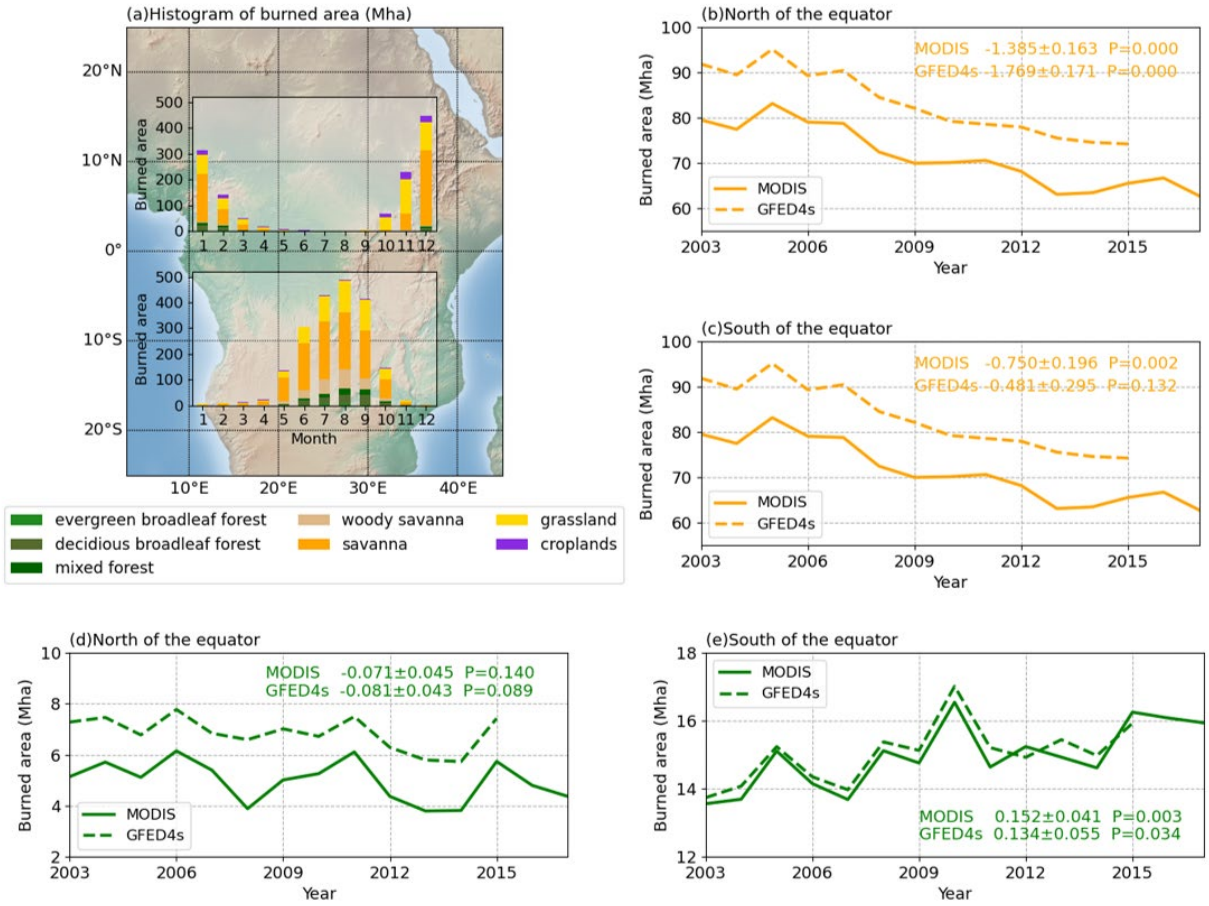

Figure 3.6 Histogram and variations of burned area in different land cover types over Central Africa estimated by the MODIS and GFED4s for the period 2003-2017. (a) The histogram of burned area for different land cover types. Interannual variations (solid line) and linear trends (dashed line) of burned area in savannas and grasslands (b) north and (c) south of the equator. Interannual variations and linear trends of burned area in forested regions (d) north and (e) south of the equator. Linear trends and significance levels are shown.

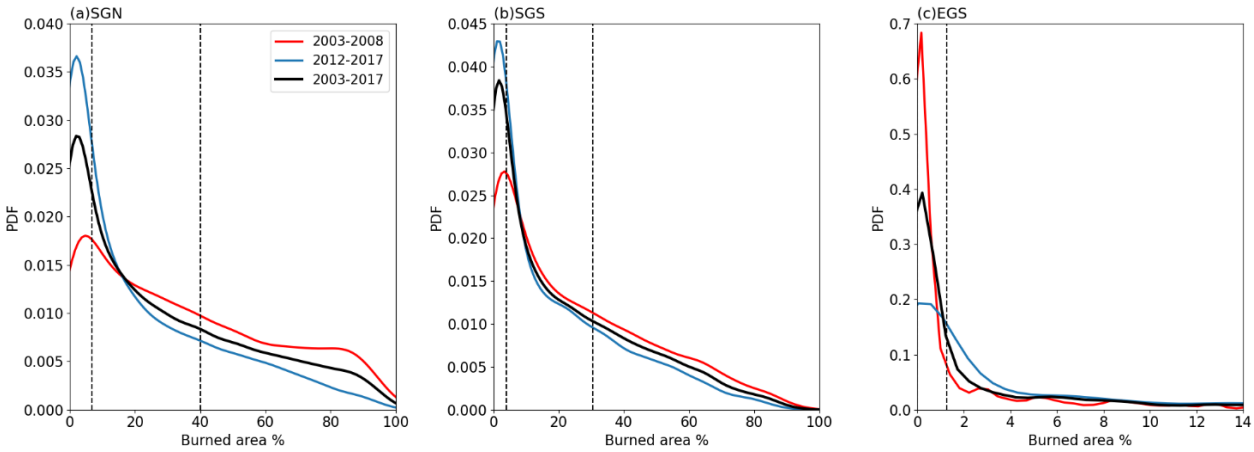

Figure 3.7 Probability density function (PDF) of burned area for grids with significant trends in savannas and grasslands (a) north and (b) south of the equator, and (c) the southern Congolese rainforest edges from the MODIS product for the period 2003-2017. PDF is calculated by kernel density estimation (KDE) to demonstrate the distribution of the variable. The dashed lines mark the 30th and 70th percentile of burned area. The dashed line in (c) marked the 65th percentile of burned area.

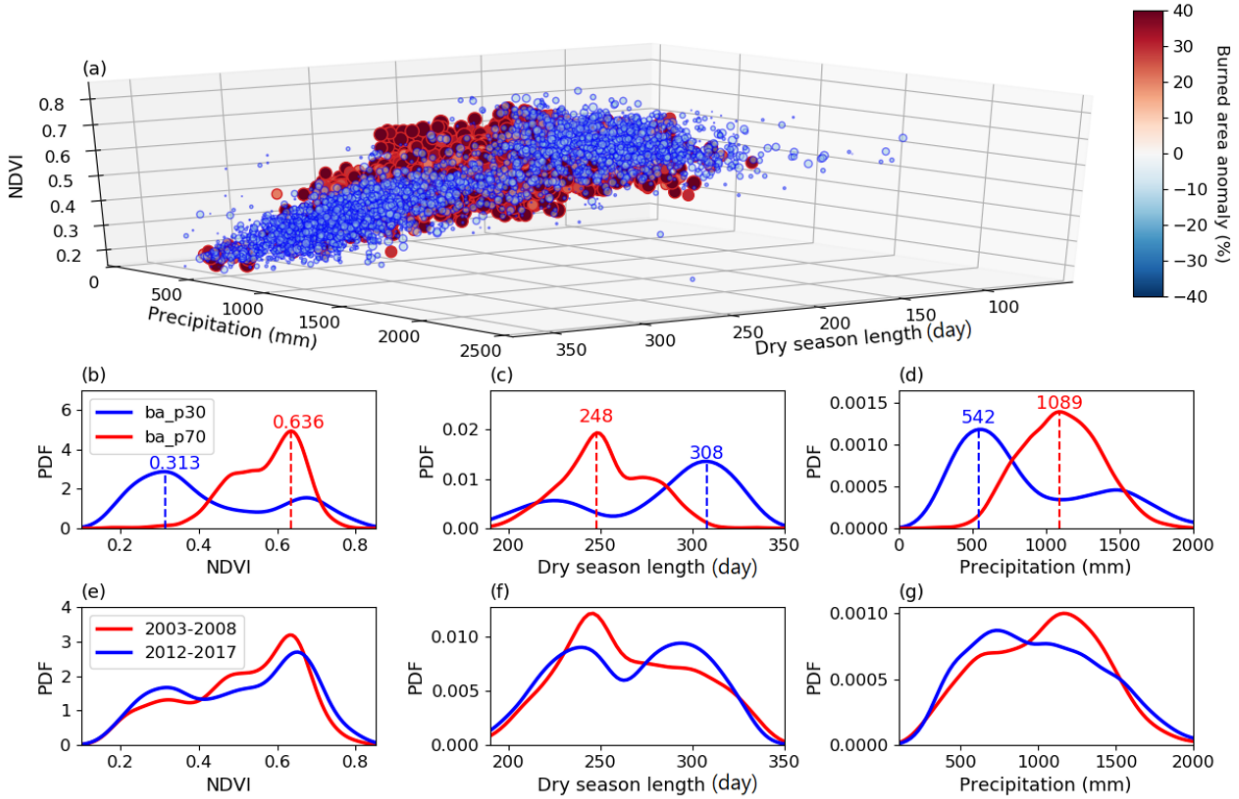

Figure 3.8 Relationships between annual burned area from MODIS and NDVI, dry season length (DSL), and precipitation amount over savannas and grasslands in northern hemisphere for the period 2003-2017. (a) NDVI versus precipitation amount and DSL against burned area. Small circles shaded in blue presents low burned area. Large circle shaded in red presents high burned area. Probability density functions (PDF) of (b) NDVI, (c) DSL, and (d) precipitation amount for high (red) and low (blue) burned area. The critical values are marked. Comparisons of (e) NDVI, (f) DSL and (g) precipitation between 2003-2008 (red) and 2012-2017 (blue). PDF is calculated by kernel density estimation (KDE) to demonstrate the distribution of the variable. "ba_p30" and "ba_p70" refer to burned area lower than the 30th percentile and higher than the 70th percentile of all burning grids, respectively.

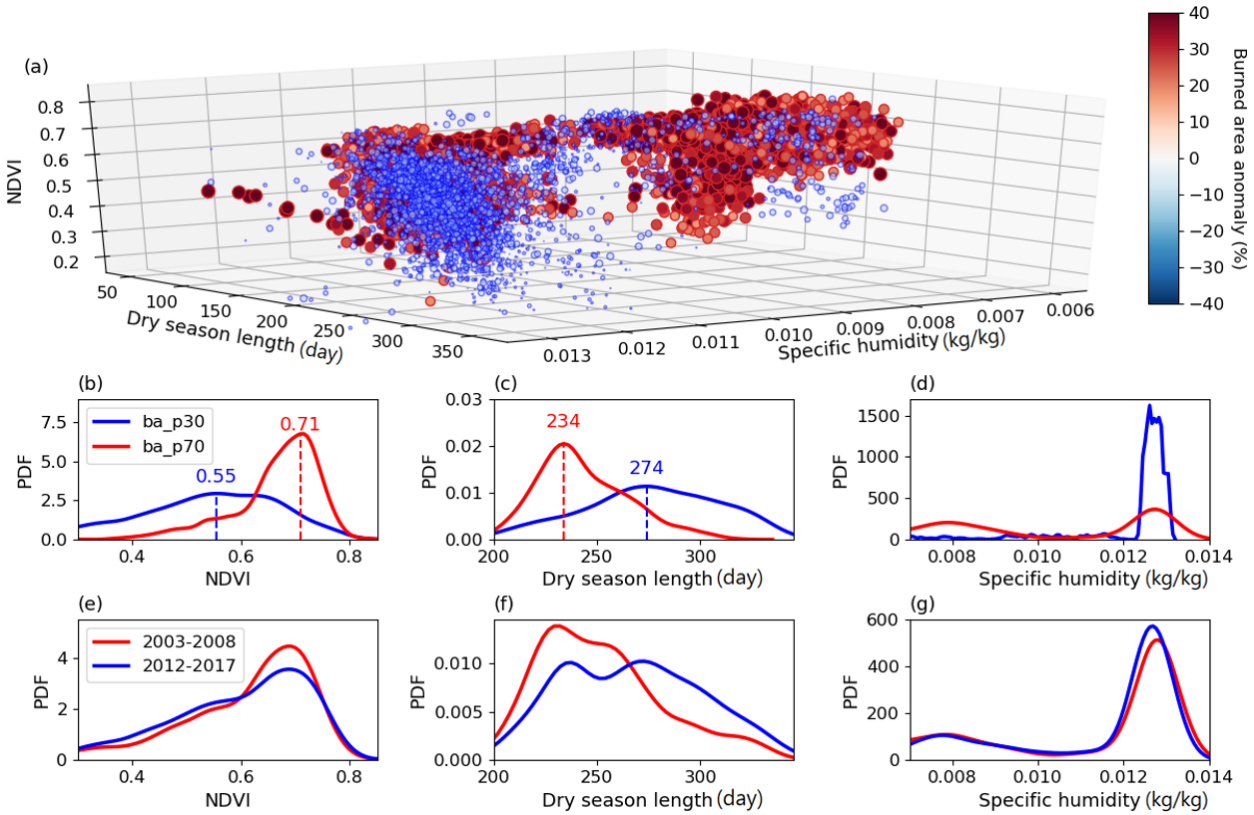

Figure 3.9 Relationships between annual burned area from MODIS and NDVI, DSL, and specific humidity over savannas and grasslands in southern hemisphere for the period 2003-2017. (a) NDVI versus DSL and specific humidity against burned area. Small circles shaded in blue presents low burned area. Large circle shaded in red presents high burned area. Probability density functions of (b) NDVI, (c) DSL and (d) specific humidity for high (red) and low (blue) burned area. The critical thresholds are marked. Comparisons of (e) NDVI, (f) DSL, and (g) specific humidity between 2003-2008 (red) and 2012-2017 (blue). "PDF", "ba_p30" and "ba_p70" are defined as in figure 3.8.

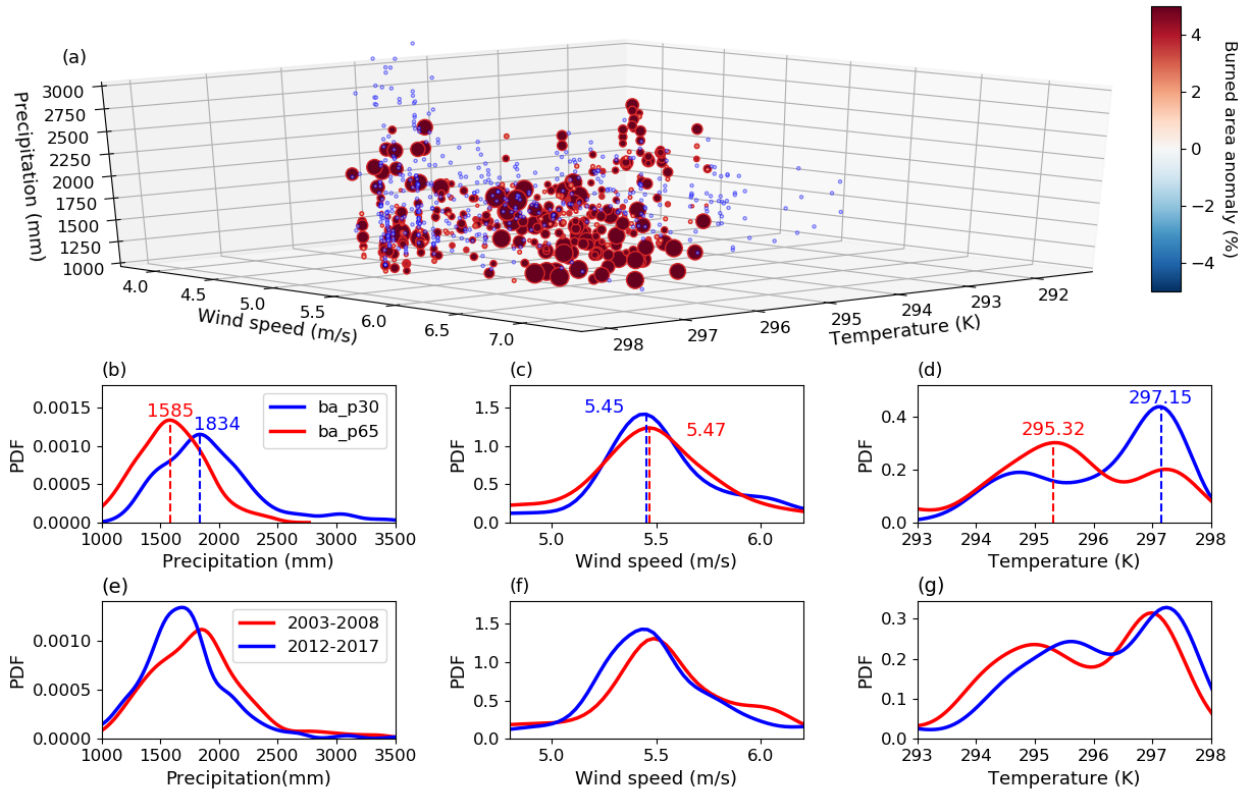

Figure 3.10 Relationships between annual burned area from MODIS and precipitation amount, wind speed and temperature in the southern rainforest edges for the period 2003-2017. (a) Precipitation amount versus wind speed and temperature against burned area. Small circles shaded in blue presents low burned area. Large circle shaded in red presents high burned area. Probability density functions of (b) precipitation amount, (c) wind speed and (d) temperature for high (red) and low (blue) burned area. The critical thresholds are marked. Comparisons of (e) precipitation amount, (f) wind speed and (g) temperature between 2003-2008 (red) and 2012-2017 (blue). "PDF" and "ba_p30" are defined as in figure 3.8. "ba_p65" refers to burned area higher than the 65th percentile of all burning grids.

Chapter 4 Increasing Influence of Indian Ocean Dipole on Precipitation over Central Equatorial Africa

4.1 Introduction

Central equatorial Africa (CEA) hosts the world's second largest rainforest. Disturbances in interannual or seasonal rainfall not only affect the hydrological cycle, but also have far-reaching impacts on the global carbon cycle (James et al. 2013; Mitchard 2018). A widespread long-term drying trend has been observed in the Congo Basin since the 1980s (Zhou et al. 2014; Hua et al. 2016; Jiang et al. 2019). The drying has been associated with sea surface temperature (SST) anomalies, with declined moisture transport from the Indian Ocean during April-June (Hua et al. 2016). The suppressed ascent over the basin was induced by the westward extended Walker Circulation caused by the La Niña-like SST anomalies during 1980-2014 (Ma and Zhou 2016; Hua et al. 2018). Understanding connections between CEA rainfall and tropical oceans is thus important but challenging due to complex land-atmosphere-ocean interactions, which vary by season and are complicated by teleconnections among oceans (Otto et al. 2013; Bush et al. 2020).

Influences of tropical oceans on CEA rainfall are seasonally specific. The El Niño Southern Oscillation (ENSO) refers to the irregular periodic variations in SSTs over the tropical Pacific Ocean and zonal pressure gradient between tropical western and eastern Pacific Ocean (Wang 2018). It is negatively correlated with rainfall anomalies in western equatorial Africa during February-August. Positive phase (El Niño) would thus suppress rainfall. The Indian Ocean Dipole (IOD) presents interannual variation in the difference between SST anomalies of tropical western and eastern Indian Ocean featured with changes in zonal winds along the equatorial Indian Ocean (Saji et al. 1999). Positive IOD modes refer to the warmer western Indian Ocean and are associated with reduced rainfall during dry seasons in CEA, but increased rainfall during September-

November and decreased rainfall during March-May in eastern Africa (Todd and Washington 2004; Nicholson and Dezfuli 2013; Otto et al. 2013; Shaaban and Roundy 2017). High tropical Atlantic SSTs could enhance CEA rainfall in dry seasons (Otto et al. 2013). In addition to the teleconnections between tropical SSTs and CEA rainfall, active interactions among different climate modes like ENSO and IOD exist and can enhance or suppress their individual effects on rainfall (Nicholson 2000b, 2001; Williams and Hanan 2011). Simple linear correlation analysis has been commonly used in previous work to quantify the impacts of individual oceanic modes on CEA rainfall (Todd and Washington 2004; Nicholson and Dezfuli 2013), while the confounding effects of different modes are often not considered. Hence, previous results might underestimate or overestimate a single mode's independent influence without isolating potential contributions from other modes.

Aside from tropical SSTs, CEA rainfall is also affected by intra-seasonal variabilities. The Madden Julian Oscillation (MJO) is the dominant sub-seasonal mode (20-100 days) in the tropics (Wilson et al. 2013). The MJO becomes the strongest in boreal winter and spring and reaches its second peak in boreal summer (Zhang and Dong 2004). It affects tropical precipitation year-round and can cause 20-50% daily precipitation variability within a single season (Berhane et al. 2015). At longer time scales, the MJO has contributed ~14% to the CEA drying trend and interacts with other climate modes by either triggering a large-scale mode like the ENSO or mediating its teleconnections (Zhang 2005; Hoell et al. 2014; Raghavendra et al. 2020). In reverse, the MJO is modulated by the ENSO and IOD, for it is most active in the Indian and western Pacific oceans (Zaitchik 2017). Considering interactions between MJO and climate modes is more useful for long-range weather predictions than considering individual modes alone (Roundy et al. 2010). Shimizu et al. (2017) suggested that ENSO's impact on South American rainfall depends on the

MJO. Recent studies raised the possibility that MJO might be the mechanism for ENSO to affect Eastern African rainfall (Pohl and Matthews 2007; Berhane 2016). Positive IOD events are associated with suppressed MJO convection, while negative IOD events are associated with enhanced MJO convection in the Indian Ocean (Kug et al. 2009; Wilson et al. 2013). Covariance of MJO activity with the IOD could impact its influence on African rainfall. However, few studies have addressed this topic so far (Zaitchik 2017).

Potential secular variations in the relationships between climate modes and rainfall in monsoon regions and watershed have been noted (Kumar et al. 1999; Nicholson 2001; Yadav et al. 2009) but are seldom addressed in CEA due to sparse gauge density. By taking the advantage of a newly created gauge-based precipitation dataset (Nicholson et al. 2018), this study applied partial correlation and regression analyses to quantify IOD's impact on rainfall in CEA (10°E-32°E, 8°N-10°S). It presents evidence for a robust positive partial correlation between CEA rainfall and IOD during the September-December (SOND) rainy season. Here we aim to address three questions: 1) how is IOD associated with CEA rainfall amount, frequency, and intensity? 2) what are the physical processes of IOD's impact on rainfall? 3) have the changes in IOD affected the boreal rainfall trend? The results would help to disentangle oceanic impacts on CEA rainfall and to understand rainfall variations, thus improve regional precipitation predictions.

4.2 Data and Methods

4.2.1 Rainfall Datasets

To quantify the correlation between precipitation and climate modes, a newly created gauge-based monthly precipitation product at 2.5° spatial resolution (NIC131, 1921-2014) covering the Congo Basin and surrounding regions was used (Nicholson et al. 2018b). The NIC131 was gridded

by combining the gauge data at 1,826 individual stations, which is much greater than any existing precipitation datasets over Central Africa, via a statistical reconstruction approach to provide reliable records. To bolster the robustness of the results, another long-term observational monthly rainfall dataset from the GPCC v2018 (1891-2016) at 1.0° spatial resolution was utilized as well (Schneider et al. 2018).

Given limited temporal and spatial resolutions of both observational datasets, a daily precipitation dataset from the Climate Hazards Group Infrared Precipitation with Station Data (CHIRPS2, 1981-present) at 0.25° resolution (Funk et al. 2015) was used. Merged with African gauge data and thermal infrared observations from geostationary satellites, CHIRPS2 can provide good spatial coverage and temporal records for the study region. It has been validated as the best satellite-derived rainfall product for CEA (Nicholson et al. 2019). CHIRPS2 was used to quantify associations between climate modes and rainfall frequency, intensity, and extreme rainfall events.

A rainy day was defined when daily rainfall amount is larger than 1mm. Rainfall frequency was defined as the percentage of rainy days during study period (Guan et al. 2018; Dai et al. 2020). Rainfall intensity, defined as precipitation rate, was only calculated for rainy days receiving rainfall at least 1 mm per day. Extreme wet and dry rainfall events were identified as those exceeding the 75th and those lower than the 25th percentile of basin-wide daily rainfall during 1981-2019 (Shimizu et al. 2017).

4.2.2 Ocean SST and MJO Indices

Four monthly SST indices from the National Oceanic and Atmospheric Administration (NOAA) were used (Table 4.1): The Oceanic Niño index (ONI; 1950-present), the Dipole Mode Index (DMI; 1870-present; Saji and Yamagata 2003a), the Tropical Northern Atlantic Index (TNA; 1948-present) and Tropical Southern Atlantic Index (TSA; 1948-present; Enfield et al. 1999).

Positive ONI values indicate El Niño events. Positive DMI values indicate the warmer western Indian Ocean than the east and positive IOD events. Positive values for TNA and SNA indicate high SSTs in corresponding regions. The monthly surface wind data from the Comprehensive Ocean-Atmosphere Data Set (COADS, 1960-present) observation at 1.0° resolution was used as an auxiliary product to estimate oceanic modes (Freeman et al. 2017).

To estimate the status of the MJO, the Real-time Multivariate MJO index (RMM, 1974-present; Wheeler and Hendon 2004) based on the empirical orthogonal function analysis of zonal wind and outgoing longwave radiation (OLR) from the Center for Australian Weather ad Climate Research was used. An active MJO day is identified when RMM amplitude is larger than 1 (Raghavendra et al. 2020). A single MJO event can experience eight phases as the convection starts around the western Indian Ocean and propagates eastward (Zhang 2005). This index is not a perfect or a complete representation of MJO signal but has demonstrated usefulness. The convection during different RMM phases was estimated by the daily OLR (1974-2019) data at 2.5° resolution from NOAA as well (Liebmann and Smith 1996).

To quantify possible impacts of IOD and MJO on large-scale circulations, vertical motion (omega), horizontal winds, and specific humidity were provided by the 3-hourly MERRA2 (1980-present) at 0.625°×0.5° resolution (Gelaro et al. 2017). With improved and updated data assimilation and observing systems, the MERRA2 reanalysis represents the currently state-of-the-art reanalysis, and its use of a modern satellite database is expected to improve the data quality over observation-limited regions such as CEA (Molod et al. 2015, Hua et al. 2016). For example, it can better capture the major hydrological characteristics and large-scale circulation patterns over CEA than other reanalysis products (Hua et al. 2019).

4.2.3 Statistical Methods

The independent associations between precipitation and tropical SSTs were quantified using partial correlation analysis. The partial correlation analysis was conducted during four seasons. All variables were detrended before the analysis was applied. Two-sided Pearson test was applied to assess whether correlations were statistically significant. Composite analysis was further applied to analyze rainfall variations and potential modifications in synoptic dynamics. Composites of anomalies in rainfall amount, frequency, intensity, extremes, daily OLR, omega, horizontal winds, and specific humidity were compared for different IOD and RMM phases. Significance of the difference was tested by Monte Carlo simulation and two-tailed Student t test. Ten positive IOD events (1982, 1983, 1994, 1997, 2006, 2008, 2011, 2012, 2018, 2019) and ten negative IOD events (1981, 1989, 1992, 1996, 1998, 2001, 2005, 2010, 2014, 2016) were identified based on the method of Saji and Yamagata (2003b): 1) DMI, zonal wind over Indian Ocean (Ueq, 70°E-90°E, 5°N-5°S), and SST anomaly (SSTA) over the eastern Indian Ocean (90°E-110°E, 0°-10°S) were detrended. 2) A 3-month running mean was applied. 3) DMI, Ueq, and SSTA were all required to exceed 0.5 standard deviation threshold for at least 3 months.

4.3 Results

4.3.1 Associations of the IOD with CEA Rainfall

In general, the tropical Indian and Pacific Oceans have higher correlations with CEA rainfall than the other oceans, which implies potential stronger impacts on precipitation (Table 4.2). Negative correlation between precipitation and ONI was observed during June-November, indicating that positive ENSO events are associated with suppressed precipitation. The DMI is positively correlated with precipitation, particularly during September-November when the

correlation coefficient reaches 0.68 ($P < 0.01$). Positive IOD events are thus associated with enhanced precipitation. Correlations between CEA rainfall and tropical Atlantic SSTs are relatively weak. The TNA is negatively correlated with precipitation during March-May. The tropical southern Atlantic SST is not directly correlated with CEA rainfall. Given the strongest correlation between precipitation and DMI during September-November, the study mainly focused on analyzing IOD's potential impacts on CEA rainfall during SOND. December was also included, for there is a significant correlation in winter and IOD events can last to December (Saji et al. 1999).

Figure. 4.1 displays associations between the DMI and rainfall amount, frequency, and intensity. The DMI is positively correlated with basin-wide rainfall amount except the northwestern basin (Fig. 4.1a). Similar spatial patterns are observed by the NIC131 and GPCC data (Fig. 4.2). Discrepancies over the central and southern basin might be attributed to the differences in data sources, resolutions, and interpolation methods of these three rainfall products. The positive correlation is seen between the DMI and rainfall frequency as well (Fig. 4.1b). DMI is positively correlated with rainfall intensity in the southern and eastern basin but is negatively correlated with intensity in the northwest (Fig. 4.1c), resulting in an overall weak association with rainfall intensity. Consistent with the spatial patterns, regionally averaged rainfall amount is positively correlated with DMI ($R = 0.69$, $P < 0.01$). The coefficient between rainfall frequency and DMI reaches 0.65 ($P < 0.01$) (Fig. 4.1d).

Next, composites of anomalies in rainfall amount, frequency, intensity, and the frequency of extreme events were compared between positive and negative IOD events (Fig. 4.1e). Regional mean precipitation amount is significantly enhanced by ~3.4% during positive IOD events but is suppressed by ~3% during negative IOD events. Rainfall frequency is increased by ~3% during

positive IOD events but is decreased by ~2% during negative IOD events. Given that the relative change in rainfall amount (A) can be attributed to the relative changes in rainfall frequency (F) and intensity (I) ($\frac{dA}{A} = \frac{dF}{F} + \frac{dI}{I}$), the increased rainfall amount is thus mainly attributed to the increased rainfall frequency during positive IOD events. Although there is less change in rainfall intensity during active IOD events, the frequency of extreme wet rainfall events is evidently increased by 4% and the frequency of extreme dry events is decreased by 5% during positive IOD events.

Seasonal phase locking is an important characteristic of IOD. An IOD event intensifies after June, peaks in October, and rapidly decays during November-December (Saji et al. 1999). Impacts of IOD on rainfall was further estimated during different months. Figure 4.1f shows that the changes in rainfall amount and frequency induced by IOD are highest during October and November. Rainfall amount and frequency increase by ~9% and ~7% during positive IOD events in October, which is consistent with IOD's evolution.

4.3.2 Impacts of IOD on MJO Activity and Mean Circulations

To investigate possible physical processes of IOD's impacts on CEA rainfall, covaried MJO activity and modifications in mean circulations were estimated. The MJO is most active during SOND, when active MJO days dominate about two thirds of the Time (Table 4.3). First, we composited rainfall based on days with active MJO and days without active MJO during positive and negative IOD events respectively (Fig. 4.3a). It is shown that rainfall amount increases by ~4% with active MJO, while only increases by ~2% without active MJO during positive IOD events. Consistently, rainfall frequency and the frequency of extreme wet events increase by ~3.5% and ~4.5% during active MJO days. MJO activity is likely a crucial process through which IOD impacts CEA rainfall. During negative IOD events, MJO activity slightly alleviates the IOD's

suppression effect on precipitation, as the decrease in rainfall amount reaches ~3.5% without MJO impacts. Spatial maps of rainfall variation, which were calculated as the differences in composite rainfall with or without active MJO between positive and negative IOD events, illustrate that MJO could significantly increase rainfall amount over central and southern CEA (Figs. 4.3b-d). In general, the net effect of MJO tends to enhance precipitation over CEA, and the impact is stronger during positive IOD events.

Next, differences in composite vertical motion, horizontal wind, and specific humidity between positive and negative IOD events changes were assessed. CEA rainfall is influenced by the Walker Circulation (Hua et al. 2016; Hua et al. 2018) with its upward branch located over CEA and two downward branches over the western Indian Ocean around 40°E–55°E and the Gulf of Guinea. Moisture converges in the lower troposphere, and the low-level easterly jet (800-600hPa) favors convection developments over CEA (Fig. 4.4). During positive IOD events, the Walker Circulation becomes weaker (Figs. 4.3e, 4.5). More moisture is transported and accumulated at lower and middle troposphere over CEA via abnormal easterlies (Figs. 4.3e-g, 4.6e, 4.7e). During negative IOD events, the Walker circulation is strengthened and westward extended (Fig. 4.5). The mid-level troposphere becomes drier over CEA (Fig. 4.6). Figure 4.3f shows the differences in composite variables with active MJO. The moistening in the lower and middle troposphere during positive IOD events is more constrained over eastern Africa and the western Indian Ocean. And the easterly jet is weakened particularly during negative IOD events and thus is less favorable for convection systems (Figs. 4.3f, 4.7d).

In view of MJO's impacts on synoptic dynamics during IOD events, IOD modifications on MJO activity were analyzed. Active MJO days were clarified as wet or dry phases if CEA rainfall was significantly enhanced or suppressed. In this way, phases 1 and 2 (MJO convection over the

western Indian Ocean) are wet phases, while phases 4, 5 and 6 (MJO convection over the eastern Indian Ocean and Maritime Continent) are dry phases. Compared with neutral IOD events, there are more wet phases days during positive IOD events, and slightly more dry phases days during negative IOD events (Table 4.3). Composite synoptic dynamics anomalies for wet MJO phases during positive IOD events indicate that low- and mid-level easterly anomalies are stronger, the lower atmosphere is moister over the western and central Indian Ocean and the Walker Circulation is much weakened, resulting in stronger convection over CEA (Figs. 4.8e-h). During negative IOD events, increased convection is constrained over eastern Africa attributed to MJO (Figs. 4.8i-l). For dry phases, the stronger subsidence limb of the Walker Circulation occurs eastward over the central Indian Ocean and the abnormal low and mid-level westerlies become stronger over both CEA and tropical Indian Ocean during negative IOD events. As a result, slightly increased moisture is observed above CEA and MJO's suppression effect on convection over CEA is weakened (Fig. 4.9).

4.3.3 Impacts of Changing IOD on CEA Rainfall Trend

A warmer tropical Indian Ocean was projected by climate models and observations showed faster SST warming in the western Indian Ocean than in the east since the 1960s (Vecchi and Soden 2007; Cai et al. 2013). Accompanying this warming trend, an increasing DMI has been documented. The frequency and intensity of positive IOD events have increased during the 20th century (Abram et al. 2008; Cai et al. 2009; Cai et al. 2014). This raises a question regarding whether IOD impacts on CEA rainfall would also change?

To quantify potential secular variation in the association between IOD and CEA rainfall, partial correlation analysis between DMI and rainfall was extended back to the 1960s using long-

term observational rainfall data. Sliding correlations on a 21-year moving window between DMI and rainfall were calculated using all three rainfall datasets. The correlation coefficient has increased since the 1970s, and it has steadily reached above 0.6 since the late 1980s (Fig. 4.10a). Spatial patterns of partial correlation show that the correlations were much weaker during 1967-1990. Significant positive correlations were only observed over the southeastern basin (Figs. 4.10b-c). While for the recent two decades, stronger positive correlations were discovered with extended coverage including the western and southern basin (Figs. 4.10d-e). Changes in spatial correlation maps suggest stronger potential impacts of IOD on rainfall.

Considering the stronger correlation between the DMI and precipitation, possible changes in rainfall and contributions from the IOD were assessed. Figure. 4.11 shows that there are more grids showing increasing rainfall trends since 1991 compared to the earlier period 1967-1990. Next, rainfall trends were estimated at both basin and grid levels. Regional averaged rainfall has increased by 0.01-0.02 $mm \cdot d^{-1} \cdot yr^{-1}$ ($P < 0.05$) since 1991 featured with an increasing DMI (Fig. 4.11b). Spatial patterns of rainfall trends show that the wetting is strong over northern, central, and southeastern CEA, though CHIRPS2 data observed weaker increasing trends. The maximum increasing rate reaches above 0.04 $mm \cdot d^{-1} \cdot yr^{-1}$ (Figs. 4.11c-e). To quantify the sensitivity of rainfall to IOD, we adopted the method following Cai et al. (2009): first, detrended rainfall anomalies were regressed onto the detrended DMI to quantify IOD impacts on rainfall. Then, the regression coefficients were multiplied with the DMI trend to yield rainfall changes congruent with the increasing DMI. The results suggest that impact of IOD is strong over western, southern, and eastern CEA, which are consistent with previous partial correlation results. The IOD trend-congruent rainfall increase is comparable with the observed rainfall increases in the western,

southern, and eastern basin, while the IOD-congruent rainfall decrease over the northwestern CEA was observed by GPCC and CHIRPS2 data (Figs. 4.11f-h).

4.4 Conclusions and Discussions

Using observational rainfall datasets, we have shown a robust positive correlation between SOND precipitation over CEA and IOD during 1981-2019, which was little addressed in previous studies. The correlated coefficient between DMI and regional averaged rainfall reaches 0.65 ($P < 0.01$). Rainfall amount, frequency, and the frequency of extreme rainfall events significantly increased during positive IOD events and decreased during negative IOD events. Consistent with the seasonal phase locking of IOD, the enhancement in rainfall amount and frequency peaks during October and the suppression of precipitation is stronger during November. In general, the enhancement associated with positive IOD events is stronger than the suppression associated with negative IOD events, which might be attributed to the generally greater amplitude of positive IOD events (Cai et al. 2013).

Changes in rainfall activity associated with the IOD are likely via modifications of mean circulations, moisture distribution, and MJO activity. Composite analysis indicates that increased rainfall during positive IOD events is featured with a weaker Walker Circulation, which is consistent with previous studies manifesting contributions of a strengthened Walker Circulation to the drying trend in CEA (Hua et al. 2016; Hua et al. 2018). Following the change in the Walker Circulation, moisture increases in the lower and middle troposphere over CEA. MJO activity covaries with the IOD to influence CEA rainfall as well, which was less addressed when quantifying oceanic influences on rainfall or interactions between the MJO and the IOD. There are likely more wet MJO days during positive IOD events and more dry MJO days during negative

IOD events, which are consistent with previous studies indicating higher SST favoring the development of certain MJO convection (Kug et al. 2009; Wilson et al. 2013). Anomalies in the Walker Circulation and moisture distribution are amplified by MJO activity. Enhancement of convection over CEA is stronger within wet MJO days during positive IOD events. During negative IOD events, the easterly jet over CEA is weakened, while slightly more moisture is transported to the basin during dry MJO days. As a result, the net MJO impacts are more likely to increase precipitation during active IOD events, particularly for positive IOD events. Interannual variability of the IOD would thus provide useful indications to understand rainfall variability and conduct reliable rainfall prediction in the changing climate over CEA.

Given the important role of IOD-MJO interactions on precipitation, further research on interactions between sub-seasonal variability and interannual variability is required to explicitly understand regional rainfall variability and improve seasonal predictions. Our study found that MJO convection over eastern African and the western Indian Ocean (wet phases) are strengthened during positive IOD events, and MJO convection over the eastern Indian Ocean and Maritime Continent (dry phases) are strengthened and eastward shifted during negative years. However, impacts of MJO on CEA rainfall do not simply depends on MJO frequency and convection cores, but also on how the MJO system affects local weather conditions including wind shears and moisture. In addition, there are interactions among IOD and other climatic modes via the atmospheric bridge (Alexander et al. 2002). IOD is positively correlated with ENSO ($R = 0.75$, $P < 0.01$) during September-December. Though an El Niño event is associated with decreased CEA rainfall, it could be concurrent with a positive IOD event to enhance local rainfall. On the other hand, ENSO affects MJO activity as well. Time lagged correlation analysis indicated that MJO is particularly strong in the Pacific Ocean when an El Niño event develops but is weak in the wake

of the El Niño (Zhang and Gottschalck 2002). MJO convection also tends to shift eastward during El Niño events, and vice versa (Hendon et al. 1999; Bergman et al. 2001). However, specific studies including ENSO-MJO interactions tested few associations with African rainfall. Hence, process-based climate model simulations are further needed to obtain a more nuanced understanding of IOD and ENSO's interactions with sub-seasonal variability and their combined influences on CEA precipitation.

Consistent with previous climate projections, the DMI has increased since the 1960s. Along with the warming Indian Ocean, the positive correlation between DMI and SOND rainfall becomes stronger with time, and an increasing trend in SOND rainfall has been observed since the 1990s as well. The IOD trend-induced rainfall increase are suggested to account for much of the rainfall trend by regression analysis. Aside from increases in DMI and the correlation between IOD and CEA rainfall, the frequency of strong positive IOD events is projected to increase (Cai et al. 2014; Cai et al. 2020). The Walker Circulation is predicted to decrease and MJO activity will be modified under the warming climate (Vecchi and Soden 2007; Maloney et al. 2019). It is possible that variations in CEA rainfall and the correlation between IOD and CEA rainfall are linked with the global warming trend. Although we did not answer how much change in rainfall can be explained by internal variability or anthropogenic warming, our results highlight the necessity and importance of the increasing influences of the IOD-CEA rainfall relationships into future climate projection and seasonal forecasts of CEA rainfall.

Tables and Figures

Table 4.1 Oceanic indices used in this study.

Index	Time period	Definition	Source SST Dataset
ONI (Oceanic Niño Index)	1950-2020	3-month running mean of SST anomalies in the Nino 3.4 region (5°N-5°S, 120°W-170°W)	NOAA ERSST v5
DMI (Dipole Mode Index)	1870-2020	Monthly SST anomaly difference between the western equatorial Indian Ocean (10°N-10°S, 50°E-70°E) and southeastern equatorial Indian Ocean (0°-10°S, 90°E-110°E) (climatology is 1981-2010)	HadISST 1.1
TNA (Tropical Northern Atlantic Index)	1948-present	Monthly SST anomaly from 5.5°N-23.5°N, 15°W-57.5°W (climatology is 1971-2000)	HadISST and NOAA OI 1°x1° datasets
SNA (Tropical Southern Atlantic Index)	1948-present	Monthly SST anomaly from 0°-20°S, 30°W-10°E (climatology is 1971-2000)	HadISST and NOAA OI 1°x1° datasets

Table 4.2 Partial correlation coefficients between the CHIRPS2 rainfall data and different ocean sea surface temperature (SST) indices for the period 1981-2019.

Time / Ocean index	DMI	ONI	TNA	TSA
MAM	0.11	0.02	-0.29*	-0.05
JJA	0.38**	-0.65***	0.18	0.15
SON	0.68***	-0.44***	0.25	0.06
DJF	0.30*	-0.19	0.09	0.10

Note: "*" indicates that the correlation is significant at 90% confidence level. "**" indicates that the correlation is significant at 95% confidence level. And "***" indicates that the correlation is significant at 99% confidence level. MAM–March-April-May. JJA–June-July-August. SON–September-October-November. DJF–December-January-February. "DMI", "ONI", "TNA" and "TSA" are defined in section 4.2.2.

Table 4.3 Percentage time (%) of MJO activities during different IOD events during 1981-2019.

IOD phases	Inactive MJO	Other active MJO	Wet MJO (1/2)	Dry MJO (4/5/6)
Neutral	40.5%	20.4%	13.2%	25.9%
Positive	36.6%	19.0%	19.3%	25.1%
Negative	44.4%	18.0%	10.9%	26.7%

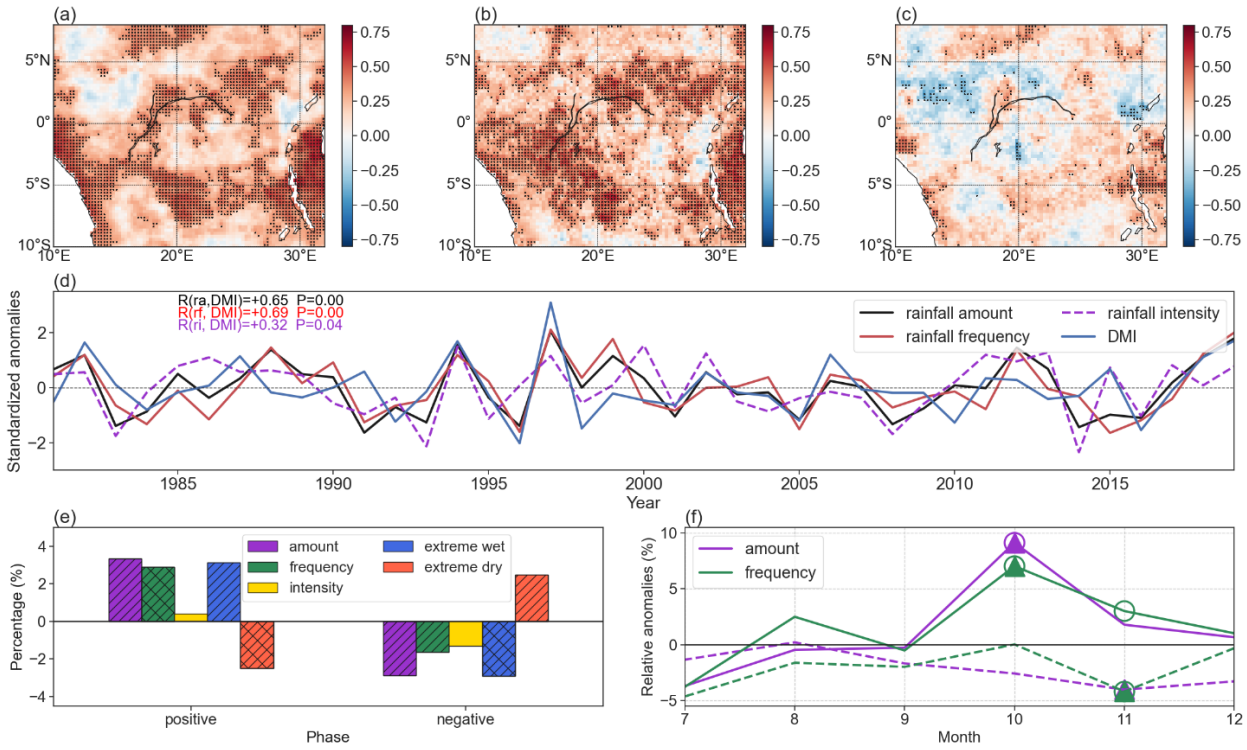

Figure 4.1 Correlations between CEA rainfall and the DMI during September-December for the period 1981-2019. Spatial patterns of partial correlations between the DMI and (a) rainfall amount, (b) rainfall frequency, and (c) rainfall intensity. Grid boxes with dots indicate statistical significance at the 95% confidence level. (d) Interannual variations in the DMI, rainfall amount, frequency, and intensity. The partial correlation coefficients between the DMI and rainfall characteristics and significance levels are shown as well. (e) Relative anomalies of rainfall amount, frequency, intensity, and frequency of extreme rainfall events during positive and negative IOD events. Color bars marked with hatched lines indicate significant at the 95% confidence level tested by Monte Carlo simulation. Color bars with cross lines indicate the significance verified by both Monte Carlo simulation and the two-tailed Student t test. (f) Relative anomalies of monthly rainfall amount and frequency during positive IOD (solid lines) and negative events (dashed lines). Points marked by circles indicate significance at the 95% confidence level tested by Monte Carlo simulation. Points marked by triangles indicate significance at the 95% confidence level tested by Student t test.

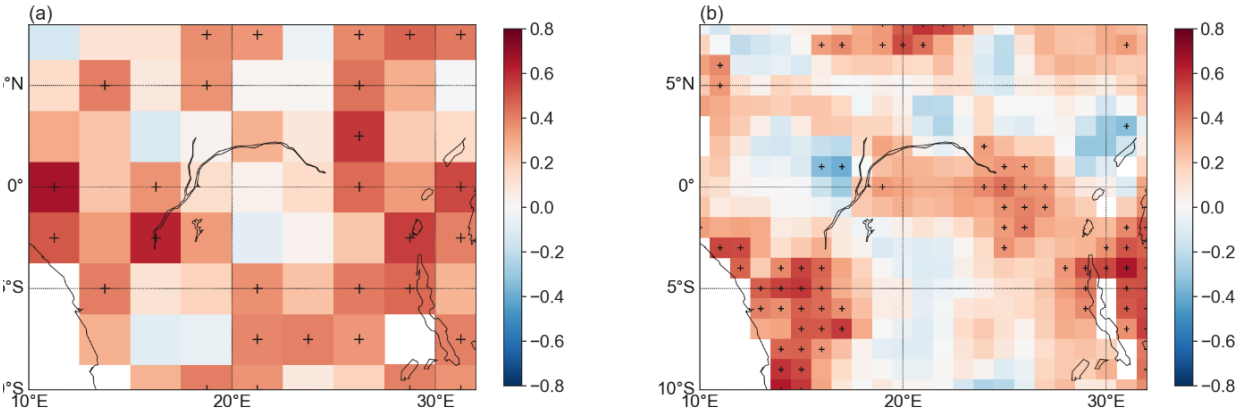

Figure 4.2. Spatial patterns of partial correlations between the DMI and rainfall amount during September-December estimated by (a) NIC131 (1981-2014) and (b) GPCC (1981-2016). Grid boxes with crosses indicate statistical significance at the 95% confidence level.

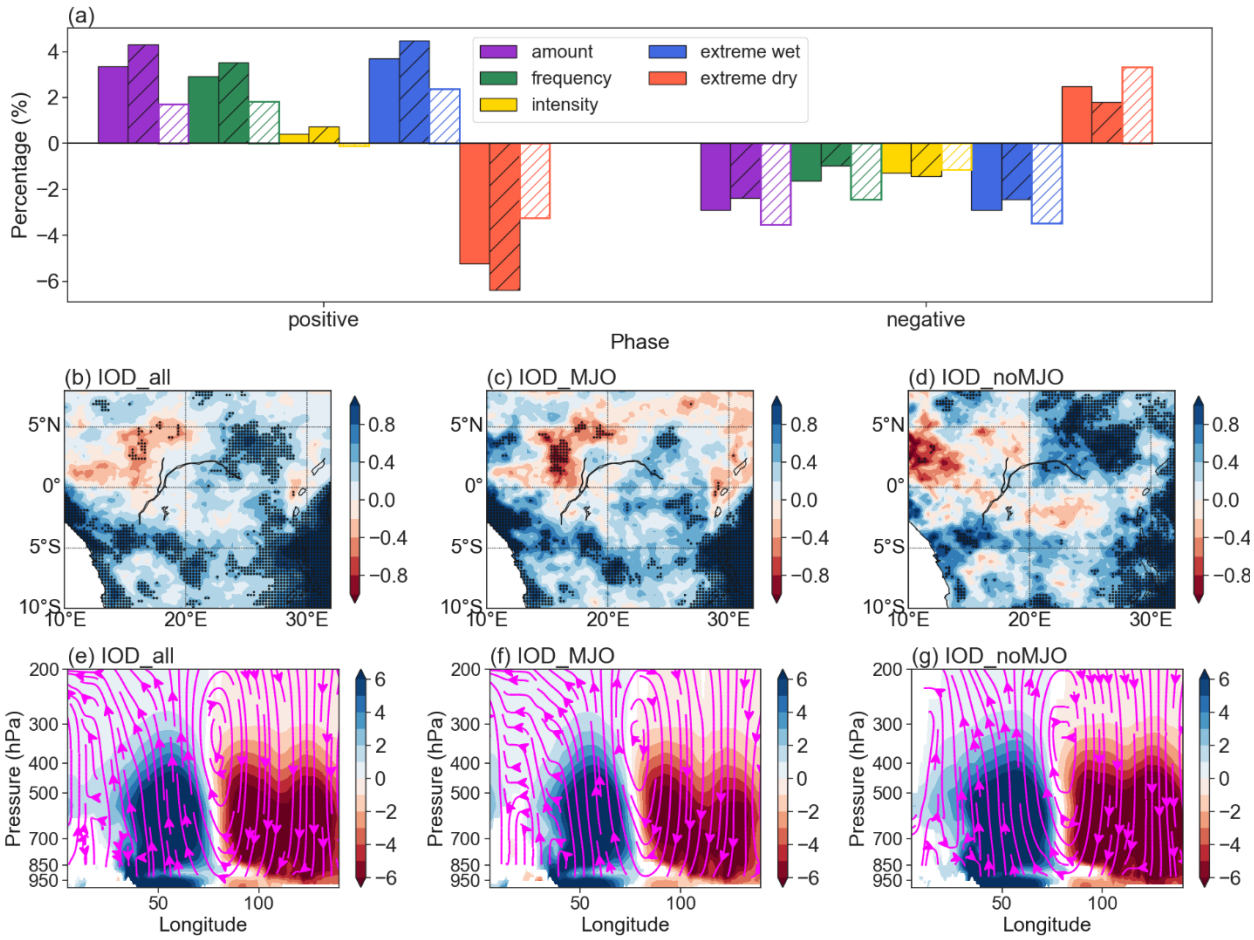

Figure 4.3 Modified impacts of IOD on CEA rainfall by MJO during SOND. (a) Relative anomalies of rainfall amount, frequency, intensity, and frequency of extreme rainfall events during positive and negative IOD events. Solid color bars with hatched lines present rainfall anomalies with MJO influences. Color bars with only hatched lines present rainfall anomalies without MJO impacts. Spatial patterns of differences in rainfall amount between (b) positive and negative IOD events, (c) positive and negative IOD events with active MJO, (d) same as (c) but without MJO activities. Grid boxes with dots indicate statistical significance at the 95% confidence level. Composites of differences in meridional mean (10°N-10°S) specific humidity (10^{-1} g·kg^{-1}, shaded), streamlines of zonal wind (m/s) and omega (10^{-1} Pa·s^{-1}) between (e) positive and negative IOD events, (f) positive and negative IOD events with active MJO, (g) same as (f) but without active MJO. Only significant differences at 95% confidence level are plotted.

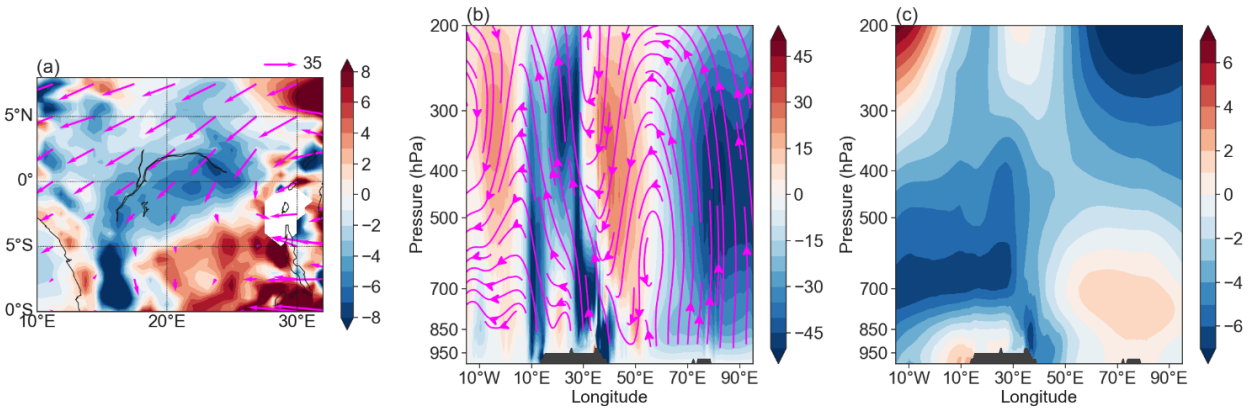

Figure 4.4 Climatology of (a) moisture divergence (10^{-8} kg·kg^{-1}·s^{-1}, convergence is shaded in blue) and flux (g·kg^{-1}·m·s^{-1}, vectors) at 850hPa, and vertical cross section (averaged over 10°N-10°S) of (b) omega (10^{-3} Pa·s^{-1}, shaded) and streamlines of zonal wind (u, m/s) and omega (10^{-1} Pa·s^{-1}) and (c) zonal wind (m/s) during September-December for the period 1981-2019.

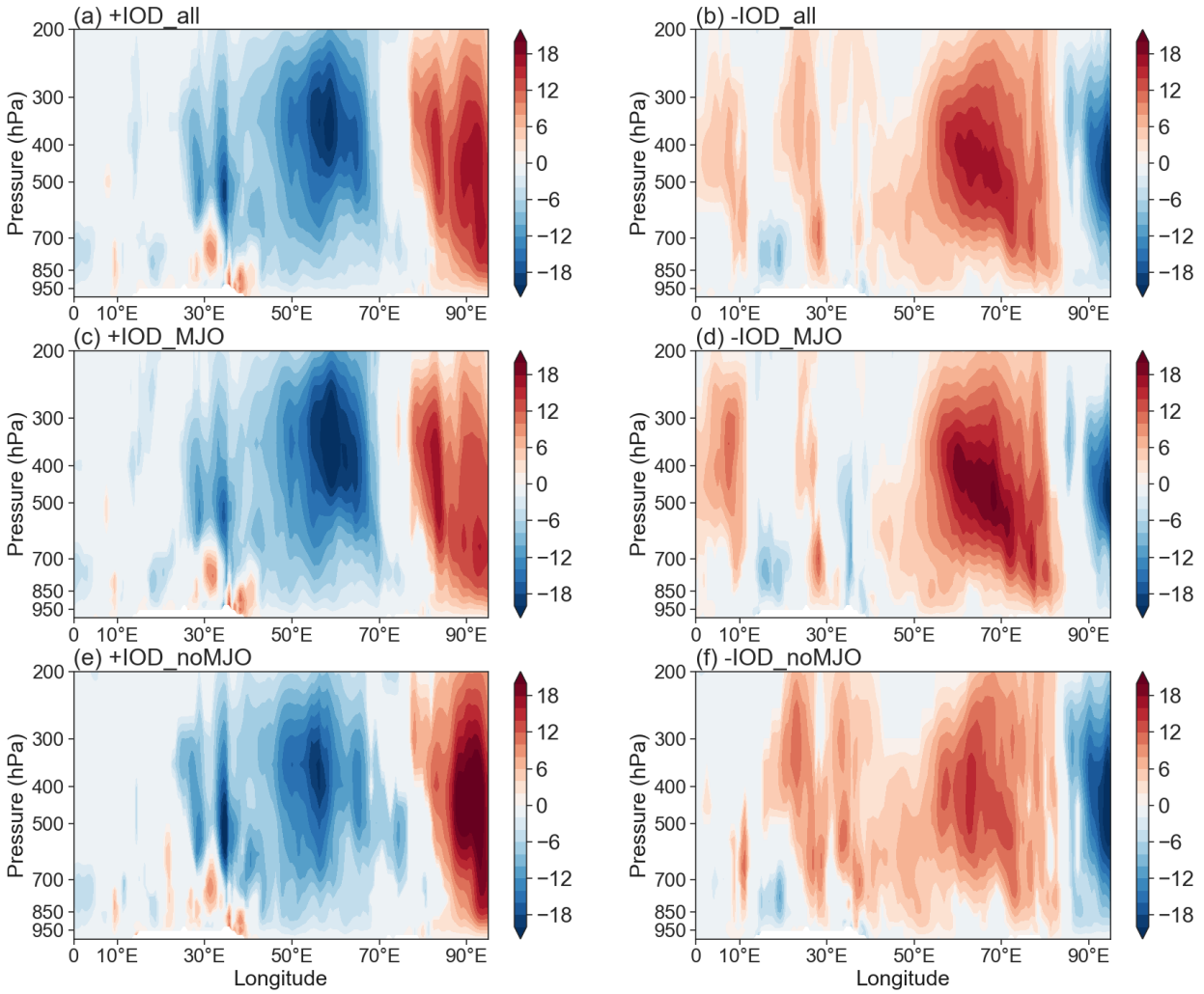

Figure 4.5 Composite of meridional mean (10°N-10°S) omega anomalies (10^{-3} Pa·s^{-1}) during (a) all positive IOD days, (c) positive IOD days with active MJO activities, and (e) exclusively positive IOD days during 1981-2019. (b) Same as (a), but for all negative IOD days. (d) Same as (c), but for negative IOD days with active MJO activities. (f) Same as (e), but for negative IOD days. Only significant anomalies at the 95% confidence level are plotted.

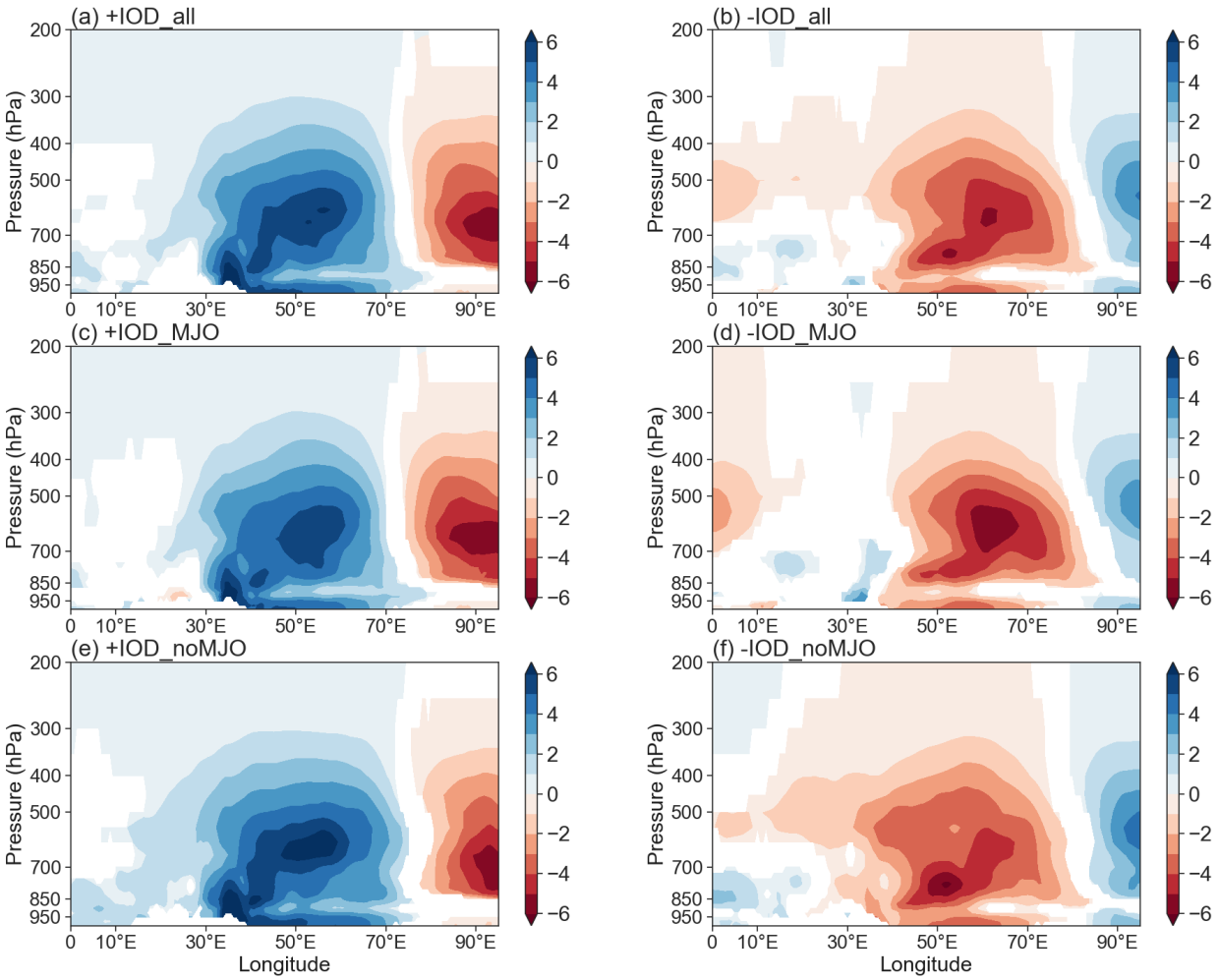

Figure 4.6 Same as Figure 4.5 but for specific humidity anomalies (10^{-1} g·kg^{-1}).

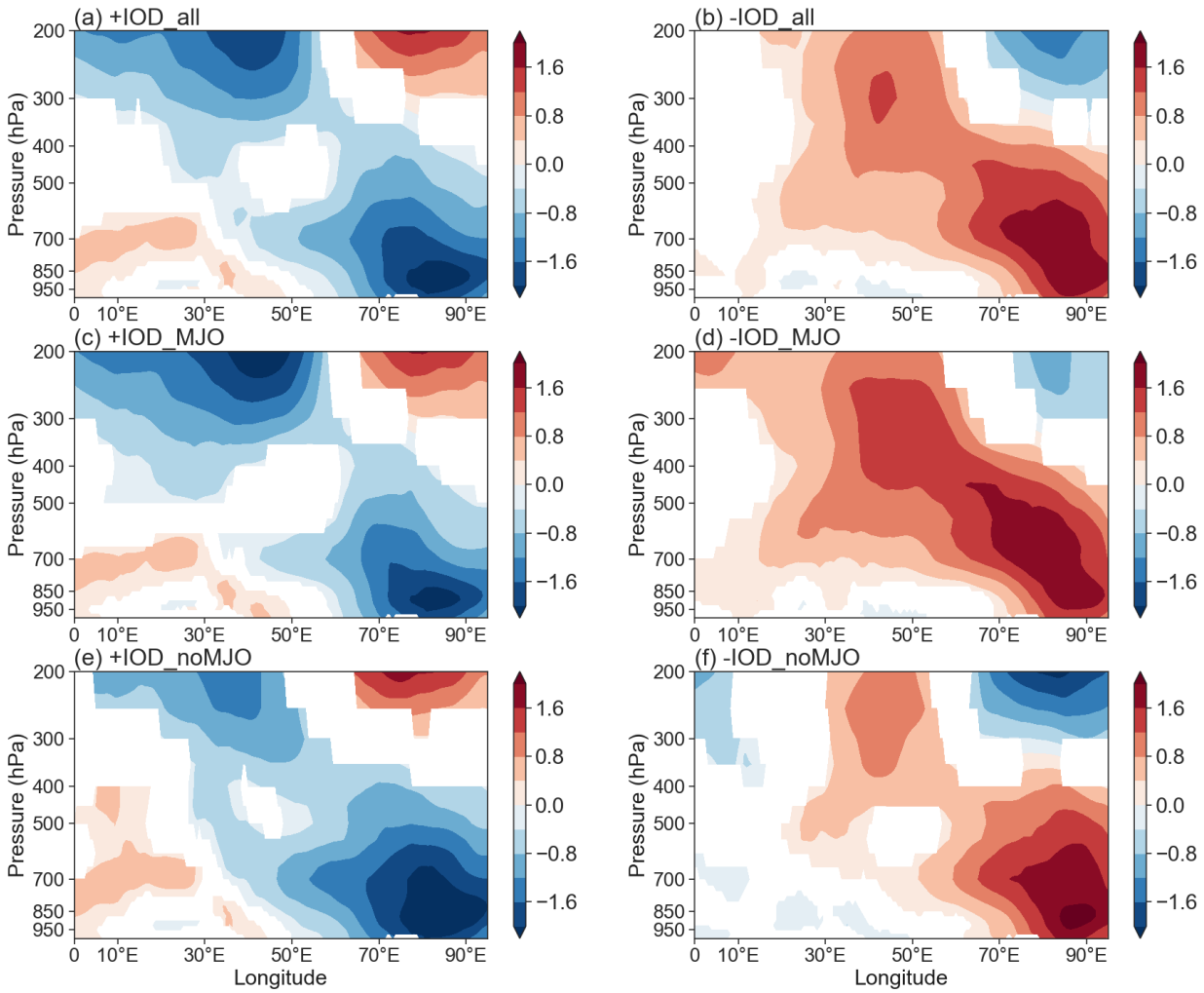

Figure 4.7 Same as Figure 4.5 but for zonal wind anomalies ($m \cdot s^{-1}$).

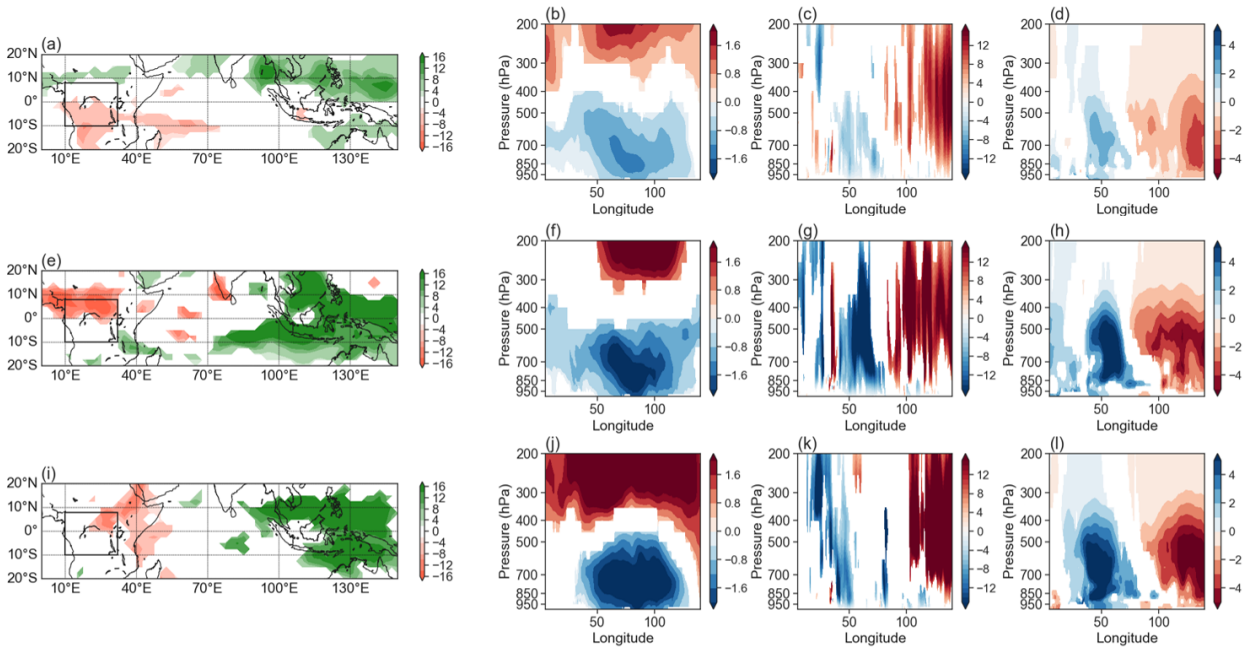

Figure 4.8 Anomaly composites of (a) OLR anomalies ($W \cdot m^{-2}$), (b) meridional mean zonal wind (m/s), (c) vertical motion ($Pa \cdot s^{-1}$), and (d) specific humidity ($g \cdot kg^{-1}$) for wet MJO phases during neutral IOD events. (e-h) Same as (a-d) but during positive IOD events. (i-l) Same as (a-d) but during negative IOD events. Only significant anomalies at the 95% significance level are plotted.

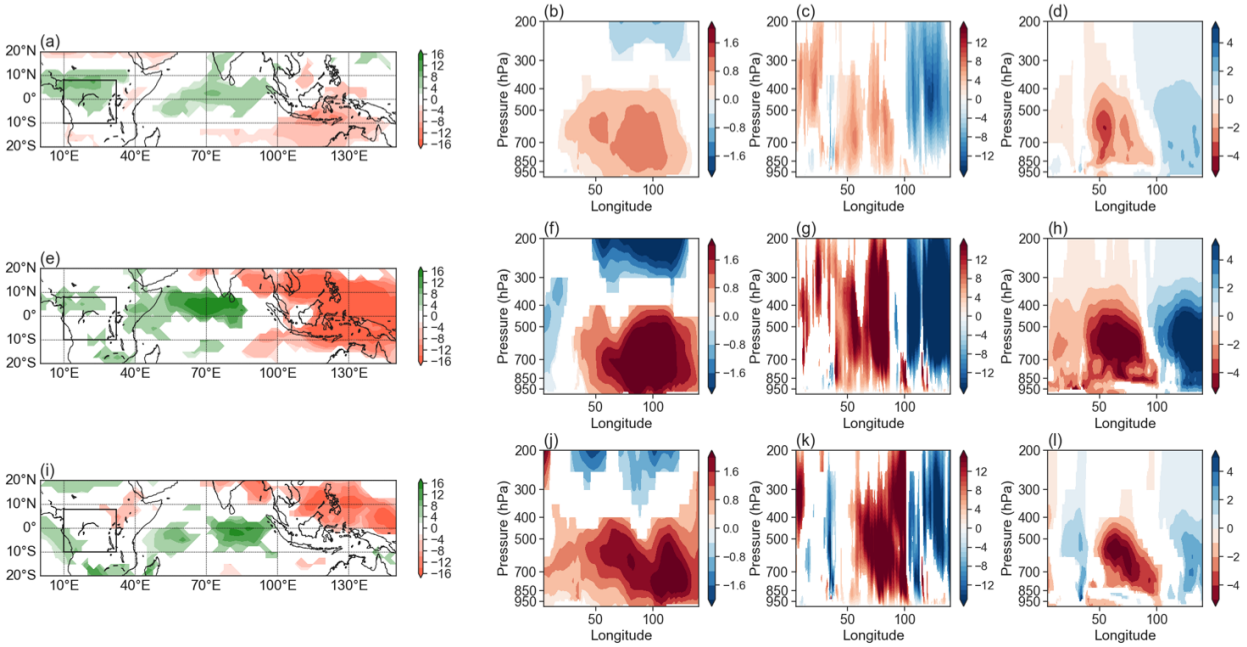

Figure 4.9. Same as Figure 4.8 but for dry MJO phases.

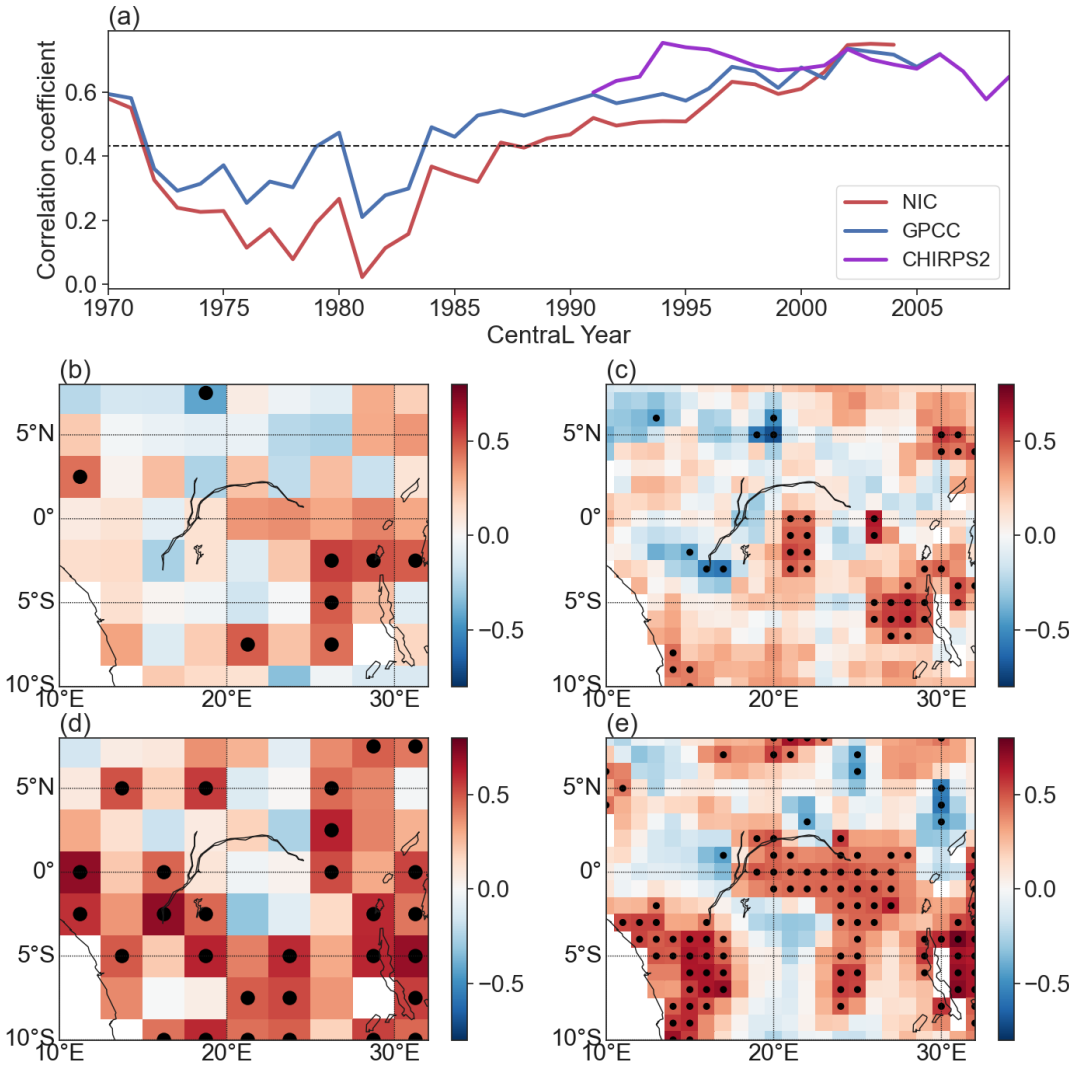

Figure 4.10 (a) 21-year sliding partial correlations between the DMI and SOND rainfall amount for the period 1960-2019. The black dashed line indicates significance at 95% confidence level. Spatial patterns of partial correlations between the DMI and rainfall estimated by (b) NIC131 and (c) GPCC during 1967-1990. (d-e) Same as (b-c) but during 1991-2014. Grid boxes with dots indicate correlations are significant at the 95% confidence level.

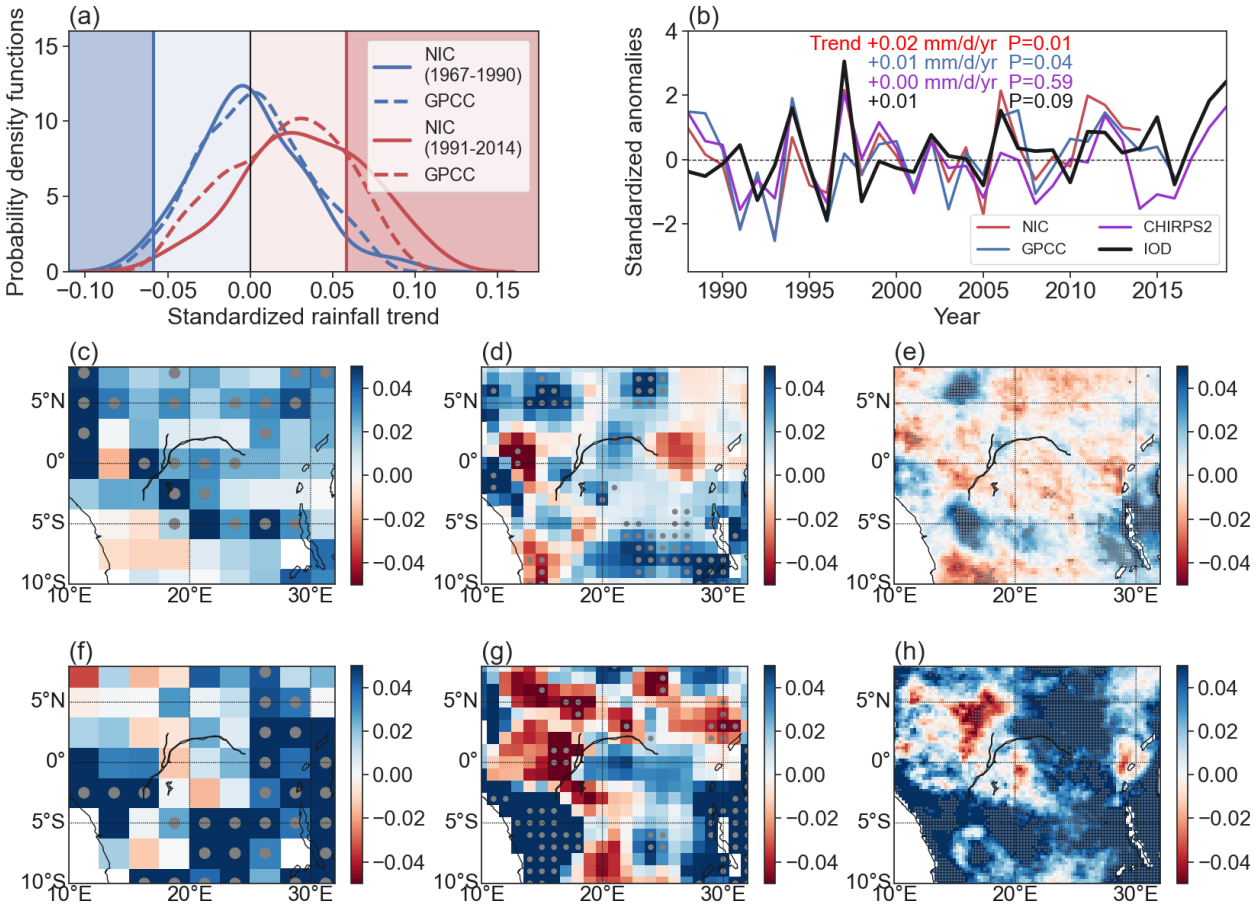

Figure 4.11 (a) Probability density functions of standardized rainfall trends estimated by NIC131 (solid lines) and GPCC (dashed lines) within CEA during 1967-1990 (blue lines) and 1991-2014 (red lines). Dark red and blue shades indicate grids with significant trends at the 95% confidence level. (b) Interannual variations and linear trends of the DMI and rainfall since 1991. Linear trends and significance levels are shown. Spatial pattern of linear trends in rainfall ($mm \cdot d^{-1} \cdot yr^{-1}$) estimated by (c) NIC131, (d) GPCC, and (e) CHIRPS2 during 1991-2014. Grid boxes with dots have a significant trend at 95% confidence level. Interannual rainfall changes ($mm \cdot d^{-1} \cdot yr^{-1}$) congruent with the DMI trend estimated by (f) NIC131, (g) GPCC, and (h) CHIRPS2 during 1991-2014. Grid boxes with dots indicate the regression are significant at 95% confidence level.

Chapter 5 Impacts of Evapotranspiration on Precipitation in the Congo Basin

5.1 Introduction

Tropical rainforests play a major role in water and carbon cycles (Lewis 2006; Hagos and Leung 2011). The role of rainforests in the water cycle is to add moisture to the atmosphere through evapotranspiration (ET) from two distinct mechanisms: transpiration (in which plants release water from their leaves during photosynthesis) and evaporation (in which plants evaporate from water to the air from aerial parts, such as leaves, stems, flowers, and soils) (Wang and Dickinson 2012). By controlling the fluxes of water, heat, and momentum exchanges between the land surface and the atmosphere, rainforests affect cloud formation, atmospheric circulation processes, and precipitation (Worden et al. 2007; Jasechko et al. 2013; Sheil 2018). Disturbances due to climate change and deforestation might exert profound impacts on vegetation functions, which would influence atmospheric conditions to accelerate or decelerate climate change in turn (IPCC 2002; Malhi and Wright 2004; Syktus and McAlpine 2016). Thus, studying variations in rainforests ET and its influences on climate is not only important to understand rainforest sensitivity to climatic perturbations, but also has important implications for studies on vegetation-climate interactions.

Termed as the 'Green Ocean', the largest amount of ET is observed over tropical rainforests. Most terrestrial precipitation is recycled from land surface and more than half of this derives from plants transpiration (Spracklen et al. 2012; Sheil 2018). In the Amazon, moisture recycling contributes about 25%-33% of precipitation (Eltahir and Bras 1994; Trenberth 1999). A high annual recycling ratio ranging from 28% to 38% has been found in the Congo Basin as well (Pokam et al. 2012; Dyer et al. 2017). ET can be affected by plant's growth stage or level of maturity, the ability of plants to access soil moisture, percentage of soil cover, solar radiation, humidity, temperature, and wind (Peters 2016). Sensitivity of rainforests to climatic or

anthropogenic perturbations is thus complicated. Because of deep roots and ample soil moisture, ET in the Amazon is often maintained or even enhanced during the dry season, when net radiation is high (Hasler and Avissar 2007; Harper et al. 2014; Restrepo-Coupe et al. 2021). However, extreme scenarios like deforestations, the complete removal of trees for the conversion of forest to another land use, result in reduced moisture into the atmosphere, less precipitation, and more droughts as shown in observations and GCM simulations (Zemp et al. 2017; McAlpine et al. 2018; Staal et al. 2018). Climate variability in the Congo Basin is characterized by a long-term drying trend and a lengthening boreal summer dry season since the 1980s. In contrast to the Amazon and Southeast Asian rainforests with high rates of deforestation, the Congolese rainforest has experienced the least amount of deforestation and its photosynthetic activity has decreased gradually (Zhou et al. 2014; Hua et al. 2016; Jiang et al. 2019). Very likely, these gradual changes imply decreased ET and moisture recycling, which might have influenced the severity and persistency of precipitation perturbations.

Rainforests also impacts seasonal and sub-seasonal precipitation (van den Hurk et al. 2003; Gentine et al. 2019). Moisture recycling affects the timing of the wet season onset by destabilizing the lower troposphere via increasing latent heat during the precedent dry season (Fu and Li 2004; Li and Fu 2004). A novel theory—'biotic pump'—suggests that ET is essential to maintain high rainfall in the continental interiors of the Amazon, Congo, and Siberia (Makarieva et al. 2013). It suggests that a lower pressure zone is generated over transpired forests and draws air in from the surroundings, which cannot be explained by global circulation patterns and moisture recycling as rainfall would decline exponentially with distance inland without forests (Makarieva and Gorshkov 2007; Makarieva et al. 2013). Using advanced water isotope measurements, Wright et al. (2017) indicated that the ability of the Amazonia rainforests to maintain ET in the dry season

plays a key role in retaining rainfall and moisture to facilitate the return of the rainy season, when conventional monsoon-like wind patterns are missing.

Aside from applying empirical analyses, physical climate models are powerful tools to quantify vegetation's impacts on climate and answer 'what if' questions. Because the long-term drying trend and the large-scale vegetation browning over the Congo rainforest are expected to reduce the rainforest ET (Zhou et al. 2014; Hua et al. 2016), one key question is whether such changes will reduce the local rainfall amount and modify the rainfall patterns. Deforested simulations and sensitivity experiments via general climate models (GCMs) have been widely conducted. A large-scale reduction in ET and an increase in surface albedo were generally noted over simulated deforestation regions, however, the subsequent changes in precipitation activity lacked consistent conclusion and varied geographically due to coarse resolutions and model deficiencies in simulating complex regional scale vegetation-atmosphere interactions (e.g., Shukla and Mintz 1982; Polcher and Laval 1994; Findell et al. 2006; Devaraju et al. 2015).

Regional climate models (RCMs) have been proved to be particularly valuable to conduct simulations regarding vegetation regulations on regional climate. Their higher resolution allows for a better representation of fine-scale forcing and land surface heterogeneity, which is important to accurately simulate the local and regional climate system (Paeth et al. 2005; Rummukainen 2010; Sylla et al. 2016). Among the currently available RCMs, the International Centre for Theoretical Physics (ICTP) Regional Climate Model (RegCM) has been widely applied to Africa and has been proved to work properly simulating African climate (Wang and Alo 2012; Bell et al. 2015; Sylla et al. 2016; Wang et al. 2016). For Central Africa, experiments with different prescribed vegetation properties have been conducted to indicate that decreased rainforest ET can efficiently lead to changes in precipitation by influencing water vapor in the lower atmosphere and

water recycling activity (Bell et al. 2015). However, how do vegetation impacts on precipitation vary with different seasons and by different ET perturbation extents are unknown.

In this study, sensitivity experiments are conducted using the latest ICTP RegCM4.9.3 model coupled with the National Center for Atmospheric Research (NCAR) Community Land Model (CLM4.5) over CEA. Combined with newly available water isotope measurements, sensitivity experiments with prescribed ET disturbances are conducted to establish: 1) when and where does ET exert significant impact on precipitation? 2) how does precipitation respond to different ET perturbations? A description of the regional climate model and experiment design are given in section 5.2. Section 5.3 presents the model evaluation. Results from satellite observations and model simulations are included in section 5.4.

5.2 Data and Methods

5.2.1 Model Description

The 4th generation ICTP RegCM4.9.3 (Giorgi et al. 2012) is used in the study. RegCM4 has participated in the Coordinated Regional Climate Downscaling Experiment (CORDEX), a World Climate Research Programme (WCRP) framework to evaluate model performance through a set of experiments aiming at producing regional climate simulations. The model has worked properly for multiple domains including Africa, South America, Central America, East Asia, and Europe (Giorgi et al. 2012; Diro et al. 2012; Gao et al. 2012). RegCM4 is a vertical sigma level, grid point-limited model with compressibility and its dynamic core is derived from the hydrostatic version of the U.S National Center for Atmospheric Research/Pennsylvania State University Mesoscale Model 5 (NCAR/PSU MM5) (Grell et al. 1994). The radiation scheme is derived from the Community Climate Model (CCM3) (Kiehl et al. 1996) and includes representation of aerosols

following Solmon et al. (2006) and Zakey et al. (2006). The model applies the non-local boundary layer scheme of Holtslag et al. (1990) and the ocean flux scheme of Zeng et al. (1998). The Emanuel convection scheme is utilized based on its good model performance in Africa (Wang et al. 2016). The physics package in RegCM4 also includes a large-scale cloud and precipitation scheme that accounts for cloud sub-grid variability (Pal et al. 2000).

The RegCM4.9.3 is coupled with the CLM4.5 land surface model (Oleson et al. 2010) to take advantage of the improved parameterizations and new capabilities owning to the model community's development effort. CLM solves the surface hydrological, biogeophysical, and biogeochemical processes using a hierarchical data structure. Each land grid cell can be divided into a different number of landing units including glacier, lake, vegetated land, etc. Each column can be occupied by multiple plant functional types (PFTs) that differ in physiology and structure, and up to 16 PFTs can be considered. Calculations for surface mass and energy fluxes within a vegetated land unit take place at the PFT level, and the area-weighted average of the surface fluxes from different components within each grid cell is passed to the atmospheric model as the lower boundary conditions (Wang et al. 2016). Within the CLM model, the Ball-Berry stomatal conductance model (Collatz et al. 1991) is applied to resolve ET combined with leaf area index (LAI), stem area index (SAI) and leaf stomal resistance coupling with photosynthetic processes. Thus, LAI and SAI information included at the PFT level provide a proxy to edit ET conditions and are accessible for conducting sensitivity experiments.

Input datasets for initial conditions and lateral boundary conditions are obtained from the 6-hourly real-time ERA-Interim data at 1.5°×1.5° spatial resolution (Dee et al. 2011). Sea surface temperatures are forced by the weekly averages optimum interpolation sea surface temperature from the National Ocean and Atmosphere Administration (NOAA) at 1.0°×1.0° (Reynolds et al.

2002) following previous model simulations over Africa (Bell et al. 2015; Sylla et al. 2016; Wang et al. 2016).

5.2.2 Experiment Design

The model domain extends from 24°N to 24°S and from 20°W to 60° to cover equatorial Central Africa, a large part of Sahel, and parts of both the Indian and Atlantic Oceans (Fig 5.1a). A 50 km × 50 km horizontal grid resolution is used for efficiency. The model performance has been assessed to be comparable to simulations resolved at a finer resolution like 25 km (Sylla et al. 2016). The model includes 18 sigma levels in the vertical and the model top extends to 50hPa. Simulated results are interpolated at 12 pressure levels for analysis.

Five experiments are conducted (Table 5.1). For each run within the experiments, the model is conducted over 16 years from January 2003 to December 2018 with daily outputs. The first year of each simulation is discarded as model spin-up and the results from the remaining 15 years are used. As the biogeochemistry model is inactive, LAI and SAI are updated daily by linearly interpolating between monthly values within the CLM4.5 model (Oleson et al. 2010). Monthly LAI values at PFT level are developed from the 1-km MODIS-derived monthly LAI data (Myneni et al. 2002). SAI is calculated from the LAI using the methods of Zeng et al. (2002).

Here we simply change the LAI and SAI values to mimic the long-term drying induced reduction in ET. Ground water plays an important role in regulating the ET over tropical rainforests, particularly during the dry season. Note that the rainforest trees have deep roots, so they can access deep soil moisture and maintain high ET through most of growing seasons (Baker et al. 2008; Harper et al. 2010; Yan et al. 2020). In the CLM4.5 model, the soil column of each grid is discretized into 15 layers up to 35 m, which takes account of ground water's effects. Also, the

changes in LAI and SAI have limited impacts on canopy albedo over the Congo rainforest as vegetation albedo is very sensitive to LAI/SAI over sparsely vegetated surfaces (with SAI+LAI < 1.5) but becomes saturated for LAI/SAI over dense forests (e.g., with SAI+LAI > 2.5) (Zhou et al. 2003). In this way, we can focus on the sensitivity of precipitation to changes in ET induced by LAI/SAI changes.

In the first group simulation (referred as CTL), defaulted values of LAI and SAI values in the CLM model are used without any changes. In the second group simulations (EXP), both LAI and SAI are prescribed at 4 different percentage change levels (-20%, -10%, +10%, and +20%) for all months simultaneously to consider similar vegetation changes throughout the entire season. Precipitation's responses to ET variations can be established by calculating the differences in simulated precipitation from experiments in the control run and experiment runs. Two-tailed Student's t-test, combined with the fast Fourier transform reducing daily and sub-daily noises (Wright et al. 2017), is applied to test whether the differences are significant or not. Changes in spatial patterns and vertical profiles of atmospheric conditions are analyzed as well.

5.2.3 Observational and Reanalysis Datasets

To validate model results, impacts of ET on precipitation are also estimated by satellite and reanalysis datasets. Water vapor is traced by isotopic data from the near-infrared Tropical Emission Spectrometer (TES) in the EOS Aura satellite (Worden et al. 2006). Molecular differences among hydrogen isotopes like H_2O and HDO cause mass fractionation during transitions of different water phases: heavier isotopes (HDO) preferentially condense, whereas lighter isotopes (H_2O) preferentially evaporate (Galewsky et al. 2016). The heavier deuterium content of water can be calculated as the relative ratio δD in parts per thousand (‰):

$$\delta D = 1000 \times \frac{R - R_{std}}{R_{std}} \quad (5.1)$$

where R is the ratio of the number of HDO molecules (N_{HDO}) to the number of H_2O molecules (N_{H_2O}) and R_{std} is the corresponding N_{HDO}/N_{H_2O} ratio in a reference standard and equals to 3.11×10^{-4} (Wright et al. 2017). Under thermodynamic equilibrium conditions, δD for tropical oceanic evaporation is approximately -70 to -80‰, whereas δD terrestrial evaporation is about -20 to -40‰ for less water condenses along the transportation path. If the free tropospheric moisture is dominated by upward mixing of local ET, then the largest specific humidity in the free troposphere will be associated with the highest value of δD (Wright et al. 2017). In this way, the water isotopes provide a direct measurement to attribute moisture from the continent and oceans.

Daily measurement of specific humidity (q) and δD are retrieved from Version 6 of the TES retrieval algorithm (v006_Litev01.00) measuring the volume mixing radios of HDO, water vapor, methane, and nitrous oxide with the 0.5×5 km nadir spatial resolution at 17 pressure levels from September 2004 to December 2015 (Worden et al. 2012). Pressure-weighted q and δD in the free atmosphere (348-750hPa) are calculated following Wright et al.'s (2017) quality control criteria: 1) The cloud effective optical depth must be < 0.4; 2) the degrees-of-freedom for a signal for the entire file must be >1. Datasets of q and δD are further interpolated on to the 1° grid box.

The observational precipitation dataset is obtained from the daily CHIRPS2 at 0.25° resolution (Funk et al. 2015). The ET dataset is obtained from the daily Global Land Evaporation Amsterdam Model Version 3.5a (GLEAM v3.5a) at 0.25° resolution for the period 1980-2020 (Miralles et al. 2011; Martens et al. 2017). This latest GLEAM product has updated the data assimilation scheme, water balance module, and evaporative stress functions to optimize its performance at the global scale and address its merit of extensive use of microwave observations. RZSM is also available from GLEAM. Cloud fractions of different cloud types are examined by using the Edition 4A of

the Clouds and the Earth's Radiation Energy System (CERES) Synoptic Radiation Fluxes and Clouds (SYN1deg) daily product at 1.0°×1.0° spatial resolution from March 2000 to December 2020 (NASA/LARC/SD/ASDC 2017). Specific humidity, horizontal winds, and vertical motion are obtained from the 3-hourly MERRA2 reanalysis (Gelaro et al. 2017) to study ET-related atmospheric conditions.

5.3 Model Evaluation

The RegCM4.9.3-CLIM4.5 performance in reproducing the mean climate over the Congo Basin, particularly precipitation patterns, is assessed. First, the representation of the Congolese rainforest and simulations of ET by the model are checked. The distribution of rainforest is compared with the MODIS land cover product (MCD12C1) based on the IGBP classification scheme (Friedl et al. 2010). The description of rainforests in the CLM4.5 model well matches the MODIS land cover data (Figs. 5.1a-b). The regional mean seasonal cycle of LAI and SAI of rainforest pixels are shown in figure 5.1c. Values of both LAI and SAI reach the peaks in the late MAM rainy season, which are consistent with the peak values of ET in MAM. The simulated ET is compared with the GLEAM ET data (Fig. 5.2). Though the seasonal cycle of simulated ET captures its bimodal pattern, the simulated ET magnitude is lower than the observations, particularly during dry seasons. The spatial pattern of simulated ET further indicates that the lower regional mean ET values are related to lower ET values over the central and eastern basin.

Next, simulated precipitation in CTL is compared with the daily CHIRPS2 dataset (Funk et al. 2015) and the newly available monthly in situ rainfall datasets NIC131 (1901-2014; Nicholson et al. 2018b). The simulated regional mean daily precipitation over the Congo Basin (10°E-31°E, 5°N-8°S) matches the two observational rainfall precipitation datasets well ($R > 0.9$) (Fig. 5.3a).

The bias in the simulated spatial pattern of rainfall is further estimated. The Taylor diagram shows that the pattern correlation of precipitation is about 0.7 and the standard deviation is about 0.9 against the CHIRPS2 dataset (Fig. 5.3b). The simulated spatial pattern of annual total rainfall is also compared with the CHIRPS2 and NIC131 rainfall data. The amount and distribution of precipitation are comparable with observations. However, there is an underestimation in rainfall amount in the central and eastern basin, where ET is underestimated as well (Figs. 5.3c-e). Overall, the RegCM4 model decently simulates precipitation climatology over the Congo Basin. Though biases exist in both precipitation and ET, the general spatial patterns and the seasonal cycle for these two variables are consistent between observed and simulated. Thus, using this model to quantify precipitation responses to ET disturbances is still feasible.

5.4 Results

5.4.1 Observed ET Impacts on Precipitation and Atmospheric Dynamics

To establish ET's impacts on precipitation over the Congo Basin, ET's contribution to atmospheric moisture supporting local precipitation is first analyzed using the satellite-retrieved TES product. Regional averaged ET shows strong synchrony with precipitation. ET and precipitation both reach the peaks during the MAM rainy season and decrease dramatically in the following JJA dry season. Compared to the peak of precipitation in October, ET reaches its peak in April instead. The contribution of ET to atmospheric moisture over the Congo basin, estimated by the regression slope of δD against q, reaches the peak in April as well. A high positive regression slope persists through the JJA dry season, though ET amount is low during this time. The regression slope drops below zero during September-November (SON), which indicates increased contribution of oceanic moisture (Fig. 5.4a).

Large amounts of high clouds (> 300hPa) are observed in both rainy seasons indicating strong convection activity, while an increase in low clouds (below 700hPa) occurs during the middle and late JJA dry season (Fig. 5.4b). Moisture converges in the lower troposphere (~850hPa) during both two rainy seasons. Moisture convergence exists in the middle troposphere (~500hPa) during both MAM and JJA. Humidity increases during the MAM rainy season, drops dramatically during JJA and starts to increase again in the following rainy season (Fig. 5.4c). During March to early September, the lower-level easterly wind from the tropical Indian Ocean to the Congo Basin becomes weak, which indicates less moisture transported from the ocean (Fig. 5.4d). The seasonal shifts in different cloud fractions and moisture fluxes suggest a potential and critical role of ET in moisturizing the lower troposphere and might provide high moist static energy to sustain convection, particularly during MAM and JJA.

Figure 5.5 shows spatial patterns of δD and q in the free troposphere during MAM and JJA. The maximum values of δD appear in the eastern and northeastern basin during both MAM and JJA, while the value of δD is higher during MAM (Figs. 5.5a-b). During MAM, q amount is high over almost the whole basin, except the south. Easterly winds prevail above the basin. During JJA, the lower atmosphere is drier and the maximum q shifts to the northeastern basin and easterly winds only prevail over the eastern basin (Figs. 5.5c-d). Combining the adjustments of moisture distribution and dominant horizontal wind, positive and high regression slope of δD against q is observed over the southern Congo Basin (Figs. 5.5e). Though both δD and q amounts are lower during JJA, positive and high regression slopes are found over the western, central, and southeastern basin, which indicate the lager contribution of rainforest ET to moisture sources over the Congo (Figs. 5.5f).

5.4.2 Simulated Precipitation Sensitivity to ET Perturbations

Following the observational results on contribution of ET to precipitation, precipitation sensitivity to ET changes is established by regional climate simulations. First, to ensure the feasibility of generated ET perturbations with prescribed LAI and SAI values, changes in ET in EXP relative to the CTL run are estimated. Theoretically, decreased (increased) ET is suggested under negative (positive) LAI and SAI perturbations if vegetation is not constrained by environmental factors (e.g., light, temperature, water, humidity, and nutrition). For EXP, simulations show that though LAI and SAI are changed at the same percentage in all months, there are opposite responses in regional mean ET during rainy seasons and dry seasons. During rainy seasons, ET increases (decreases) with enhanced (reduced) LAI and SAI. Whereas during dry seasons, ET decreases (increases) with enhanced (reduced) LAI and SAI, particularly during the JJA dry season (Fig. 5.6). Immediate increases in ET during the dry season after an acute drought with sufficient soil water have been observed in the Amazon (Saleska et al. 2007). In addition to reductions in carbon uptake concurrent with drought, ecosystems often experience lower tree growth rates and higher tree mortality rates for several following years, and further decreased ET levels (Galiano et al. 2011; Saatchi et al. 2013; Anderegg et al. 2015; Kolus et al. 2019). In this way, responses of plants to hydrological disturbances at different stages might lead to heterogeneous changes in ET.

Given the relatively large contribution of ET to moisture sources during MAM and JJA, the precipitation sensitivity to ET changes is mainly analyzed during these two seasons using modeling results. Precipitation changes responding to ET perturbations are first analyzed during the MAM rainy season. The last two weeks of February are also included to maximize ET changes and fully consider transitional seasons. Figure 5.7 shows the spatial patterns of changes in ET and

precipitation. At the large scale, with positive (+20%) (negative; -20%) LAI and SAI changes, increased (decreased) ET is observed almost over the whole Congo Basin in figure. 5.7c (Fig. 5.7b). However, there are some local scale noises in the spatial pattern over part of the central and eastern basin (e.g., Fig. 5.7b). Spatial patterns of changes in precipitation are mostly similar to the ET changes, and precipitation generally decreases (increases) under reduced (enhanced) ET, particularly over the eastern basin (Figs. 5.7e-f).

Given the presence of some noises in spatial patterns of precipitation responses to ET perturbations at the grid level, a framework calculating the collective precipitation sensitivity to ET variation is conducted next. The 15-yr mean sensitivities of precipitation amount, frequency, and intensity to ET changes are calculated as the relative changes normalized by relative ET changes, i.e., $\frac{\partial A/A}{\partial E/E}$, $\frac{\partial F/F}{\partial E/E}$, $\frac{\partial I/I}{\partial E/E}$ (Guan et al. 2018) for each rainforest grid. The results indicate that the way that precipitation responds to ET variables fits in a linear model with a regression slope equal to 0.68 ($P < 0.01$) (Fig. 5.8a). This indicates that increased ET would result in increased precipitation, vice versa. Relative changes in rainfall amount can be further decomposed into relative changes in rainfall frequency and intensity (i.e., $\frac{\partial A}{A} = \frac{\partial F}{F} + \frac{\partial I}{I}$). The relative changes in rainfall amount responding to ET variations are mainly attributed to relative changes in rainfall intensity as the regression slope of $\frac{\partial I}{I}$ against $\frac{\partial E}{E}$ equals to 0.78 ($P < 0.01$) (Figs. 5.8b-c).

The spatial pattern of precipitation sensitivity to ET changes is shown in figure 5.9. Precipitation responds positively to ET perturbations over the Congo basin, particularly in the central and eastern basin. The spatial pattern of rainfall intensity sensitivity to ET changes is similar to and consistent with that of rainfall amount (Figs. 5.9a-b). Considering the acute geographic gradient in the distribution of land cover types and the large spread in annual rainfall values (700--2000 mm/yr) in the Congo Basin (Guan et al., 2015), the rainfall sensitivity is

aggregated for different climate zones simply classified by the annual rainfall amount. The results show that grids with annual rainfall less than 1000 mm would become more sensitive to ET perturbations compared to moister grids (Fig. 5.9c).

Same analyses are conducted for rainfall changes during the JJA dry season. Similarly, the first two weeks of September are included. Compared to MAM, enhanced (reduced) ET is aligned with decreased (increased) LAI and SAI values. Though ET varies differently in the dry season relative to the wet season, precipitation activity still responds similarly to ET perturbations, as positive ET perturbations results in increased precipitation, particularly over the northern and northwestern basin (Fig. 5.10). Small rainfall changes in the southern basin are reasonable because both ET and precipitation are much lower during the dry season over these regions. Overall, regression slope of rainfall sensitivity to ET changes is smaller for the whole basin. Considering the acute gradient of rainfall amount from north to south, the rainfall sensitivity is calculated at the grid level. The spatial patterns show similar positive and linear responses of precipitation amount and intensity to ET changes in the northern, central, and eastern basin (Figs. 5.11a-b). Similarly, grids with annual rainfall less than 1000 mm are more sensitive to ET disturbances than those grids with more rainfall (Fig. 5.11c).

5.4.3 Possible Mechanisms in Explaining Precipitation Variations

To identify possible mechanisms regarding the simulated ET's impact on precipitation, horizontal and vertical motions, moisture distribution and convergence, and clouds are compared between EXP and CTL for the two seasons. Results indicate that ET would strongly affect moisture distribution in the lower troposphere to influence precipitation activity. During MAM, there is a significant increase in q from the land surface up to the lower troposphere (~800hPa) right above

the Congo Basin as ET enhances (Fig. 5.12a). The spatial pattern of differences in q at 850hPa further indicate that moisture increases significantly over the basin (Figs. 5.12b-c). Increased moisture would increase moist static energy, which can offset the cooling caused by increased ET at the surface and thus facilitate enhanced precipitation. In contrast, with negative LAI and SAI changes, decreased ET results in a significant decrease of q in the lower troposphere. The spatial patterns shows that this decrease is particularly strong over the central and eastern basin (Figs. 5.12d-f). Spatial patterns in q under ET changes match the spatial patterns of precipitation sensitivity to ET changes as well. During JJA, similar changes in q within the lower troposphere are also observed (Fig. 5.13). As ET decreases under positive LAI and SAI changes, significant decreases in q at 850hPa is observed over the western basin (Figs. 5.13b-c). And moisture significantly increases over the western and central basin as ET increases (Figs. 5.13b-c).

Regarding the observational distinct characteristics of high and low clouds during these two seasons, changes in modeled cloud fractions are analyzed next. During MAM, high cloud fraction increases (decreases) significantly with enhanced (reduced) ET over the basin, particularly over the central, southern, and eastern basin (Fig. 5.14). Increased high cloud fraction implies enhanced convection activity and thus increased precipitation. During JJA, there is less significant change in high cloud fraction. Mild changes in low cloud, referring to shallow convection, are only observed in the northwestern basin. Enhanced (reduced) ET would induce increase (decrease) low cloud fraction (not shown).

Possible changes in atmospheric circulations caused by ET changes are also assessed. Nevertheless, no significant changes in both horizontal and vertical motions emerge in the simulations for both seasons. For vertical motions, in general, a strong ascent dominates over the Congo Basin, and it is stronger during MAM than in JJA. Westerly wind prevails at the surface

level and easterly wind dominate the lower and middle troposphere above the basin (Jiang et al. 2021). Limited ET impacts on atmospheric circulations within the regional model might be caused by dampened regional circulations responses due to fixed atmospheric boundary conditions (Fu 2003; Li et al. 2018). To better estimate impacts of ET on atmospheric circulations, increasing model resolutions to enable descriptions of mesoscale circulations or allowing energy and mass exchanges at the boundary can be considered for future modeling work.

5.5 Conclusions and Discussion

In this study, impacts of ET on precipitation over the Congo Basin are quantified by combining satellite measurements and regional climate model simulations. The daily TES measurements from 2004 to 2015 of water isotopes indicate that ET is a crucial moisture source for precipitation, particularly during the MAM rainy season and JJA dry season. The results are consistent with previous research indicating relatively higher recycling ratio during MAM (25.5%) and JJA (38.9%) compared to other seasons over the Congo Basin (Dyer et al. 2017). In the MAM rainy season, ET moisturizes the middle and lower troposphere and sustain moisture convergence above the basin, when land-sea winds are relatively weak. The results thus support the 'biotic pump' hypothesis (Makarieva et al. 2013). During JJA, ET is essential to sustain moisture in the lower troposphere and shallow convection. The similar shallow convection during the dry season has been found over the southern Amazon as well (Wright et al. 2017). Spatial patterns of the water isotope and specific humidity indicate that ET-related moisture is mainly from the central and eastern basin. ET's contribution to atmospheric moisture is particularly large over the southern basin during MAM. It's contribution almost dominates the whole basin during JJA, particularly in the western, central, and southern basin.

The latest RegCM4.9.3 model performs well in simulating the central African precipitation. With prescribed LAI and SAI values, the precipitation sensitivity to ET changes is established for the period 2004-2018. Simulations indicate that precipitation increases (decreases) under positive (negative) ET changes. Precipitation responds almost linearly to ET perturbations. During MAM, precipitation sensitivity to ET changes is strong over the basin, particularly over the central and eastern basin. During JJA, precipitation sensitivity is strong over the western and northern basin. During both seasons, strong precipitation sensitivity to ET changes is mainly attributed to high sensitivity of precipitation intensity to ET changes. When annual total rainfall amount is below 1000 mm, precipitation would become more sensitive to ET changes.

In model simulations, ET decreases (increases) with negative LAI and SAI forcing during rainy seasons (dry seasons). The total ET over vegetated surface consists of transpiration, interception, and evaporation from bare ground. Transpiration is regulated by canopy stomatal conductance and is controlled by LAI dynamics. Interception is the portion of precipitation that wets the foliage and bark of trees and evaporates rather than reaches the forest floor, and its quantity depends proportionally on the duration, intensity, and direction of precipitation event and on the surface area of foliage and bark, i.e., LAI and SAI. Evaporation term is usually small over dense forests. It refers to the amount of water lost by evaporation from the forest floor and depends inversely on the vegetation amount and cover (or LAI) (Pallardy et al., 1995). Thus, decreases in LAI and SAI might induce considerable increases in evaporation. With the same percentage change of LAI and SAI in all months, ET decreases with negative LAI and SAI forcing during rainy seasons, but it increases during dry seasons. As rainforest photosynthesis and ET are limited by radiation during rainy seasons, the decreases in LAI and SAI may mostly reduce the contribution of interception and thus reduce the overall ET. During the dry season, ET is not

limited by radiation. Enhanced transpiration and evaporation may offset decreases in interception and result in overall increased ET. However, we cannot confirm this due to the lack of related key variables from model output.

Though the RegCM4 model works decently for Central Africa, it has limitations. The model underestimates ET, particularly during the JJA dry season. This might be induced by model limitations in characterizing groundwater and soil properties in the RegCM4, which results in overestimated terrestrial stress constraining vegetation transpiration (Harper et al. 2014). In addition, the relatively simple parameterization of vegetation function depending on LAI and SAI might not accurately describe the partitioning of ET in the model (Zhou et al. 2013). Such model deficiencies in estimating transpiration, interception, and evaporation from bare ground can bias the simulation of ET and thus its impacts on regional precipitation.

By comparing changes in atmospheric conditions, simulations suggest that ET-induced changes in moisture with the lower troposphere is critical to influence precipitation. During MAM, there is increased (decreased) moisture in the lower troposphere with enhanced (reduced) ET over the whole basin. During JJA, moisture distribution changes similarly responding to ET changes, particularly over the western basin. Changes in other variables like vertical motion and horizontal moisture fluxes at the higher level in the troposphere are not identified by the model, which might be affected by fixed atmospheric boundary conditions. Thus, a configuration allowing energy and mass exchanges at the boundary can be applied in future study to better understand ET's impacts on regional atmospheric circulations.

Overall, ET's effect on precipitation is verified by both observations and models. ET activity impacts precipitation activity over the Congo Basin mainly via modifying moisture distribution in the lower atmosphere during MAM and JJA. Precipitation responds positively to ET changes, i.e.,

precipitation would decrease (increase) when ET decreases (increases). As precipitation and vegetation greenness have been decreasing over the Congo Basin during April-June, decreased ET would trigger positive feedback to exacerbate the drying and further slash local rainforest's physical functions. In this way, climate risks and vulnerability of the African rainforests under climate disturbances might have been underestimated.

Tables and Figures

Table 5.1 Model configuration, simulation period and experiment designs.

Experiment	Configuration	Period	Prescribed LAI/SAI*
CON	RegCM4.9.3-CLM4.5	--	--
EXP	RegCM4.9.3-CLM4.5	All months	±20%, ±10%

Note: * 20% and 10% refer to the 20% and 10% increase (+) or decrease (-) in the climatological LAI and SAI values used in the CLM4.5, respectively.

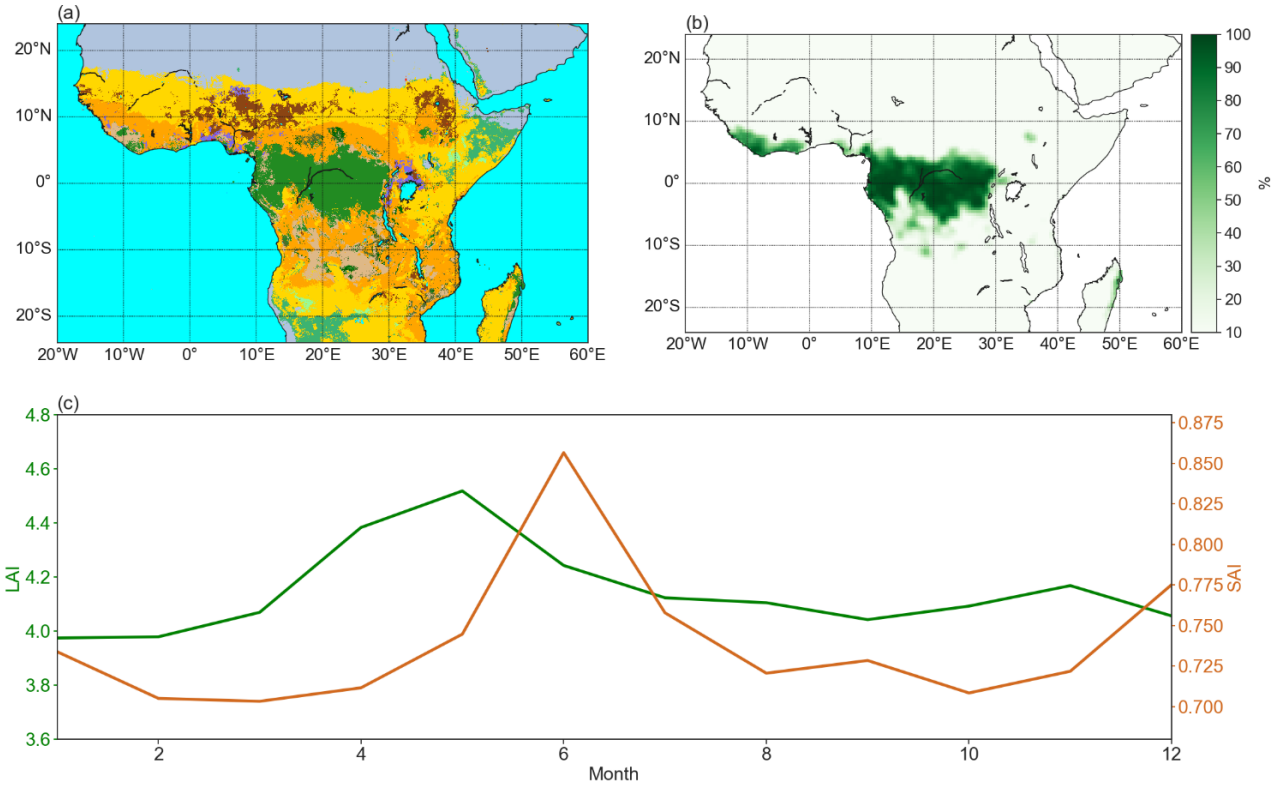

Figure 5.1 (a) The simulation domain and distribution of land cover types in the region. (b) The rainforest fractional cover described by the CLM4.5. (c) The climatological seasonal cycle of leaf area index (LAI) and stem area index (SAI) for all rainforest grids in the CLM4.5 over the Congo Basin (5°N-8°S, 10°E-31°E).

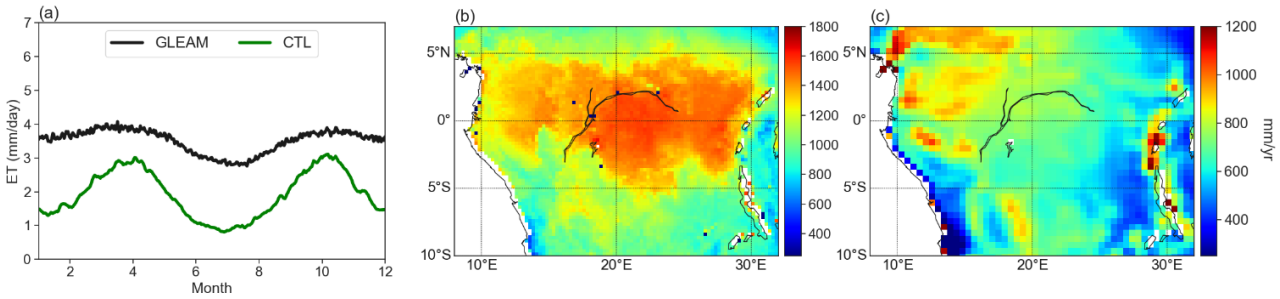

Figure 5.2 (a) Seasonal cycle of regional mean ET from the CTL simulation and the GLEAM product over the Congo Basin for the period 2014-2018. (b) Climatological spatial pattern of annual ET amount from (b) GLEAM and (c) CTL simulation.

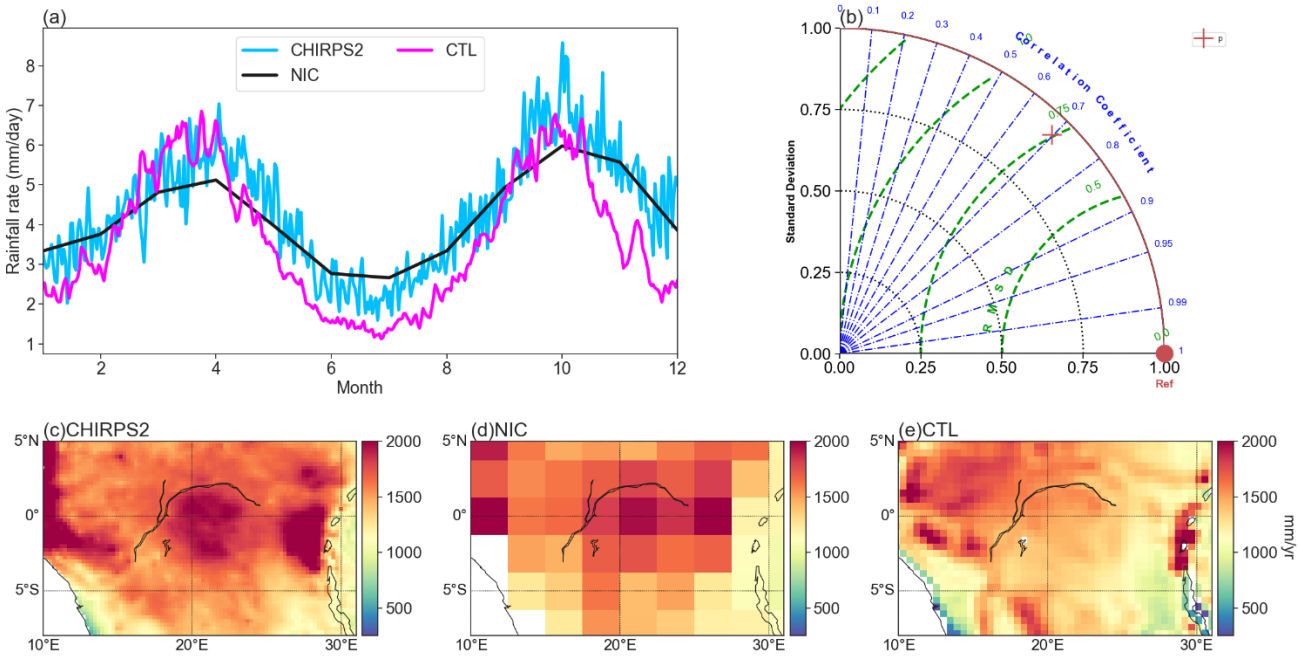

Figure 5.3 Validations of simulated precipitation in the CTL run over the Congo Basin: (a) Seasonal cycle of regional mean precipitation from the CTL simulation and the CHIRPS2 and NIC131 observations during 2004-2018. (b) Taylor diagram for pattern statistics of simulated annual precipitation of CTL against the CHIRPS2 data. Climatological spatial pattern of annual precipitation amount from (c) CHIRPS2, (d) NIC131, and (e) CTL.

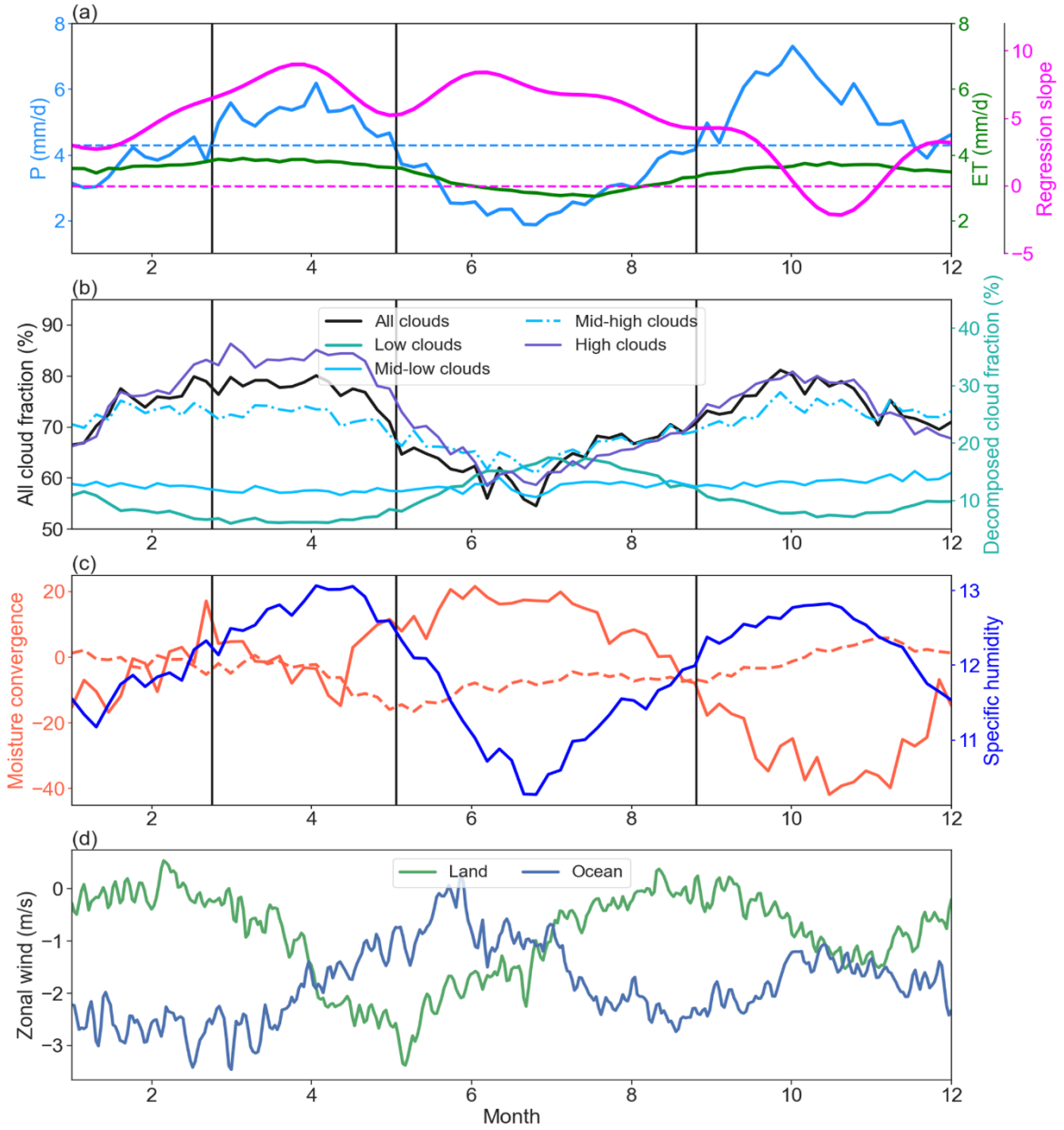

Figure 5.4 Regional averaged daily (a) precipitation (CHIRPS2), ET (GLEAM), 5-d linear regression slope of δD against specific humidity (‰/g·kg^{-1}; TES). (b) Total, low (< 700hPa), mid-low (700-500hPa), mid-high (< 500-300hPa), and high (> 300hPa) cloud covers from the CERES. (c) Moisture divergence (10^{-5} g·kg^{-1}·s^{-1}; negative values refer to convergence) at 850hPa (solid line) and 500hPa (dashed line), and specific humidity (g· kg^{-1}) at 850hPa from the MERRA2 over the Congo Basin (10°E-31°E, 5°N-8°S). (d) Zonal wind at 850hPa over the Congo Basin and the tropical western Indian Ocean (40°E-60°E, 5°N-8°S) from the MERRA2 for the period 2004-2015.

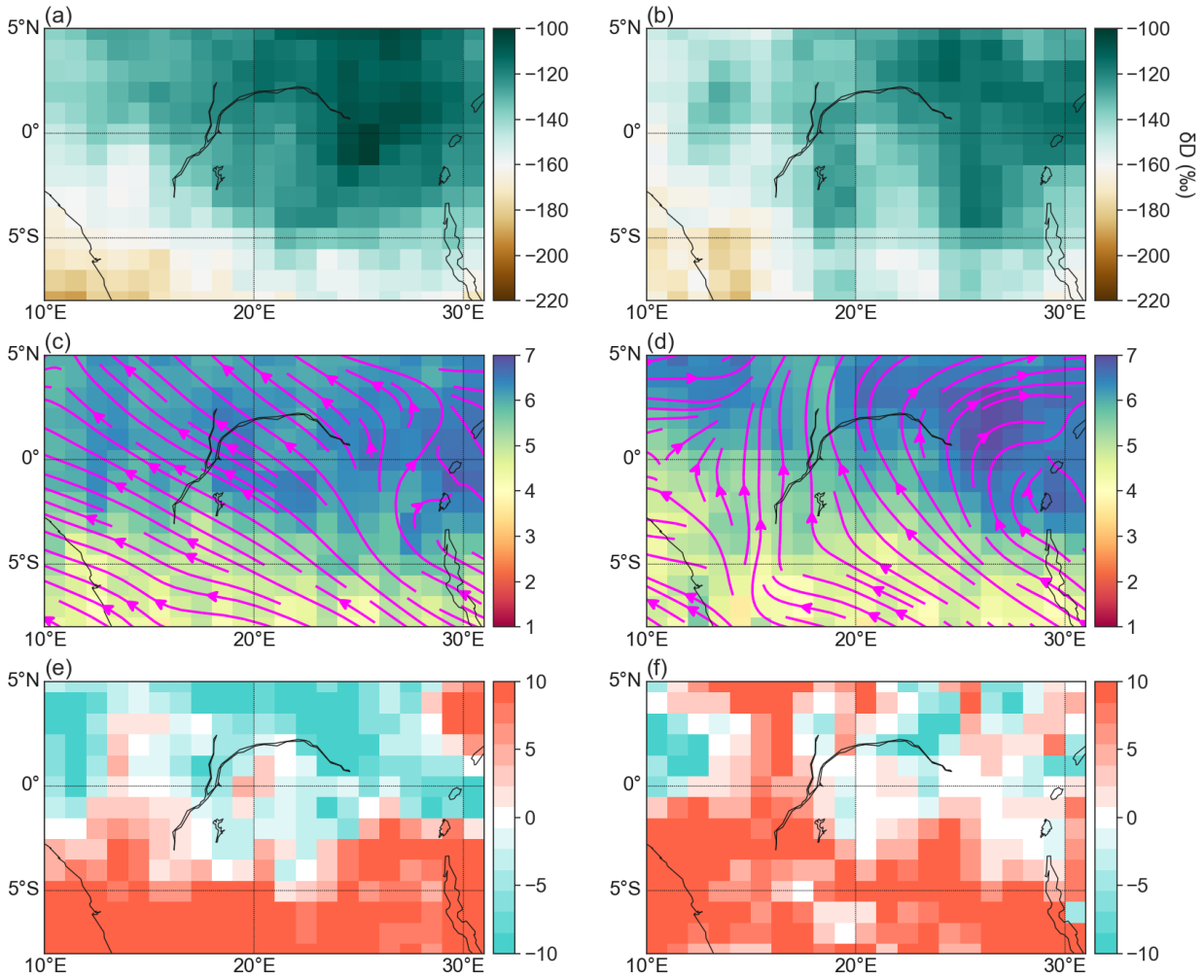

Figure 5.5 Spatial patterns of δD in the free atmosphere troposphere based on the TES measurements in (a) the March-May wet season and (b) June-August dry season for the period 2004-2015. (c-d) Same as (a-b) but for specific humidity ($g \cdot kg^{-1}$; shaded) in the free atmosphere based on the TES measurements and streamlines of horizontal winds at 850hPa from the MERRA2. (e-f) Same as (a-b) but for linear regression slope of δD against specific humidity ($‰/g \cdot kg^{-1}$) from TES**.**

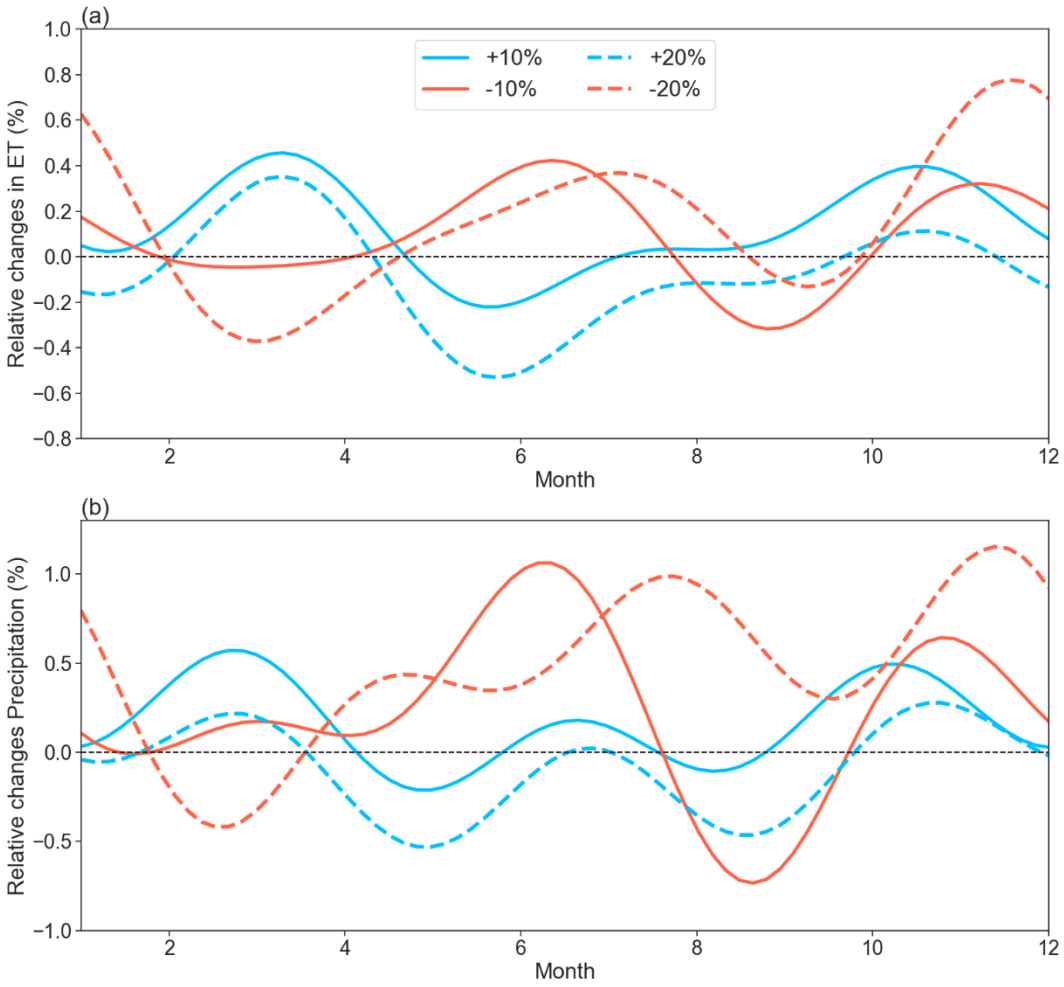

Figure 5.6 Regional mean differences in (a) ET and (b) precipitation between EXP and CTL simulations over the Congo Basin after removing daily and sub-daily noises by the fast Fourier transform.

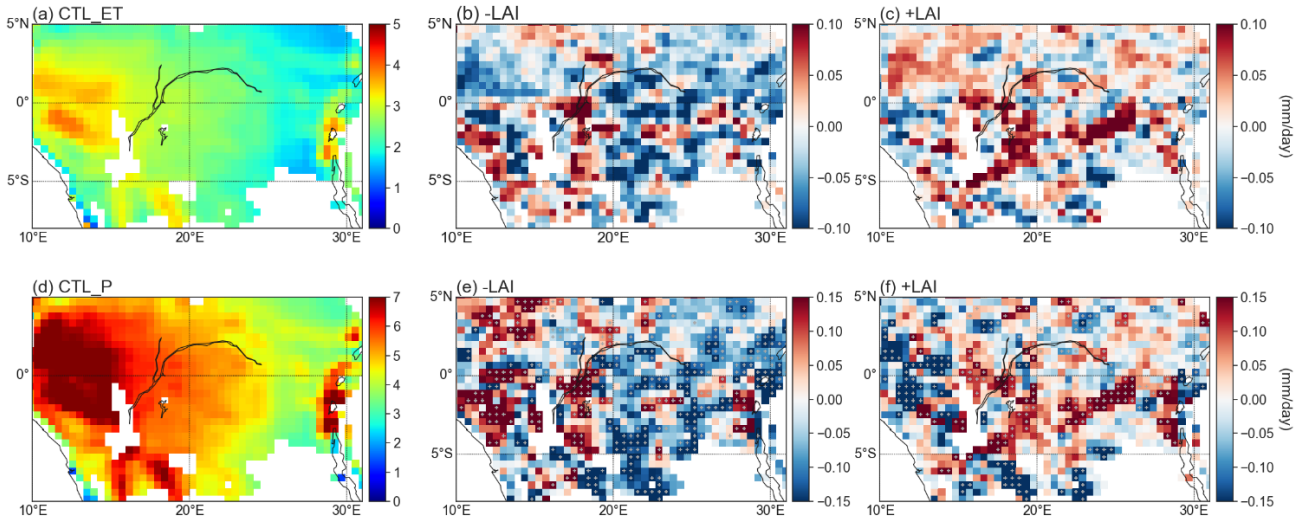

Figure 5.7 Simulated climatological spatial pattern of (a) ET (mm/d) and (d) precipitation (mm/d) during MAM from CTL. Spatial patterns of differences in (b) ET and (e) precipitation between EXP with negative LAI and SAI changes (-20%) and CTL. Spatial patterns of differences in (c) ET and (f) precipitation between EXP with positive LAI and SAI changes (+20%) and CTL. Grid boxes with gray dots indicate statistical significance at the 90% confidence level.

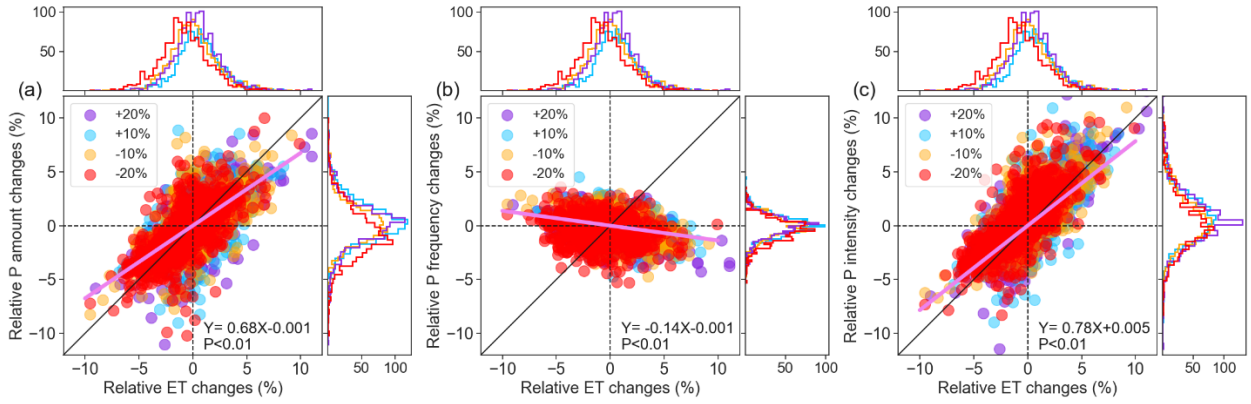

Figure 5.8 (a) Relative precipitation amount sensitivity to changes in ET over the Congo Basin during MAM calculated by EXP and CTL simulations. (b) Same as (a) but for the sensitivity of precipitation frequency. (c) Same as (a) but for the sensitivity of precipitation intensity. Possibility distribution functions of relative changes in precipitation amount, frequency, intensity, and ET in EXP are shown. The linear regression results of relative changes in precipitation amount, frequency, and intensity against relative changes in ET are presented as well.

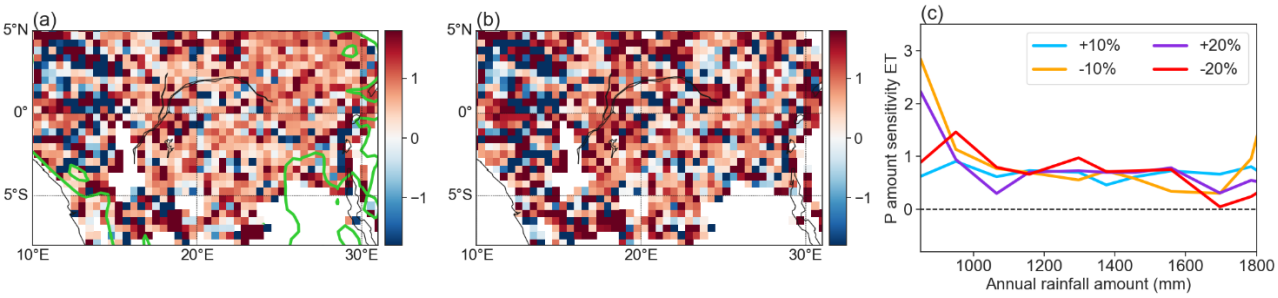

Figure 5.9 (a) Simulated spatial patterns of rainfall amount sensitivity (unitless) to ET changes during MAM over the Congo Basin. (b) Same as (a) but for the sensitivity of precipitation intensity. (c) Regional averaged precipitation sensitivity to ET changes for different hydroclimate categories (measured by the annual rainfall amount).

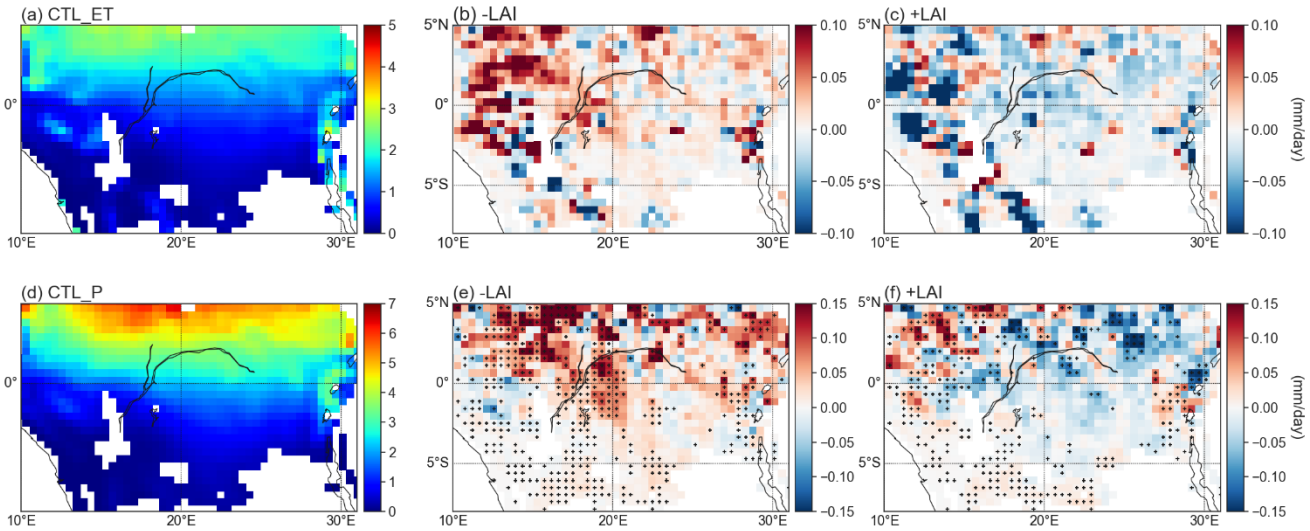

Figure 5.10 Same as figure 5.7 but during JJA.

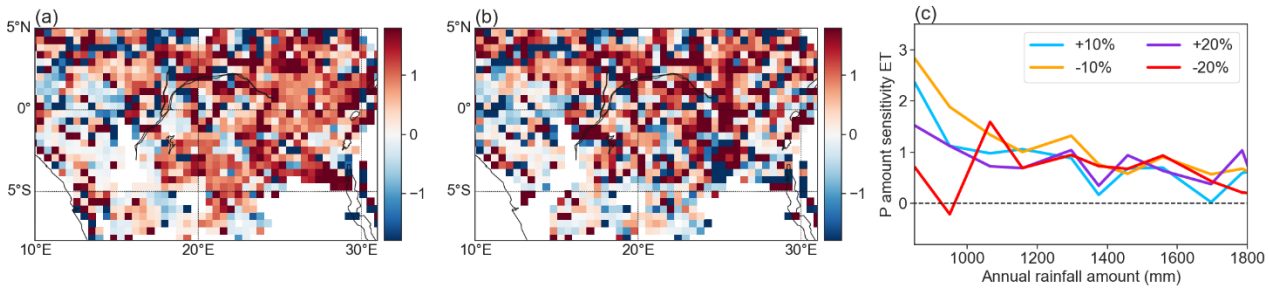

Figure 5.11 Same as figure 5.9 but during JJA.

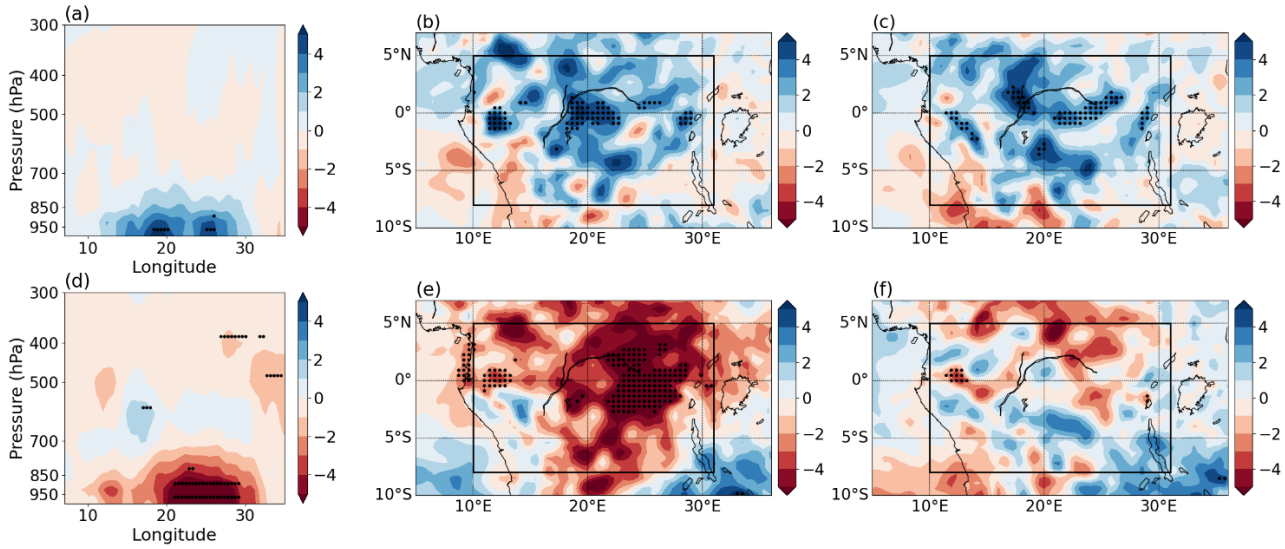

Figure 5.12 (a) Vertical cross section of differences in MAM specific humidity (10^{-2} g·kg^{-1}) between EXP with positive LAI and SAI changes (+20%) and CTL. (b) Spatial patterns of composite differences in specific humidity at 850hPa between EXP1 with positive LAI and SAI changes (+20%) and CTL. (c) Sames as (b) but with +10% LAI and SAI. (d-f) Same as (a-c) but for differences between EXP with negative LAI and SAI changes and CTL. Grid boxes with dots indicate statistical significance at the 90% confidence level.

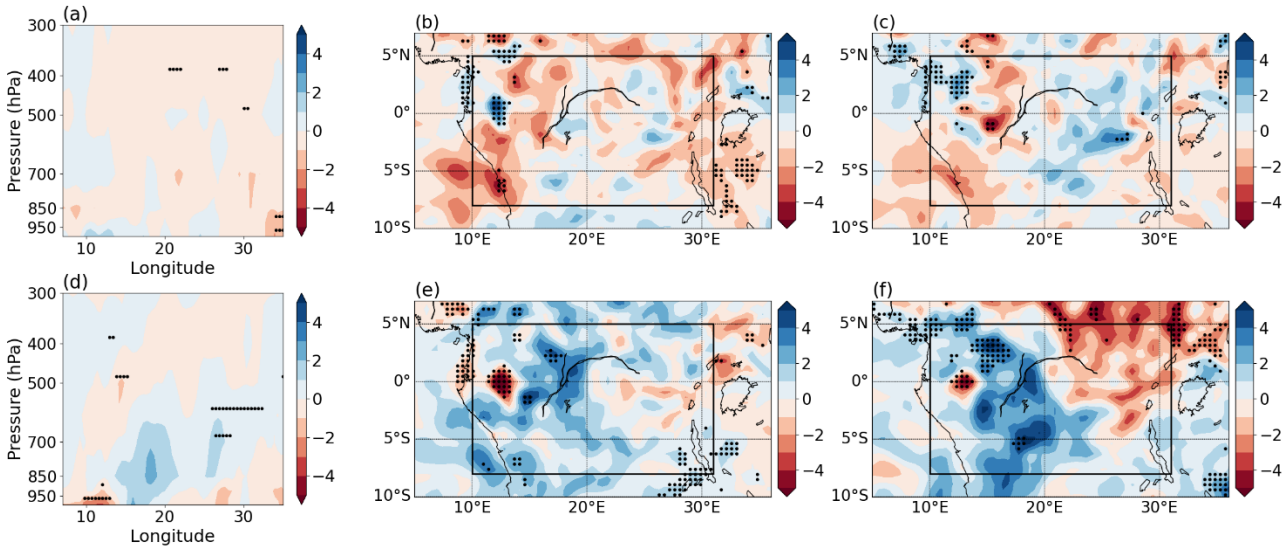

Figure 5.13 Same as figure 5.12 but during JJA.

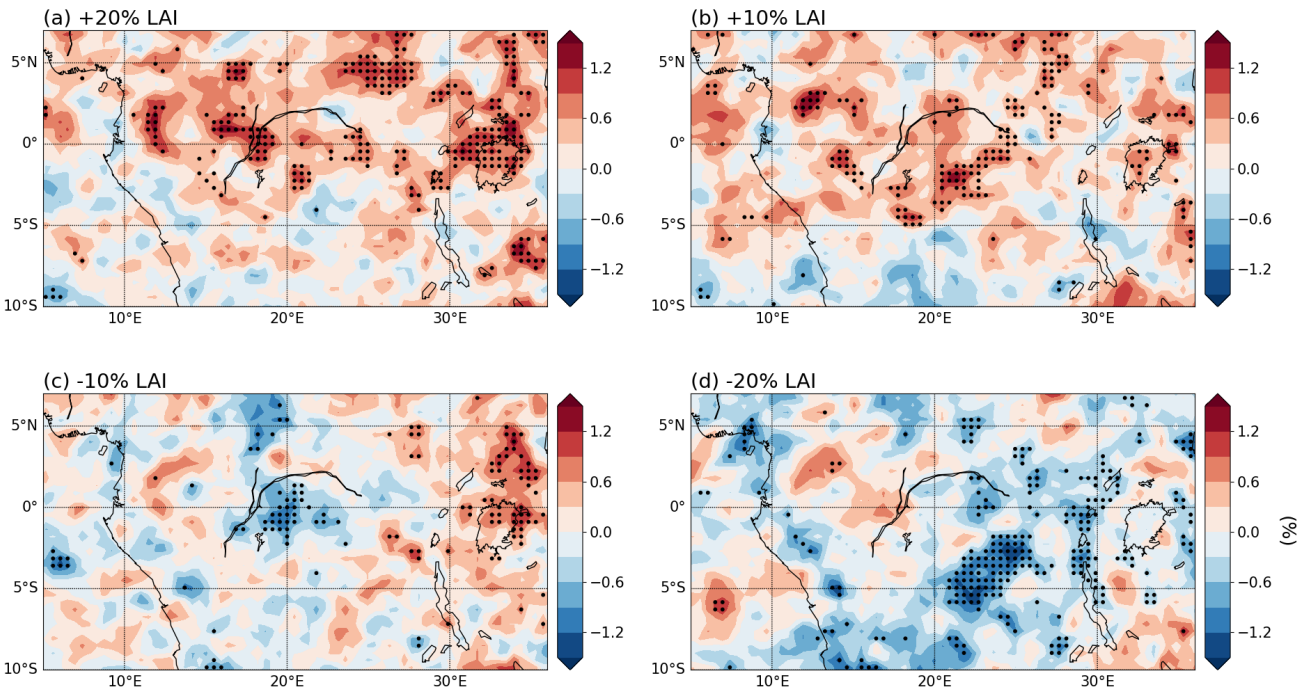

Figure 5.14 (a) Spatial patterns of composite differences in high cloud amount with positive LAI and SAI changes (+20%) and CTL. (b) Sames as (a) but with +10% LAI and SAI. (c-d) Same as (a-b) but for differences between EXP with negative LAI and SAI changes and CTL. Grid boxes with dots indicate statistical significance at the 90% confidence level.

Chapter 6 Concluding Remarks

6.1 Summary and Conclusions

The Congo rainforest, the world's second largest rainforest, has been experiencing an exclusive long-term drying trend since around the 1980s. This stunning rainfall variation is against the conventional paradigm indicating that wet regions would become wetter under the warming climate. This continuous drying trend raises big concerns on the sustainability of the Congolese rainforest, as it is drier and more fragmented compared to other tropical rainforests. What's more, the decreased precipitation and forest greenness threaten the carbon sink, biomes and human systems as well.

Based on previous studies, this dissertation aims at addressing three big questions: 1) How has precipitation seasonality, particularly the dry season length and intensity, changed in CEA? 2) Whether and how have wildfires varied along with the decreasing precipitation and potential changes in dry season? Answering these two questions will better characterize the drying trend and its hydrological and ecological implications over CEA. 3) How do tropical oceans and the rainforest affect precipitation activity respectively in CEA? Answering this question will improve the understanding of land-ocean-climate interactions and dominant factors influencing interannual and sub-seasonal precipitation variability. To overcome the caveats of limited observations in the Congo Basin, this dissertation adopted a wide range of newly available rainfall datasets, the latest satellite products measuring vegetation properties and fire activities, and advanced reanalysis data. To establish associations between CEA rainfall and tropical oceans, the partial correlation and composite analyses were applied. The impact of rainforest ET on precipitation was established by combining satellite-derived water isotopic data with sensitivity experiments conducted by the RegCM4.9.3 regional model.

The integral work was expanded into four detailed questions. Major findings of each question have been presented in four chapters. Chapter 2 addressed the very first research question on potential trends in DSL. Chapter 3 included observational variations in total burned area, frequency, and size of different fire categories. A machine learning algorithm was used to efficiently figure out leading factors regulating the variability and variations in wildfires. Chapter4 estimated the association between the tropical Indian Ocean and CEA rainfall and its increasing impacts on precipitation during September-December since the 1990s. Chapter5 established ET's impact on precipitation and quantify precipitation's sensitivity to different ET variations. A summary of these findings is listed as below.

In Chapter 2, we quantified potential trends in the boreal JJA summer dry season by using observational and reanalysis precipitation datasets and satellite-derived vegetation products measuring plant greenness, water content and photosynthesis. The results showed that the summer dry season has become longer for the period 1979-2015 from both hydrological and ecological perspectives. The DSL increased by 6.4-10.4 days per decade during 1988-201. This was concurrent with an earlier DSO estimated by precipitation data and a delayed DSE estimated by vegetation products. The earlier DSO can be attributed to long-term droughts in the pre-dry season. The delayed DSE resulted from insufficient replenished soil moisture, which postponed the start of the next wet season and hinders vegetation's regrowth. If such changes continue, the enhanced water stress in a warming climate may affect the carbon cycle and alter the composition and structure of evergreen rainforests.

In Chapter 3, trends in wildfires were investigated using the latest burned area data from the MODIS and the GFED4s products over Central Africa (10°E-40°E, 15°N-15°S). A 3-D (latitude, longitude, time) connected-component labeling algorithm was applied to identify individual fires

and their size. Results showed a decline in burned area by 2.7-3.2 Mha yr^{-1} (~1.3% yr^{-1}) for the period 2003-2017, particularly in northern Central Africa. This decline was attributed to significant decreases in both fire frequency and size, particularly for large fires (>100 ha) which contribute to ~90% of the total burned area. Burned area declined in tropical savannas and grasslands but increased at the edges of the Congolese rainforest. A random forest regression model was applied to quantify influences of climatic conditions, fuel availability, and agricultural activity on burned area changes. Overall, suppressed fuel, increased dry season length, and decreased rainfall contributed to significant declines in burned area in savannas and grasslands. In the edges of the southern Congolese rainforest, suppressed rainfall and warmer temperature were responsible for the increased burned area.

In Chapter 4, by using observational rainfall datasets, we identified a positive correlation between precipitation over CEA and the IOD during SOND for the period 1981-2019. Rainfall amount significantly increases during positive IOD events. The enhancement in precipitation is primarily attributed to increased rainfall frequency and reaches the maximum in October. IOD impacts rainfall via modifying the Walker circulation over the tropical Indian Ocean and moisture in the middle troposphere over CEA. The MJO activity covaries with IOD to modulate the African Easterly Jet, which is critical to convection development over CEA. SOND rainfall has increased for the last two decades, which is concurrent with increases in both the IOD index and the correlation between IOD and rainfall. The IOD-congruent rainfall changes potentially account for much of rainfall trends in southern and eastern CEA.

In Chapter 5, we focus on the impact of ET on precipitation in the Congo Basin. First, potential impacts of ET on precipitation were assessed by water isotopic observations. The results indicated that ET contributes to moisture sources supporting convection activity over the basin, particularly

during the MAM rainy season and the JJA dry season. ET plays critical roles in moisturizing and destabilizing the middle and lower troposphere and sustaining moisture convergence during the two seasons. Six groups of sensitivity experiments with different ET perturbations were conducted by the RegCM4.9.3 model coupled with the CLIM4.5 land model. This model performs well in capturing the climatology and seasonal cycle of precipitation patterns in the Congo Basin. In general, precipitation responds linearly and positively to ET variations during MAM and JJA, i.e., precipitation decreases (increases) with negative (positive) ET disturbances. The sensitivity of precipitation activity to ET is mainly attributed to the sensitivity of precipitation intensity. The regional model suggests that ET impacts precipitation mainly via affecting moisture distribution in the lower troposphere. During the MAM rainy season, increased humidity in the lower troposphere would enhance high cloud friction to increase precipitation under positive ET forcing. During the JJA dry season, moisture also increases in the lower troposphere when ET enhances, but less changes in cloud fractions.

6.2 Recommendations for Future Work

Studies from this dissertation identified the lengthening DSL and significant changes in wildfire attributable to variations in precipitation patterns. Terrestrial and oceanic impacts on precipitation were identified during different seasons and over different sub-regions in CEA. We suggest that Oceans' remote impacts and local rainforest functions contribute to the drying during the boreal spring and summer seasons. The Indian Ocean is closely associated with CEA precipitation variability and increased precipitation during the autumn rainy season. Considering the complexity and challenges in untangling various processes in vegetation-atmosphere-ocean interactions over the Congo Basin, improved understanding of the biogeochemical and

biogeophysical mechanisms that govern the Congo rainfall and ET and its intraseasonal-to-interdecadal variability, and how this variability may be influenced by anthropogenic climate change, are research questions of critical importance.

For example, this dissertation addresses the impacts of the tropical Indian Ocean and rainforest ET on precipitation. We found that the warmer tropical western Indian Ocean (positive IOD) would enhance precipitation over CEA and this positive association has strengthened during the past decades along with the warming trend in the tropical western Indian Ocean. Whether such changes are attributed to anthropogenic warming or internal variability of Earth system are still unknown. Considerable strong impacts of ET on precipitation have been found during the spring rainy season and summer dry season in the Congo Basin. Exacerbated decreases in ET and RZSM during April-August since 2000 have been observed as well. "How much of this can be attributed to decreased vegetation greenness" and "whether do these changes contribute to the exacerbated drying trend" are another two questions that need to be studied in the future work.

One big challenge in studying climate changes and ecology in the Congo Basin is the lack of good and long-term observations. Rain gauge has dramatically decreased since around the late 1990s (Washington et al. 2013). Combining satellite observations and reanalysis datasets, the continuous changes in precipitation and rainforest greenness have been observed. Active associations between precipitation and tropical oceans at season and sub-seasonal scales and rainforest's feedback on regional climate require recovering the monitoring of local weather and atmospheric conditions with finer spatial and temporal resolutions. Sufficient data resources are not only important to build the science capacity to solve previously unanswered questions on intra-seasonal rainfall-ocean-atmosphere interactions and vegetation-climate interactions, but also are critical to enable better plans for climate change mitigation and adaption.

BIBLIOGRAPHY

Abram, N.J., Gagan, M.K., Cole, J.E., Hantoro, W.S. and Mudelsee, M., 2008: Recent intensification of tropical climate variability in the Indian Ocean. *Nat. Geosci.*, **1**, 849-853.

Achard, F., Eva, H.D., Stibig, H.J., Mayaux, P., Gallego, J., Richards, T. and Malingreau, J.P., 2002: Determination of deforestation rates of the world's humid tropical forests. *Science*, **297**, 999-1002.

Adams, J., 1998: The distribution and variety of equatorial rain forest. http://www.esd.ornl.gov/projects/qen/rainfo.html

Albergel, C., De Rosnay, P., Balsamo, G., Isaksen, L. and Muñoz-Sabater, J., 2012: Soil moisture analyses at ECMWF: Evaluation using global ground-based in situ observations. *J. Hydrometeorol.*, 13, 1442-1460.

Aldersley, A., Murray, S., J. and Cornell, S., E., 2011: Global and regional analysis of climate and human drivers of wildfire *Sci. Total Environ.*, **409**, 3472-3481.

Alexander, M., A., Bladé, I., Newman, M., Lanzante, J., R., Lau, N., C. and Scott, J., D., 2002: The atmospheric bridge: The influence of ENSO teleconnections on air–sea interaction over the global oceans. *J. Clim.*, **15**, 2205-2231.

Allan, R.P., Soden, B.J., John, V.O., Ingram, W. and Good, P., 2010: Current changes in tropical precipitation. *Environ. Res. Lett.*, **5**, 025205.

Andela, N., Morton, D.C., Giglio, L., Chen, Y., van der Werf, G.R., Kasibhatla, P.S., DeFries, R.S., Collatz, G.J., Hantson, S., Kloster, S. and Bachelet, D., 2017: A human-driven decline in global burned area. *Science*, **356**, 1356-1362.

Andela, N. and van der Werf, G.R., 2014: Recent trends in African fires driven by cropland expansion and El Niño to La Niña transition. *Nat. Clim. Change*, **4**, 791-795.

Anderegg, W.R., Schwalm, C., Biondi, F., Camarero, J.J., Koch, G., Litvak, M., Ogle, K., Shaw, J.D., Shevliakova, E., Williams, A.P. and Wolf, A., 2015: Pervasive drought legacies in forest ecosystems and their implications for carbon cycle models. *Science*, **349**, 528-532.

Anyamba, A. and Tucker, C. J., 2012: in *Remote Sensing of Drought: Innovative Monitoring Approaches* (eds Wardlow B. D. et al.) Ch. 2, CGR Press.

Archibald, S., Lehmann, C.E., Belcher, C.M., Bond, W.J., Bradstock, R.A., Daniau, A.L., Dexter, K.G., Forrestel, E.J., Greve, M., He, T. and Higgins, S.I., 2018: Biological and geophysical feedbacks with fire in the Earth system. *Env. Res. Let.*, **13**, 033003.

Archibald, S., Nickless, A., Govender, N., Scholes, R.J. and Lehsten, V., 2010: Climate and the inter-annual variability of fire in southern Africa: a meta-analysis using long-term field data and satellite-derived burnt area data. *Glob. Ecol. Biogeog.*, **19**, 794-809.

Archibald, S. and Roy, D.P., 2009: July. Identifying individual fires from satellite-derived burned area data. *Proc. IGARSSS*, **3**, 160-163.

Archibald, S., Roy, D.P., van Wilgen, B.W. and Scholes, R.J., 2009: What limits fire? An examination of drivers of burnt area in Southern Africa. *Glob. Change Biol.*, **15**, 613-630.

Asefi-Najafabady, S. and Saatchi, S., 2013: Response of African humid tropical forests to recent rainfall anomalies. *Phil. Trans. R. Soc. B*, **368**, 20120306.

Ashton, M.S., Tyrrell, M.L., Spalding, D. and Gentry, B. eds., 2012*: Managing Forest Carbon in a Changing Climate*. Springer.

Atyi, E.A., Liboum, M., Guizol, P., Awono, A., Jungers, Q., Pokem, D.S.D., Sonwa, D.J., Palla, F., Sufo-Kankeu, R. and Djossi, D., 2019: *International financial flows to support nature protection and sustainable forest management in Central Africa*. Central Africa Forest Observatory.

Baccini, A., Walker, W., Carvalho, L., Farina, M., Sulla-Menashe, D. and Houghton, R.A., 2017: Tropical forests are a net carbon source based on aboveground measurements of gain and loss. *Science*, **358**, 230-234.

Baker, I.T., Prihodko, L., Denning, A.S., Goulden, M., Miller, S. and Da Rocha, H.R., 2008: Seasonal drought stress in the Amazon: Reconciling models and observations. *J. Geophys. Res.*, **113**, G00B01.

Balas, N., Nicholson, S.E. and Klotter, D., 2007: The relationship of rainfall variability in West Central Africa to sea-surface temperature fluctuations. *Int. J. Climatol.*, **27**, 1335-1349.

Beck, H.E., McVicar, T.R., van Dijk, A.I., Schellekens, J., de Jeu, R.A. and Bruijnzeel, L.A., 2011: Global evaluation of four AVHRR–NDVI data sets: Intercomparison and assessment against Landsat imagery. *Remote Sens. Environ.*, **115**, 2547-2563.

Bell, J.P., Tompkins, A.M., Bouka-Biona, C. and Sanda, I.S., 2015. A process-based investigation into the impact of the Congo basin deforestation on surface climate. *J. Geophys. Res. Atmos.*, **120**, 5721-5739.

Berg, A., Findell, K., Lintner, B., Giannini, A., Seneviratne, S.I., Van Den Hurk, B., Lorenz, R., Pitman, A., Hagemann, S., Meier, A. and Cheruy, F., 2016: Land–atmosphere feedbacks amplify aridity increase over land under global warming. *Nat. Clim. Change*, **6**, 869-874.

Bergman, J., W., Hendon, H., H., and Weickmann, K., M., 2001: Intraseasonal air–sea interactions at the onset of El Niño. *J. Clim.*, **14**, 1702-1719.

Berhane, F. G., 2016: Intraseasonal Precipitation variability over tropical Africa (Doctoral dissertation), Johns Hopkins University, Baltimore, MD, USA

Berhane, F., Zaitchik, B., and Badr, H. S., 2015: The Madden–Julian oscillation's influence on spring rainy season precipitation over equatorial West Africa. *J. Clim.*, **28**, 8653-8672.

Betts, R.A., 2004: Global vegetation and climate: self-beneficial effects, climate forcings and climate feedbacks. *Journal De Physique IV*, **121**, 37-60.

Biasutti, M. and Sobel, A.H., 2009: Delayed Sahel rainfall and global seasonal cycle in a warmer climate. *Geophys. Res. Lett.*, **36**.

Bistinas, I., Harrison, S.P., Prentice, I.C. and Pereira, J.M.C., 2014: Causal relationships versus emergent patterns in the global controls of fire frequency. *Biogeosciences*, **11**, 5087-5101.

Bond, W.J., Woodward, F.I. and Midgley, G.F., 2005: The global distribution of ecosystems in a world without fire. *New Phytol.*, **165**, 525-538.

Bosilovich, M.G., Schubert, S.D. and Walker, G.K., 2005: Global changes of the water cycle intensity. *J. Clim.*, **18**, 1591-1608.

Breiman, L., 2001: Random forests. *Mach*. *Learn*, **45**, 5-32.

Breiman, L. and Cutler, A., 2003: Setting up, using, and understanding random forests V4. 0 [online] http://oz.berkeley.edu/users/breiman/Using_random_forest_v4.0.pdf

Bunyard, P., 2014: How the Biotic Pump links the hydrological and the rainforest to climate: Is it for real? How can we prove it? University of Sergio Arboleda, Bogotá.

Bush, E.R., Jeffery, K., Bunnefeld, N., Tutin, C., Musgrave, R., Moussavou, G., Mihindou, V., Malhi, Y., Lehmann, D., Ndong, J.E. and Makaga, L., 2020: Rare ground data confirm significant warming and drying in western equatorial Africa. *Peer J*, **8**, e8732.

Cai, W., Cowan, T. and Sullivan, A., 2009: Recent unprecedented skewness towards positive Indian Ocean Dipole occurrences and its impact on Australian rainfall. *Geophys. Res. Lett.*, **36**.

Cai, W., Santoso, A., Wang, G., Weller, E., Wu, L., Ashok, K., Masumoto, Y. and Yamagata, T., 2014: Increased frequency of extreme Indian Ocean Dipole events due to greenhouse warming. *Nature*, **510**, 254-258.

Cai, W., Wu, L., Lengaigne, M., Li, T., McGregor, S., Kug, J.S., Yu, J.Y., Stuecker, M.F., Santoso, A., Li, X. and Ham, Y.G., 2019: Pantropical climate interactions. *Science*, **363**.

Cai, W., Yang, K., Wu, L., Huang, G., Santoso, A., Ng, B., Wang, G. and Yamagata, T., 2021: Opposite response of strong and moderate positive Indian Ocean Dipole to global warming. *Nat. Clim. Change*, **11**, 27-32.

Cai, W., Zheng, X.T., Weller, E., Collins, M., Cowan, T., Lengaigne, M., Yu, W. and Yamagata, T., 2013: Projected response of the Indian Ocean Dipole to greenhouse warming. *Nat. Geosci.*, **6**, 999-1007.

Cecil, D., J., Buechler, D., E. and Blakeslee, R., J., 2015: TRMM LIS climatology of thunderstorm occurrence and conditional lightning flash rates *J. Clim*., **28**, 6536-6547.

Chagnon, F.J.F., Bras, R.L. and Wang, J., 2004: Climatic shift in patterns of shallow clouds over the Amazon. *Geophys. Res. Lett.*, **31**, 24.

Charney, J.G., 1975: Dynamics of deserts and drought in the Sahel. *Q. J. R. Meteorolog. Soc.,* **101**, 193-202.

Cheng, L., Zhang, L., Wang, Y.P., Canadell, J.G., Chiew, F.H., Beringer, J., Li, L., Miralles, D.G., Piao, S. and Zhang, Y., 2017: Recent increases in terrestrial carbon uptake at little cost to the water cycle. *Nat. Commun.*, **8**, 1-10.

Chou, C., Neelin, J.D., Chen, C.A. and Tu, J.Y., 2009: Evaluating the "rich-get-richer" mechanism in tropical precipitation change under global warming. *J. Clim.*, **22**, 1982-2005.

Cochrane, M., A., Alencar, A., Schulze, M. D., Souza, C. M., Nepstad, D. C., Lefebvre, P. and Davidson, E., A., 1999: Positive feedbacks in the fire dynamic of closed canopy tropical forests. *Science*, **284**, 1832-1835.

Cochrane, M., A. and Laurance, W., F., 2002: Fire as a large-scale edge effect in Amazonian forests. *J. Trop. Ecol*., **18**, 311-325.

Collatz, G.J., Ball, J.T., Grivet, C. and Berry, J.A., 1991: Physiological and environmental regulation of stomatal conductance, photosynthesis and transpiration: a model that includes a laminar boundary layer. *Agri. For. Meteorol.*, **54**, 107-136.

Cox, P.M., Betts, R.A., Jones, C.D., Spall, S.A. and Totterdell, I.J., 2000: Acceleration of global warming due to carbon-cycle feedbacks in a coupled climate model. *Nature*, **408**, 184-187.

Dai, A., 2013: Increasing drought under global warming in observations and models. *Nat. Clim. Change*, **3**, 52-58.

Dai, A., Rasmussen, R.M., Liu, C., Ikeda, K. and Prein, A.F., 2020: A new mechanism for warm-season precipitation response to global warming based on convection-permitting simulations. *Clim. Dyn.*, **55**, 343-368.

Dantas, V.D.L., Hirota, M., Oliveira, R.S. and Pausas, J.G., 2016: Disturbance maintains alternative biome states. *Ecol. Lett.*, **19**, 12-19.

Dargie, G.C., Lewis, S.L., Lawson, I.T., Mitchard, E.T., Page, S.E., Bocko, Y.E. and Ifo, S.A., 2017: Age, extent and carbon storage of the central Congo Basin peatland complex. *Nature*, **542**, 86-90.

Dee, D.P., Uppala, S.M., Simmons, A.J., Berrisford, P., Poli, P., Kobayashi, S., Andrae, U., Balmaseda, M.A., Balsamo, G., Bauer, D.P. and Bechtold, P., 2011: The ERA-Interim reanalysis: Configuration and performance of the data assimilation system. *Q. J. R. Meteorol. Soc.*, **137**, 553-597.

Delire, C., Foley, J.A. and Thompson, S., 2004: Long-term variability in a coupled atmosphere–biosphere model. *J. Clim.*, **17**, 3947-3959.

DeMaria, M., DeMaria, R.T., Knaff, J.A. and Molenar, D., 2012: Tropical cyclone lightning and rapid intensity change. *Mon. Wea. Rev.*, **140**, 1828-1842.

Devaraju, N., Bala, G. and Modak, A., 2015: Effects of large-scale deforestation on precipitation in the monsoon regions: Remote versus local effects. *Proc. Natl. Acad. Sci.*, **112**, 3257-3262.

Didan. K., 2015: MOD13C1 MODIS/Terra Vegetation Indices 16-Day L3 Global 0.05Deg CMG V006 NASA EOSDIS Land Processes DAAC https://doi.org/10.5067/MODIS/MOD13C1.006

Dimiceli, C., Carroll, M., Sohlberg, R., Kim, D., H., Kelly. M, and Townshend, J., R., G., 2015: MOD44B MODIS/Terra Vegetation Continuous Fields Yearly L3 Global 250m SIN Grid V006 NASA EOSDIS Land Processes DAAC https://doi.org/10.5067/MODIS/MOD44B.006

Diro, G.T., Rauscher, S.A., Giorgi, F. and Tompkins, A.M., 2012: Sensitivity of seasonal climate and diurnal precipitation over Central America to land and sea surface schemes in RegCM4. *Clim. Res.*, **52**, 31-48.

Dominguez, F. and Kumar, P., 2008: Precipitation recycling variability and ecoclimatological stability—A study using NARR data. Part I: Central US plains ecoregion. *J. Clim.*, **21**, 5165-5186.

Dominguez, F., Kumar, P. and Vivoni, E.R., 2008: Precipitation recycling variability and ecoclimatological stability—A study using NARR data. Part II: North American monsoon region. *J. Clim.*, **21**, 5187-5203.

Dunning, C.M., Black, E.C. and Allan, R.P., 2016: The onset and cessation of seasonal rainfall over Africa. *J. Geophys. Res. Atmos.*, **121**, 11-405.

Dyer, E.L., Jones, D.B., Nusbaumer, J., Li, H., Collins, O., Vettoretti, G. and Noone, D., 2017: Congo Basin precipitation: Assessing seasonality, regional interactions, and sources of moisture. *J. Geophys. Res. Atmos.*, **122**, 6882-6898.

Eastman, J.R. and Fulk, M., 1993: Long sequence time series evaluation using standardized principal components. *Photo. Eng. Remote Sens.*, **59**, 991-996.

Ellwood, M.D. and Foster, W.A., 2004: Doubling the estimate of invertebrate biomass in a rainforest canopy. *Nature*, **429**, 549-551.

Eltahir, E.A. and Bras, R.L., 1994: Precipitation recycling in the Amazon basin. *Quart. J. Roy. Meteor. Soc.*, **120**, 861-880.

Enfield, D.B., Mestas-Nuñez, A.M., Mayer, D.A. and Cid-Serrano, L., 1999: How ubiquitous is the dipole relationship in tropical Atlantic sea surface temperatures?. *J. Geophys. Res.*, **104**, 7841-7848.

Engelbrecht, B.M., Comita, L.S., Condit, R., Kursar, T.A., Tyree, M.T., Turner, B.L. and Hubbell, S.P., 2007: Drought sensitivity shapes species distribution patterns in tropical forests. *Nature*, **447**, 80-82.

Enquist, B.J. and Enquist, C.A., 2011: Long-term change within a Neotropical forest: Assessing differential functional and floristic responses to disturbance and drought. *Glob. Change Biol.*, **17**, 1408-1424.

Erfanian, A., Wang, G. and Fomenko, L., 2017: Unprecedented drought over tropical South America in 2016: significantly under-predicted by tropical SST. *Sci. Rep.*, **7**, 1-11.

Fan, Y. and van den Dool, H., 2004: Climate Prediction Center global monthly soil moisture data set at 0.5 resolution for 1948 to present. *J. Geophys. Res. Atmos.*, **109**, D10102.

Fauset, S., Baker, T.R., Lewis, S.L., Feldpausch, T.R., Affum-Baffoe, K., Foli, E.G., Hamer, K.C. and Swaine, M.D., 2012: Drought - induced shifts in the floristic and functional composition of tropical forests in Ghana. *Ecol. Lett.*, **15**, 1120-1129.

Feng, X., Porporato, A. and Rodriguez-Iturbe, I., 2013: Changes in rainfall seasonality in the tropics. *Nat. Clim. Change*, **3**, 811-815.

Findell, K.L., Knutson, T.R. and Milly, P.C.D., 2006: Weak simulated extratropical responses to complete tropical deforestation. *J. Clim.*, **19**, 2835-2850.

Flannigan, M.D., Krawchuk, M.A., de Groot, W.J., Wotton, B.M. and Gowman, L.M., 2009: Implications of changing climate for global wildland fire. *Int. J. Wildland Fire*, **18**, 483-507.

Forkel, M., Dorigo, W., Lasslop, G., Chuvieco, E., Hantson, S., Heil, A., Teubner, I., Thonicke, K. and Harrison, S.P., 2019: Recent global and regional trends in burned area and their compensating environmental controls. *Environ. Res. Commun*., **1**, 051005.

Freeman, E., Woodruff, S.D., Worley, S.J., Lubker, S.J., Kent, E.C., Angel, W.E., Berry, D.I., Brohan, P., Eastman, R., Gates, L. and Gloeden, W., 2017: ICOADS Release 3.0: a major update to the historical marine climate record. *Int. J. Climatol.*, **37**, 2211-2232.

Friedl, M. and Sulla-Menashe, D., 2015: MCD12C1 MODIS/Terra+Aqua Land Cover Type Yearly L3 Global 0.05Deg CMG V006 *NASA EOSDIS Land Processes DAAC* https://doi.org/10.5067/MODIS/MCD12C1.006

Friedl, M.A., Sulla-Menashe, D., Tan, B., Schneider, A., Ramankutty, N., Sibley, A. and Huang, X., 2010: MODIS Collection 5 global land cover: Algorithm refinements and characterization of new datasets. *Remote Sens. Environ.*, **114**, 168-182.

Fu, C., 2003: Potential impacts of human-induced land cover change on East Asia monsoon. *Glob. Planet. Chang.*, **37**, 219-229.

Fu, R. and Li, W., 2004: The influence of the land surface on the transition from dry to wet season in Amazonia. *Theor. Appl. Climatol.*, **78**, 97-110.

Fu, R., Yin, L., Li, W., Arias, P.A., Dickinson, R.E., Huang, L., Chakraborty, S., Fernandes, K., Liebmann, B., Fisher, R. and Myneni, R.B., 2013: Increased dry-season length over southern Amazonia in recent decades and its implication for future climate projection. *Proc. Natl. Acad. Sci.*, **110**, 18110-18115.

Funk, C., Peterson, P., Landsfeld, M., Pedreros, D., Verdin, J., Shukla, S., Husak, G., Rowland, J., Harrison, L., Hoell, A. and Michaelsen, J., 2015: The climate hazards infrared precipitation with stations—a new environmental record for monitoring extremes. *Sci. Data*, **2**, 1-21.

Galewsky, J., Steen‐Larsen, H.C., Field, R.D., Worden, J., Risi, C. and Schneider, M., 2016: Stable isotopes in atmospheric water vapor and applications to the hydrologic cycle. *Rev. Geophys.*, **54**, 809-865.

Galiano, L., Martínez‐Vilalta, J. and Lloret, F., 2011: Carbon reserves and canopy defoliation determine the recovery of Scots pine 4 yr after a drought episode. *New Phytol.*, **190**, 750-759.

Gao, X., Shi, Y., Zhang, D., Wu, J., Giorgi, F., Ji, Z. and Wang, Y., 2012: Uncertainties in monsoon precipitation projections over China: results from two high-resolution RCM simulations. *Clim. Res.*, **52**, 213-226.

Gelaro, R., McCarty, W., Suárez, M.J., Todling, R., Molod, A., Takacs, L., Randles, C.A., Darmenov, A., Bosilovich, M.G., Reichle, R. and Wargan, K., 2017: The modern-era retrospective analysis for research and applications, version 2 (MERRA-2*). J. Clim.*, **30**, 5419-5454.

Gentine, P., Massmann, A., Lintner, B.R., Hamed Alemohammad, S., Fu, R., Green, J.K., Kennedy, D. and Vilà-Guerau de Arellano, J., 2019: Land–atmosphere interactions in the tropics–a review. *Hydrol. Earth Syst. Sci*., **23**, 4171-4197.

Giannini, A., Saravanan, R. and Chang, P., 2003: Oceanic forcing of Sahel rainfall on interannual to interdecadal time scales. *Science*, **302**, 1027-1030.

Giglio, L., Boschetti, L., Roy, D.P., Humber, M.L. and Justice, C.O., 2018: The Collection 6 MODIS burned area mapping algorithm and product. *Remote Sens. Environ.*, **217**, 72-85.

Giglio, L., Schroeder, W. and Justice, C.O., 2016: The collection 6 MODIS active fire detection algorithm and fire products. . *Remote Sens. Environ.*, **178**, 31-41.

Giglio, L., Randerson, J.T. and Van Der Werf, G.R., 2013: Analysis of daily, monthly, and annual burned area using the fourth - generation global fire emissions database (GFED4*). J. Geophys. Res. Biogeosci.*, **118**, 317-328.

Giorgi, F., Coppola, E., Solmon, F., Mariotti, L., Sylla, M.B., Bi, X., Elguindi, N., Diro, G.T., Nair, V., Giuliani, G. and Turuncoglu, U.U., 2012: RegCM4: model description and preliminary tests over multiple CORDEX domains. *Clim. Res.*, **52**, 7-29.

Good, S.P. and Caylor, K.K., 2011: Climatological determinants of woody cover in Africa. *Proc. Natl Acad. Sci. USA*, **108**, 4902-4907.

Green, J.K., Konings, A.G., Alemohammad, S.H., Berry, J., Entekhabi, D., Kolassa, J., Lee, J.E. and Gentine, P., 2017: Regionally strong feedbacks between the atmosphere and terrestrial biosphere. *Nat. Geosci.*, **10**, 410-414.

Grell, G.A., Dudhia, J. and Stauffer, D.R., 1994: A description of the fifth-generation Penn State/NCAR Mesoscale Model (MM5). *NCAR Tech. Note*, **121**.

Guan, K., Good, S.P., Caylor, K.K., Sato, H., Wood, E.F. and Li, H., 2014: Continental-scale impacts of intra-seasonal rainfall variability on simulated ecosystem responses in Africa. *Biogeosciences*, **11**, 6939-6954.

Guan, K., Good, S.P., Caylor, K.K., Medvigy, D., Pan, M., Wood, E.F., Sato, H., Biasutti, M., Chen, M., Ahlström, A. and Xu, X., 2018: Simulated sensitivity of African terrestrial ecosystem photosynthesis to rainfall frequency, intensity, and rainy season length. *Environ. Res. Lett.*, **13**, 025013.

Guan, K., Pan, M., Li, H., Wolf, A., Wu, J., Medvigy, D., Caylor, K.K., Sheffield, J., Wood, E.F., Malhi, Y. and Liang, M., 2015. Photosynthetic seasonality of global tropical forests constrained by hydroclimate. *Nat. Geosci.*, **8**, 284-289.

Hagos, S. and Leung, L.R., 2012: On the relationship between uncertainties in tropical divergence and the hydrological cycle in global models. *J. Clim.*, **25**, 381-391.

Harper, A.B., Denning, A.S., Baker, I.T., Branson, M.D., Prihodko, L. and Randall, D.A., 2010: Role of deep soil moisture in modulating climate in the Amazon rainforest. *Geophys. Res. Lett.*, **37**, L05802.

Harper, A., Baker, I.T., Denning, A.S., Randall, D.A., Dazlich, D. and Branson, M., 2014: Impact of evapotranspiration on dry season climate in the Amazon forest. *J. Clim.*, **27**, 574-591.

Hasler, N. and Avissar, R., 2007: What controls evapotranspiration in the Amazon basin?. *J. Hydrometeor.*, **8**, 380-395.

He, L., Ren, X., Gao, Q., Zhao, X., Yao, B. and Chao, Y., 2017: The connected-component labeling problem: A review of state-of-the-art algorithms. *Pattern Recognit.*, **70**, 25-43.

Held, I.M. and Soden, B.J., 2006: Robust responses of the hydrological cycle to global warming. *J. Clim.*, **19**, 5686-5699.

Hendon, H.H., Zhang, C. and Glick, J.D., 1999: Interannual variation of the Madden–Julian oscillation during austral summer. *J. Clim.*, **12**, 2538-2550.

Hernandez, C., Keribin, C., Drobinski, P. and Turquety, S., 2015: December. Statistical modelling of wildfire size and intensity: a step toward meteorological forecasting of summer extreme fire risk. *Ann. Geophys*., **33**, 1495-1506.

Hirota, M., Holmgren, M., Van Nes, E.H. and Scheffer, M., 2011: Global resilience of tropical forest and savanna to critical transitions. *Science*, **334**, 232-235.

Hirsch, R.M. and Archfield, S.A., 2015: Flood trends: Not higher but more often. *Nat. Clim. Change*, **5**, 198-199.

Hoell, A., Barlow, M., Wheeler, M.C. and Funk, C., 2014: Disruptions of El Niño–southern oscillation teleconnections by the Madden–Julian Oscillation. *Geophys. Res. Lett.,* **41**, 998-1004.

Hoerling, M., Hurrell, J., Eischeid, J. and Phillips, A., 2006: Detection and attribution of twentieth-century northern and southern African rainfall change. *J. Clim.*, **19**, 3989-4008.

Holtslag, A.A.M., De Bruijn, E.I.F. and Pan, H.L., 1990: A high resolution air mass transformation model for short-range weather forecasting. *Mon. Weather Rev.*, **118**, 1561-1575.

Hua, W., Zhou, L., Chen, H., Nicholson, S.E., Raghavendra, A. and Jiang, Y., 2016: Possible causes of the Central Equatorial African long-term drought. *Environ. Res. Lett.*, **11**, 124002.

Hua, W., Zhou, L., Chen, H., Nicholson, S.E., Jiang, Y. and Raghavendra, A., 2018: Understanding the Central Equatorial African long-term drought using AMIP-type simulations. *Clim. Dyn.*, **50**, 1115-1128.

Hua, W., Zhou, L., Nicholson, S.E., Chen, H. and Qin, M., 2019: Assessing reanalysis data for understanding rainfall climatology and variability over Central Equatorial Africa. *Clim. Dynam.*, **53**, 651-669.

Huete, A.R., Didan, K., Shimabukuro, Y.E., Ratana, P., Saleska, S.R., Hutyra, L.R., Yang, W., Nemani, R.R. and Myneni, R., 2006: Amazon rainforests green‐up with sunlight in dry season. *Geophys. Res. Lett.*, **33**, L06405.

Huffman, G.J., Bolvin, D.T., Nelkin, E.J., Wolff, D.B., Adler, R.F., Gu, G., Hong, Y., Bowman, K.P. and Stocker, E.F., 2007: The TRMM Multisatellite Precipitation Analysis (TMPA): Quasi-global, multiyear, combined-sensor precipitation estimates at fine scales. *J. Hydrometeor.*, **8**, 38-55.

IPCC. 2002: *Climate change 2001: the scientific basis.* Cambridge University Press.

James, R., Washington, R. and Rowell, D.P., 2013: Implications of global warming for the climate of African rainforests. *Phil. Trans. R. Soc. B*, **368**, 20120298.

Jasechko, S., Sharp, Z.D., Gibson, J.J., Birks, S.J., Yi, Y. and Fawcett, P.J., 2013: Terrestrial water fluxes dominated by transpiration. *Nature*, **496**, 347-350.

Jiang, Y., Zhou, L., Tucker, C.J., Raghavendra, A., Hua, W., Liu, Y.Y. and Joiner, J., 2019: Widespread increase of boreal summer dry season length over the Congo rainforest. *Nat. Clim. Change*, **9**, 617-622.

Jiang, Y., Zhou, L. and Raghavendra, A., 2020: Observed changes in fire patterns and possible drivers over Central Africa. *Environ. Res. Lett.*, **15**, 0940b8.

Jiang, Y., Zhou, L., Roundy, P.E., Hua, W. and Raghavendra, A., 2021: Increasing Influence of Indian Ocean Dipole on Precipitation over Central Equatorial Africa. *Geophys. Res. Lett.*, **48**, e2020GL092370.

Joiner, J., Guanter, L., Lindstrot, R., Voigt, M., Vasilkov, A.P., Middleton, E.M., Huemmrich, K.F., Yoshida, Y. and Frankenberg, C., 2013: Global monitoring of terrestrial chlorophyll fluorescence from moderate-spectral-resolution near-infrared satellite measurements: methodology, simulations, and application to GOME-2. *Atmos. Meas. Tech.*, **6**, 2803-2823.

Joiner, J., Yoshida, Y., Vasilkov, A.P. and Middleton, E.M., 2011: First observations of global and seasonal terrestrial chlorophyll fluorescence from space. *Biogeosciences*, **8**, 637-651.

Joiner, J., Yoshida, Y., Guanter, L. and Middleton, E.M., 2016: New methods for the retrieval of chlorophyll red fluorescence from hyperspectral satellite instruments: simulations and application to GOME-2 and SCIAMACHY. *Atmos. Meas. Tech.*, **9**, 3939-3967.

Jolly, W.M., Cochrane, M.A., Freeborn, P.H., Holden, Z.A., Brown, T.J., Williamson, G.J. and Bowman, D.M., 2015: Climate-induced variations in global wildfire danger from 1979 to 2013. *Nat. Commun.*, **6**, 1-11.

Kiehl, J.T., 1996: Description of the NCAR community climate model (CCM3). *NCAR Tech. Note*, **152**.

Knapp, K.R., Ansari, S., Bain, C.L., Bourassa, M.A., Dickinson, M.J., Funk, C., Helms, C.N., Hennon, C.C., Holmes, C.D., Huffman, G.J. and Kossin, J.P., 2011: Globally gridded satellite observations for climate studies. *Bull. Amer. Meteor. Soc.*, **92**, 893-907.

Kolus, H.R., Huntzinger, D.N., Schwalm, C.R., Fisher, J.B., McKay, N., Fang, Y., Michalak, A.M., Schaefer, K., Wei, Y., Poulter, B. and Mao, J., 2019: Land carbon models underestimate the severity and duration of drought's impact on plant productivity. *Sci. Rep.*, **9**, 1-10.

Krause, A.G. and Weis, E., 1991: Chlorophyll fluorescence and photosynthesis: the basics. *Annu. Rev. Plant Physiol. Plant Mol. Biol.*, **42**, 313-349.

Kug, J.S., Sooraj, K.P., Jin, F.F., Luo, J.J. and Kwon, M., 2009: Impact of Indian Ocean dipole on high-frequency atmospheric variability over the Indian Ocean. *Atmos. Res.*, **94**, 134-139.

Kumar, P., 2013: Seasonal rain changes. *Nat. Clim. Change*, **3**, 783-784.

Kumar, K.K., Rajagopalan, B. and Cane, M.A., 1999: On the weakening relationship between the Indian monsoon and ENSO. *Science*, **284**, 2156-2159.

Kumar, A., Yang, F., Goddard, L. and Schubert, S., 2004: Differing trends in the tropical surface temperatures and precipitation over land and oceans. *J. Clim.*, **17**, 653-664.

Laris, P., 2011: Humanizing savanna biogeography: linking human practices with ecological patterns in a frequently burned savanna of southern Mali. *Ann. Assoc. Am. Geogr.*, **101**, 1067-1088.

Lasslop, G. and Kloster, S., 2017: Human impact on wildfires varies between regions and with vegetation productivity. *Env. Res. Lett*., **12**, 115011.

Lawrence, A., Phillips, O.L., Ismodes, A.R., Lopez, M., Rose, S., Wood, D. and Farfan, A.J., 2005: Local values for harvested forest plants in Madre de Dios, Peru: towards a more contextualised interpretation of quantitative ethnobotanical data. *Biodivers. Conserv.*, **14**, 45-79.

Lay, E.H., Holzworth, R.H., Rodger, C.J., Thomas, J.N., Pinto Jr, O. and Dowden, R.L., 2004: WWLL global lightning detection system: Regional validation study in Brazil. *Geophys. Res. Lett.*, **31**, L03102.

Le Quéré, C., Andrew, R.M., Canadell, J.G., Sitch, S., Korsbakken, J.I., Peters, G.P., Manning, A.C., Boden, T.A., Tans, P.P., Houghton, R.A. and Keeling, R.F., 2016: Global carbon budget 2016. *Earth Sys. Sci. Data*, **8**, 605-649.

Lehmann, C.E., Anderson, T.M., Sankaran, M., Higgins, S.I., Archibald, S., Hoffmann, W.A., Hanan, N.P., Williams, R.J., Fensham, R.J., Felfili, J. and Hutley, L.B., 2014: Savanna vegetation-fire-climate relationships differ among continents. *Science*, **343**, 548-552.

Lewis, S.L., 2006: Tropical forests and the changing earth system. *Phil. Trans. R. Soc. B*, **361**, 195-210.

Li, W. and Fu, R., 2004: Transition of the large-scale atmospheric and land surface conditions from the dry to the wet season over Amazonia as diagnosed by the ECMWF re-analysis. *J. Clim.*, **17**, 2637-2651.

Li, Y., Piao, S., Li, L.Z., Chen, A., Wang, X., Ciais, P., Huang, L., Lian, X., Peng, S., Zeng, Z. and Wang, K., 2018: Divergent hydrological response to large-scale afforestation and vegetation greening in China. *Sci. Adv.*, **4**, eaar4182.

Liebmann, B., Bladé, I., Kiladis, G.N., Carvalho, L.M., Senay, G.B., Allured, D., Leroux, S. and Funk, C., 2012: Seasonality of African precipitation from 1996 to 2009. *J. Clim.*, **25**, 4304-4322.

Liebmann, B. and Smith, C.A., 1996: Description of a complete (interpolated) outgoing longwave radiation dataset. *Bull. Am. Meteorol. Soc.*, **77**, 1275-1277.

Liu, Y.Y., van Dijk, A.I., McCabe, M.F., Evans, J.P. and de Jeu, R.A., 2013: Global vegetation biomass change (1988–2008) and attribution to environmental and human drivers. *Glob. Ecol. Biogeogr.*, **22**, 692-705.

Liu, Y.Y., Van Dijk, A.I., De Jeu, R.A., Canadell, J.G., McCabe, M.F., Evans, J.P. and Wang, G., 2015: Recent reversal in loss of global terrestrial biomass. *Nat. Clim. Change*, **5**, 470-474.

Lu, J. and Delworth, T.L., 2005: Oceanic forcing of the late 20th century Sahel drought. *Geophys. Res. Lett.*, **32**.

Lumbroso, D.M., Woolhouse, G. and Jones, L., 2015: A review of the consideration of climate change in the planning of hydropower schemes in sub-Saharan Africa. *Clim. Change*, **133**, 621-633.

Ma, S. and Zhou, T., 2016: Robust strengthening and westward shift of the tropical Pacific Walker circulation during 1979–2012: A comparison of 7 sets of reanalysis data and 26 CMIP5 models. *J. Clim.*, **29**, 3097-3118.

Makarieva, A.M. and Gorshkov, V.G., 2007: Biotic pump of atmospheric moisture as driver of the hydrological cycle on land. *Hydrol. Earth Syst. Sci.*, **11**, 1013-1033.

Makarieva, A.M., Gorshkov, V.G., Sheil, D., Nobre, A.D. and Li, B.L., 2013: Where do winds come from? A new theory on how water vapor condensation influences atmospheric pressure and dynamics. *Atmos. Chem. Phys.*, **13**, 1039-1056.

Malhi, Y., Roberts, J.T., Betts, R.A., Killeen, T.J., Li, W. and Nobre, C.A., 2008: Climate change, deforestation, and the fate of the Amazon. *Science*, **319**, 169-172.

Malhi, Y. and Wright, J., 2004: Spatial patterns and recent trends in the climate of tropical rainforest regions. *Proc. R. Soc. of Lond. B.*, **359**, 311-329.

Maloney, E.D., Adames, Á.F. and Bui, H.X., 2019: Madden–Julian oscillation changes under anthropogenic warming. *Nat. Clim. Change*, **9**, 26-33.

Marengo, J.A., Nobre, C.A., Tomasella, J., Oyama, M.D., De Oliveira, G.S., De Oliveira, R., Camargo, H., Alves, L.M. and Brown, I.F., 2008. The drought of Amazonia in 2005: *J. Clim.*, **21**, 495-516.

Marengo, J.A., Tomasella, J., Alves, L.M., Soares, W.R. and Rodriguez, D.A., 2011: The drought of 2010 in the context of historical droughts in the Amazon region. *Geophys. Res. Lett.*, **38**, 1096-1104.

Marlon, J.R., Bartlein, P.J., Carcaillet, C., Gavin, D.G., Harrison, S.P., Higuera, P.E., Joos, F., Power, M.J. and Prentice, I.C., 2008: Climate and human influences on global biomass burning over the past two millennia. *Nat. Geos.*, **1**, 697-702.

Martens, B., Miralles, D.G., Lievens, H., Van Der Schalie, R., De Jeu, R.A., Fernández-Prieto, D., Beck, H.E., Dorigo, W.A. and Verhoest, N.E., 2017: GLEAM v3: Satellite-based land evaporation and root-zone soil moisture. *Geosci. Model Dev.*, **10**, 1903-1925.

Martens, B., Waegeman, W., Dorigo, W.A., Verhoest, N.E. and Miralles, D.G., 2018: Terrestrial evaporation response to modes of climate variability. *Npj Clim. Atmos. Sci.*, **1**, 1-7.

Marvel, K. and Bonfils, C., 2013: Identifying external influences on global precipitation. *Proc. Natl Acad. Sci. USA*, **110**, 19301-19306.

Masih, I., Maskey, S., Mussá, F.E.F. and Trambauer, P., 2014: A review of droughts on the African continent: a geospatial and long-term perspective. *Hydrol. Earth Syst. Sci.*, **18**, 3635-3649.

Mayr, M.J., Vanselow, K.A. and Samimi, C., 2018: Fire regimes at the arid fringe: A 16-year remote sensing perspective (2000–2016) on the controls of fire activity in Namibia from spatial predictive models. *Ecol. Ind.*, 91, 324-337.

McAlpine, C.A., Johnson, A., Salazar, A., Syktus, J., Wilson, K., Meijaard, E., Seabrook, L., Dargusch, P., Nordin, H. and Sheil, D., 2018: Forest loss and Borneo's climate. *Environ. Res. Lett.*, **13**, 044009.

Millán, M.M., 2014: Extreme hydrometeorological events and climate change predictions in Europe. *J. Hydrol.*, **518**, 206-224.

Miralles, D.G., Holmes, T.R.H., De Jeu, R.A.M., Gash, J.H., Meesters, A.G.C.A. and Dolman, A.J., 2011: Global land-surface evaporation estimated from satellite-based observations. *Hydrol. Earth Syst. Sci.*, 15, 453-469.

Miralles, D.G., Van Den Berg, M.J., Gash, J.H., Parinussa, R.M., De Jeu, R.A., Beck, H.E., Holmes, T.R., Jiménez, C., Verhoest, N.E., Dorigo, W.A. and Teuling, A.J., 2014: El Niño–La Niña cycle and recent trends in continental evaporation. *Nat. Clim. Change*, **4**, 122-126.

Mitchard, E.T., 2018: The tropical forest carbon cycle and climate change. *Nature*, **559**, 527-534.

Molod, A., Takacs, L., Suarez, M. and Bacmeister, J., 2015: Development of the GEOS-5 atmospheric general circulation model: Evolution from MERRA to MERRA2. *Geosci. Model Dev.*, **8**, 1339-1356.

Myneni, R.B., Hoffman, S., Knyazikhin, Y., Privette, J.L., Glassy, J., Tian, Y., Wang, Y., Song, X., Zhang, Y., Smith, G.R. and Lotsch, A., 2002: Global products of vegetation leaf area and fraction absorbed PAR from year one of MODIS data. *Remote Sens. Environ.*, **83**, 214-231.

NASA/LARC/SD/ASDC, 2017: CERES and GEO-Enhanced TOA, Within-Atmosphere and Surface Fluxes, Clouds and Aerosols Daily Terra-Aqua Edition4A. Available at: https://doi.org/10.5067/Terra+Aqua/CERES/SYN1degDay_L3.004A.

National Research Council (NRC), 200: Climate Data Records from Environmental Satellites vol. 150 National Academics Press, Washington, DC.

Nepstad, D.C., Verssimo, A., Alencar, A., Nobre, C., Lima, E., Lefebvre, P., Schlesinger, P., Potter, C., Moutinho, P., Mendoza, E. and Cochrane, M., 1999: Large-scale impoverishment of Amazonian forests by logging and fire. *Nature*, **398**, 505-508.

Nicholson, S.E., Some, B. and Kone, B., 2000a: An analysis of recent rainfall conditions in West Africa, including the rainy seasons of the 1997 El Niño and the 1998 La Niña years. *J. Clim.*, **13**, 2628-2640.

Nicholson, S.E., 2000b: The nature of rainfall variability over Africa on time scales of decades to millenia. *Glob. Planet. Change*, **26**, 137-158.

Nicholson, S.E., 2001: Climatic and environmental change in Africa during the last two centuries. *Clim. Res.*, **17**, 123-144.

Nicholson, S.E. and Dezfuli, A.K., 2013: The relationship of rainfall variability in western equatorial Africa to the tropical oceans and atmospheric circulation. Part I: The boreal spring. *J. Clim.*, **26**, 45-65.

Nicholson, S.E., 2018a: The ITCZ and the seasonal cycle over equatorial Africa. *Bull. Amer. Meteor. Soc.*, **99**, 337-348.

Nicholson, S.E., Klotter, D., Dezfuli, A.K. and Zhou, L., 2018b: New rainfall datasets for the Congo Basin and surrounding regions. *J. Hydrometeorol.*, 19, 1379-1396.

Nicholson, S.E., Klotter, D., Zhou, L. and Hua, W., 2019: Validation of satellite precipitation estimates over the Congo Basin. *J. Hydrometeorol.*, **20**, 631-656.

Oleson, K.W., Lawrence, D.M., Bonan, G.B., Drewniak, B., Huang, M., Koven, C.D., Levis, S., Li, F., Riley, W., Subin, Z. and Swenson, S.C., 2010: Technical description of version 4.5 of the Community Land Model (CLM), *NCAR Tech. Notes*, **10**.

Otto, F.E., Jones, R.G., Halladay, K. and Allen, M.R., 2013: Attribution of changes in precipitation patterns in African rainforests. *Philos. Trans. R. Soc. B*, **368**, 20120299.

Paeth, H., Born, K., Podzun, R. and Jacob, D., 2005: Regional dynamical downscaling over West Africa: model evaluation and comparison of wet and dry years. *Meteorol. Z.*, **14**, 349-367.

Pal, J.S., Small, E.E. and Eltahir, E.A., 2000: Simulation of regional‐scale water and energy budgets: Representation of subgrid cloud and precipitation processes within RegCM. *J. Geophys. Res.*, **105**, 29579-29594.

Pallardy, S.G., Čermák, J., Ewers, F.W., Kaufmann, M.R., Parker, W.C. and Sperry, J.S., 1995: Water transport dynamics in trees and stands. *In Resource physiology of conifers* (301-389). Academic Press.

Patra, P.K., Ishizawa, M., Maksyutov, S., Nakazawa, T. and Inoue, G., 2005: Role of biomass burning and climate anomalies for land‐atmosphere carbon fluxes based on inverse modeling of atmospheric CO2. *Global Biogeochem. Cycles*, **19**, GB3005.

Pechony, O. and Shindell, D.T., 2010: Driving forces of global wildfires over the past millennium and the forthcoming century. *Proc. Natl. Acad. Sci.*, **107**, 19167-19170.

Peters, T. 2016; Water balance in tropical regions. In L. Pancel & M. Köhl (Eds.), *Tropical forestry handbook*, 391-403. Springer.

Pinzon, J.E. and Tucker, C.J., 2014: A non-stationary 1981–2012 AVHRR NDVI3g time series. *Remote Sens.*, **6**, 6929-6960.

Pohl, B. and Matthews, A.J., 2007: Observed changes in the lifetime and amplitude of the Madden–Julian oscillation associated with interannual ENSO sea surface temperature anomalies. *J. Clim.*, **20**, 2659-2674.

Pokam, W.M., Djiotang, L.A.T. and Mkankam, F.K., 2012: Atmospheric water vapor transport and recycling in Equatorial Central Africa through NCEP/NCAR reanalysis data. *Clim. Dyn.*, **38**, 1715-1729.

Polcher, J. and Laval, K., 1994: The impact of African and Amazonian deforestation on tropical climate. *J. Hydrol.*, **155**, 389-405.

Potapov, P., Hansen, M.C., Laestadius, L., Turubanova, S., Yaroshenko, A., Thies, C., Smith, W., Zhuravleva, I., Komarova, A., Minnemeyer, S. and Esipova, E., 2017: The last frontiers of wilderness: Tracking loss of intact forest landscapes from 2000 to 2013. *Sci. Adv.*, **3**, 1600821.

Potapov, P., Yaroshenko, A., Turubanova, S., Dubinin, M., Laestadius, L., Thies, C., Aksenov, D., Egorov, A., Yesipova, Y., Glushkov, I. and Karpachevskiy, M., 2008: Mapping the world's intact forest landscapes by remote sensing. *Ecol. Soc.*, **13**, 51.

Prance, G.T., 2002: Species survival and carbon retention in commercially exploited tropical rainforest. *Phil. Trans. R. Soc. A*, **360**, 1777-1785.

Raghavendra, A., Zhou, L., Jiang, Y. and Hua, W., 2018: Increasing extent and intensity of thunderstorms observed over the Congo Basin from 1982 to 2016. *Atmos. Res.*, 213, 17-26.

Raghavendra, A., Zhou, L., Roundy, P.E., Jiang, Y., Milrad, S.M., Hua, W. and Xia, G., 2020: The MJO's impact on rainfall trends over the Congo rainforest. *Clim. Dyn.*, **54**, 2683-2695.

Randerson, J.T., Chen, Y., Van Der Werf, G.R., Rogers, B.M. and Morton, D.C., 2012: Global burned area and biomass burning emissions from small fires. *J. Geophys. Res. Biogeosci.*, **117**.

Reichle, R.H., Draper, C.S., Liu, Q., Girotto, M., Mahanama, S.P., Koster, R.D. and De Lannoy, G.J., 2017: Assessment of MERRA-2 land surface hydrology estimates. *J. Clim.*, **30**, 2937-2960.

Restrepo-Coupe, N., Albert, L.P., Longo, M., Baker, I., Levine, N.M., Mercado, L.M., da Araujo, A.C., Christoffersen, B.O.D., Costa, M.H., Fitzjarrald, D.R. and Galbraith, D., 2021: Understanding water and energy fluxes in the Amazonia: Lessons from an observation-model intercomparison. *Glob. Change Biol.*, **27**, 1802-1819.

Reynolds, R.W., Rayner, N.A., Smith, T.M., Stokes, D.C. and Wang, W., 2002: An improved in situ and satellite SST analysis for climate. *J. Clim.*, **15**, 1609-1625.

Riaño, D., Moreno Ruiz, J.A., Isidoro, D. and Ustin, S.L., 2007: Global spatial patterns and temporal trends of burned area between 1981 and 2000 using NOAA-NASA Pathfinder. *Glob. Change Biol.*, **13**, 40-50 .

Ridolfi, L., D'Odorico, P. and Laio, F., 2006: Effect of vegetation–water table feedbacks on the stability and resilience of plant ecosystems. *Wat. Resour. Res.*, **42**.

Rosenfeld, D., Lohmann, U., Raga, G.B., O'Dowd, C.D., Kulmala, M., Fuzzi, S., Reissell, A. and Andreae, M.O., 2008: Flood or drought: How do aerosols affect precipitation?. *Science*, **321**, 1309-1313.

Roundy, P.E., MacRitchie, K., Asuma, J. and Melino, T., 2010: Modulation of the global atmospheric circulation by combined activity in the Madden–Julian oscillation and the El Niño–Southern Oscillation during boreal winter. *J. Clim.*, **23**, 4045-4059.

Rummukainen, M., 2010: State-of-the-art with regional climate models. *Clim. Change*, **1**, 82-96.

Saatchi, S., Asefi-Najafabady, S., Malhi, Y., Aragão, L.E., Anderson, L.O., Myneni, R.B. and Nemani, R., 2013: Persistent effects of a severe drought on Amazonian forest canopy. *Proc. Natl. Acad. Sci.*, **110**, 565-570.

Saji, N.H., Goswami, B.N., Vinayachandran, P.N. and Yamagata, T., 1999: A dipole mode in the tropical Indian Ocean. *Nature*, **401**, 360-363.

Saji, N.H. and Yamagata, T., 2003a: Possible impacts of Indian Ocean dipole mode events on global climate. *Clim. Res*., **25**, 151-169.

Saji, N.H. and Yamagata, T., 2003b: Structure of SST and surface wind variability during Indian Ocean dipole mode events: COADS observations. *J. Clim*., **16**, 2735-2751.

Saleska, S.R., Didan, K., Huete, A.R. and Da Rocha, H.R., 2007: Amazon forests green-up during 2005 drought. *Science*, **318**, 612-612.

Sankaran, M., Hanan, N.P., Scholes, R.J., Ratnam, J., Augustine, D.J., Cade, B.S., Gignoux, J., Higgins, S.I., Le Roux, X., Ludwig, F. and Ardo, J., 2005: Determinants of woody cover in African savannas. *Nature*, **438**, 846-849.

Schamm, K., Ziese, M., Raykova, K., Becker, A., Finger, P., Meyer-Christoffer, A. and Schneider, U., 2015: GPCC Full Data Daily Version 1.0 at 1.0◦: Daily Land-Surface Precipitation from Rain-Gauges built on GTS-based and Historic Data. https://doi.org/10.5676/DWD_GPCC/FD_D_V1_100

Schneider, U. B. et al., 2015: GPCC full data reanalysis version 7.0 at 1.0°: monthly land-surface precipitation from rain-gauges built on GTS-based and historic data. http://dx.doi.org/10.5676/DWD_GPCC/FD_M_V7_100.

Schneider, U. B. et al., 2018: GPCC Full Data Monthly Product Version 2018 at 1.0°: Monthly Land-Surface Precipitation from Rain-Gauges built on GTS-based and Historical Data. DOI: 10.5676/DWD_GPCC/FD_M_V2018_100

Schneider, U., Finger, P., Meyer-Christoffer, A., Rustemeier, E., Ziese, M. and Becker, A., 2017: Evaluating the hydrological cycle over land using the newly-corrected precipitation climatology from the Global Precipitation Climatology Centre (GPCC). *Atmosphere*, 8, 52.

Scholes, R.J. and Archer, S.R., 1997: Tree-grass interactions in savannas. *Annu. Rev. Ecol. Syst.*, **28**, 517-544.

Schultz, M.G., Heil, A., Hoelzemann, J.J., Spessa, A., Thonicke, K., Goldammer, J.G., Held, A.C., Pereira, J.M. and van Het Bolscher, M., 2008: Global wildland fire emissions from 1960 to 2000. *Global Biogeochem. Cycles*, **22**, GB2002.

Seager, R., Naik, N. and Vecchi, G.A., 2010: Thermodynamic and dynamic mechanisms for large-scale changes in the hydrological cycle in response to global warming. *J. Clim.*, **23**, 4651-4668.

Seidel, D.J., Fu, Q., Randel, W.J. and Reichler, T.J., 2008: Widening of the tropical belt in a changing climate. *Nat. Geosci.*, **1**, 21-24.

Seneviratne, S.I., Corti, T., Davin, E.L., Hirschi, M., Jaeger, E.B., Lehner, I., Orlowsky, B. and Teuling, A.J., 2010: Investigating soil moisture–climate interactions in a changing climate: A review. *Earth-Sci. Rev.*, **99**, 125-161.

Seth, A., Rauscher, S.A., Biasutti, M., Giannini, A., Camargo, S.J. and Rojas, M., 2013: CMIP5 projected changes in the annual cycle of precipitation in monsoon regions. *J. Clim.*, **26**, 7328-7351.

Shaaban, A.A. and Roundy, P.E., 2017: OLR perspective on the Indian Ocean Dipole with application to East African precipitation. *Quart. J. Roy. Meteor. Soc.*, **143**, 1828-1843.

Shaffer, L.J., 2010: Indigenous fire use to manage savanna landscapes in southern Mozambique. *Fire Ecol.*, **6**, 43-59.

Shanahan, T.M., Overpeck, J.T., Anchukaitis, K.J., Beck, J.W., Cole, J.E., Dettman, D.L., Peck, J.A., Scholz, C.A. and King, J.W., 2009: Atlantic forcing of persistent drought in West Africa. *Science*, **324**, 377-380.

Sheil, D., 2018: Forests, atmospheric water and an uncertain future: the new biology of the global water cycle. *For. Ecos.*, **5**, 1-22.

Shimizu, M.H., Ambrizzi, T. and Liebmann, B., 2017: Extreme precipitation events and their relationship with ENSO and MJO phases over northern South America. *Int. J. Climatol.*, **37**, 2977-2989.

Shongwe, M.E., Van Oldenborgh, G.J., Van Den Hurk, B.J.J.M., De Boer, B., Coelho, C.A.S. and Van Aalst, M.K., 2009: Projected changes in mean and extreme precipitation in Africa under global warming. Part I: Southern Africa. *J. Clim.*, **22**, 3819-3837.

Shukla, J. and Mintz, Y., 1982: Influence of land-surface evapotranspiration on the earth's climate. *Science*, **215**, 1498-1501.

Solmon, F., Giorgi, F. and Liousse, C., 2006: Aerosol modelling for regional climate studies: application to anthropogenic particles and evaluation over a European/African domain. *Tellus B.*, **58**, 51-72.

Spracklen, D.V., Arnold, S.R. and Taylor, C.M., **2012**. Observations of increased tropical rainfall preceded by air passage over forests. *Nature*, **489**, 282-285.

Sridharan, V., Broad, O., Shivakumar, A., Howells, M., Boehlert, B., Groves, D.G., Rogner, H.H., Taliotis, C., Neumann, J.E., Strzepek, K.M. and Lempert, R., 2019: Resilience of the Eastern African electricity sector to climate driven changes in hydropower generation. *Nat. Commun.,* **10**, 1-9.

Staal, A., Tuinenburg, O.A., Bosmans, J.H., Holmgren, M., van Nes, E.H., Scheffer, M., Zemp, D.C. and Dekker, S.C., 2018: Forest-rainfall cascades buffer against drought across the Amazon. *Nat. Clim. Chang*e, **8**, 539-543.

Stott, P.A., Gillett, N.P., Hegerl, G.C., Karoly, D.J., Stone, D.A., Zhang, X. and Zwiers, F., 2010: Detection and attribution of climate change: a regional perspective. *Wiley Interdisciplinary Reviews: Climate Change*, **1**, 192-211.

Sun, Y., Frankenberg, C., Jung, M., Joiner, J., Guanter, L., Köhler, P. and Magney, T., 2018: Overview of Solar-Induced chlorophyll Fluorescence (SIF) from the Orbiting Carbon Observatory-2: Retrieval, cross-mission comparison, and global monitoring for GPP. *Remote Sens. Environ.*, **209**, 808-823.

Syktus, J.I. and McAlpine, C.A., 2016: More than carbon sequestration: Biophysical climate benefits of restored savanna woodlands. *Sci. Rep.*, **6**, 1-11.

Sylla, M.B., Pal, J.S., Wang, G.L. and Lawrence, P.J., 2016: Impact of land cover characterization on regional climate modeling over West Africa. *Clim. Dyn.*, **46**, 637-650.

Tan, J., Jakob, C., Rossow, W.B. and Tselioudis, G., 2015: Increases in tropical rainfall driven by changes in frequency of organized deep convection. *Nature*, **519**, 451-454.

Todd, M.C. and Washington, R., 2004: Climate variability in central equatorial Africa: Influence from the Atlantic sector. *Geophys. Res. Lett*., **31**.

Trenberth, K.E., 1999: Atmospheric moisture recycling: Role of advection and local evaporation. *J. Clim.*, **12**, 1368-1381.

Trenberth, K.E., Fasullo, J.T. and Mackaro, J., 2011: Atmospheric moisture transports from ocean to land and global energy flows in reanalyses. *J. Clim.*, **24**, 4907-4924.

Tucker, C.J., Pinzon, J.E., Brown, M.E., Slayback, D.A., Pak, E.W., Mahoney, R., Vermote, E.F. and El Saleous, N., 2005: An extended AVHRR 8-km NDVI dataset compatible with MODIS and SPOT vegetation NDVI data. *Int. J. Remote Sens.*, **26**, 4485-4498.

UNDESA., 2017: World Population Prospects -- Population Division, https://esa.un.org/unpd/wpp/Download/Standard/Population, United Nations.

van den Hurk, B.J., Viterbo, P. and Los, S.O., 2003: Impact of leaf area index seasonality on the annual land surface evaporation in a global circulation model. *J. Geophys. Res.*, **108**, 5.1-5.9.

van der Werf, G.R., Randerson, J.T., Giglio, L., Gobron, N. and Dolman, A.J., 2008: Climate controls on the variability of fires in the tropics and subtropics. *Global Biogeochem. Cycles*, **22**.

van der Werf, G.R., Randerson, J.T., Giglio, L., Collatz, G.J., Mu, M., Kasibhatla, P.S., Morton, D.C., DeFries, R.S., Jin, Y.V. and van Leeuwen, T.T., 2010: Global fire emissions and the contribution of deforestation, savanna, forest, agricultural, and peat fires (1997–2009). *Atmos. Chem. Phys.*, **10**, 11707-11735.

van der Werf, G.R., Randerson, J.T., Giglio, L., Van Leeuwen, T.T., Chen, Y., Rogers, B.M., Mu, M., Van Marle, M.J., Morton, D.C., Collatz, G.J. and Yokelson, R.J., 2017: Global fire emissions estimates during 1997–2016. *Earth Syst. Sci. Data*, **9**, 697-720.

Vecchi, G.A. and Soden, B.J., 2007: Global warming and the weakening of the tropical circulation. *J. Clim.*, **20**, 4316-4340.

Vizy, E.K. and Cook, K.H., 2012: Mid-twenty-first-century changes in extreme events over northern and tropical Africa. *J. Clim*., **25**, 5748-5767.

Wang, C., 2018: A review of ENSO theories. *Natl. Sci. Rev.*, **5**, 813-825.

Wang, G. and Alo, C.A., 2012: Changes in precipitation seasonality in West Africa predicted by RegCM3 and the impact of dynamic vegetation feedback. *Int.l J. Geophys.*, **2012**, 597205.

Wang, J., Dai, A. and Mears, C., 2016: Global water vapor trend from 1988 to 2011 and its diurnal asymmetry based on GPS, radiosonde, and microwave satellite measurements. *J. Clim.*, **29**, 5205-5222.

Wang, K. and Dickinson, R.E., 2012: A review of global terrestrial evapotranspiration: Observation, modeling, climatology, and climatic variability. *Rev. Geophys.*, **50**, RG2005.

Wang, G., Eltahir, E.A.B., Foley, J.A., Pollard, D. and Levis, S., 2004: Decadal variability of rainfall in the Sahel: results from the coupled GENESIS-IBIS atmosphere-biosphere model. *Clim. Dyn.*, **22**, 625-637.

Wang, G., Yu, M., Pal, J.S., Mei, R., Bonan, G.B., Levis, S. and Thornton, P.E., 2016: On the development of a coupled regional climate–vegetation model RCM–CLM–CN–DV and its validation in Tropical Africa. *Clim. Dyn.*, **46**, 515-539.

Washington, R., James, R., Pearce, H., Pokam, W.M. and Moufouma-Okia, W., 2013: Congo Basin rainfall climatology: can we believe the climate models? *Phil. Trans. R. Soc. B*, **368**, 20120296.

Westerling, A.L., Hidalgo, H.G., Cayan, D.R. and Swetnam, T.W., 2006: Warming and earlier spring increase western US forest wildfire activity. *Science*, **313**, 940-943.

Wheeler, M.C. and Hendon, H.H., 2004: An all-season real-time multivariate MJO index: Development of an index for monitoring and prediction. *Mon. Wea. Rev.*, **132**, 1917-1932.

White, L.J., Masudi, E.B., Ndongo, J.D., Matondo, R., Soudan-Nonault, A., Ngomanda, A., Averti, I.S., Ewango, C.E., Sonké, B. and Lewis, S.L., 2021: Congo Basin rainforest—invest US $150 million in science. *Nature*, **598**, 411-414.

Williams, C.A. and Hanan, N.P., 2011: ENSO and IOD teleconnections for African ecosystems: evidence of destructive interference between climate oscillations. *Biogeosciences*, **8**, 27-40.

Williams, E., Rothkin, K., Stevenson, D. and Boccippio, D., 2000: Global lightning variations caused by changes in thunderstorm flash rate and by changes in the number of thunderstorms. *J. Appl. Meteorol.*, **39**, 2223-2230.

Wilson, E.A., Gordon, A.L. and Kim, D., 2013: Observations of the Madden Julian oscillation during Indian Ocean dipole events. *J. Geophys. Res.: Atmos.*, **118**, 2588-2599.

Worden, J., Bowman, K., Noone, D., Beer, R., Clough, S., Eldering, A., Fisher, B., Goldman, A., Gunson, M., Herman, R. and Kulawik, S.S., 2006: Tropospheric Emission Spectrometer observations of the tropospheric HDO/H2O ratio: Estimation approach and characterization. *J. Geophys. Res.*, **111**, D16309.

Worden, J., Kulawik, S., Frankenberg, C., Payne, V., Bowman, K., Cady-Peirara, K., Wecht, K., Lee, J.E. and Noone, D., 2012: Profiles of CH 4, HDO, H 2 O, and N 2 O with improved

lower tropospheric vertical resolution from Aura TES radiances. *Atmos. Meas. Tech.*, **5**, 397-411.

Worden, J., Noone, D. and Bowman, K., 2007: Importance of rain evaporation and continental convection in the tropical water cycle. *Nature*, **445**, 528-532.

Wright, J.S., Fu, R., Worden, J.R., Chakraborty, S., Clinton, N.E., Risi, C., Sun, Y. and Yin, L., 2017: Rainforest-initiated wet season onset over the southern Amazon. *Proc. Natl. Acad. Sci.*, **114**, 8481-8486.

Wright, S.J. and Van Schaik, C.P., 1994: Light and the phenology of tropical trees. *Am. Nat.*, **143**, 192-199.

Xie, P. and Arkin, P.A., 1997: Global precipitation: A 17-year monthly analysis based on gauge observations, satellite estimates, and numerical model outputs. *Bull. Am. Meteorol. Soc.*, **78**, 2539-2558.

Xie, P., Janowiak, J.E., Arkin, P.A., Adler, R., Gruber, A., Ferraro, R., Huffman, G.J. and Curtis, S., 2003: GPCP pentad precipitation analyses: An experimental dataset based on gauge observations and satellite estimates. *J. Clim.*, **16**, 2197-2214.

Yadav, R.K., Rupa Kumar, K. and Rajeevan, M., 2009: Increasing influence of ENSO and decreasing influence of AO/NAO in the recent decades over northwest India winter precipitation. *J. Geophys. Res.: Atmos.*, **114**.

Yan, B., Mao, J., Dickinson, R.E., Thornton, P.E., Shi, X., Ricciuto, D.M., Warren, J.M. and Hoffman, F.M., 2020: Modelling tree stem‐water dynamics over an Amazonian rainforest. *Ecohydrology*, **13**, e2180.

Yang, W., Seager, R., Cane, M.A. and Lyon, B., 2015: The annual cycle of East African precipitation. *J. Clim.*, **28**, 2385-2404.

Yates, C.P., Edwards, A.C. and Russell-Smith, J., 2008: Big fires and their ecological impacts in Australian savannas: size and frequency matters. *Int. J. Wildland Fire*, **17**, 768-781.

Yoshifuji, N., Kumagai, T.O., Tanaka, K., Tanaka, N., Komatsu, H., Suzuki, M. and Tantasirin, C., 2006: Inter-annual variation in growing season length of a tropical seasonal forest in northern Thailand. *Forest Ecol. Manage.*, **229**, 333-339.

Zaitchik, B.F., 2017: Madden-Julian Oscillation impacts on tropical African precipitation. *Atmos. Res.*, **184**, 88-102.

Zakey, A.S., Solmon, F. and Giorgi, F., 2006: Implementation and testing of a desert dust module in a regional climate model. *Atmos. Chem. Phys.*, **6**, 4687-4704.

Zemp, D.C., Schleussner, C.F., Barbosa, H.M., Hirota, M., Montade, V., Sampaio, G., Staal, A., Wang-Erlandsson, L. and Rammig, A., 2017: Self-amplified Amazon forest loss due to vegetation-atmosphere feedbacks. *Nat. Commun.*, **8**, 1-10.

Zeng, N., Neelin, J.D., Lau, K.M. and Tucker, C.J., 1999: Enhancement of interdecadal climate variability in the Sahel by vegetation interaction. *Science*, **286**, 1537-1540.

Zeng, X., Shaikh, M., Dai, Y., Dickinson, R.E. and Myneni, R., 2002: Coupling of the common land model to the NCAR community climate model. *J. Clim.*, **15**, 1832-1854.

Zeng, X., Zhao, M. and Dickinson, R.E., 1998: Intercomparison of bulk aerodynamic algorithms for the computation of sea surface fluxes using TOGA COARE and TAO data. *J. Clim.*, **11**, 2628-2644.

Zhang, C., 2005: Madden-julian oscillation. *Rev. Geophys.*, **43**, RG2003.

Zhang, C. and Dong, M., 2004: Seasonality in the Madden–Julian oscillation. *J. Clim.*, **17**, 3169-3180.

Zhang, C. and Gottschalck, J., 2002: SST anomalies of ENSO and the Madden–Julian oscillation in the equatorial Pacific. *J. Clim.*, **15**, 2429-2445.

Zhou, L., Dickinson, R.E., Tian, Y., Zeng, X., Dai, Y., Yang, Z.L., Schaaf, C.B., Gao, F., Jin, Y., Strahler, A. and Myneni, R.B., 2003: Comparison of seasonal and spatial variations of albedos from Moderate-Resolution Imaging Spectroradiometer (MODIS) and Common Land Model. *J. Geophys. Res.*, **108**, 4488.

Zhou, L., Tian, Y., Myneni, R.B., Ciais, P., Saatchi, S., Liu, Y.Y., Piao, S., Chen, H., Vermote, E.F., Song, C. and Hwang, T., 2014: Widespread decline of Congo rainforest greenness in the past decade. *Nature*, **509**, 86-90.

APPENDICES

SPRINGER NATURE

Widespread increase of boreal summer dry season length over the Congo rainforest

Author: Yan Jiang et al
Publication: Nature Climate Change
Publisher: Springer Nature
Date: Jul 1, 2019

JOHN WILEY AND SONS LICENSE TERMS AND CONDITIONS

Dec 14, 2021

This Agreement between University at Albany, SUNY -- Yan Jiang ("You") and John Wiley and Sons ("John Wiley and Sons") consists of your license details and the terms and conditions provided by John Wiley and Sons and Copyright Clearance Center.

License Number	5207941186223
License date	Dec 14, 2021
Licensed Content Publisher	John Wiley and Sons
Licensed Content Publication	Geophysical Research Letters
Licensed Content Title	Increasing Influence of Indian Ocean Dipole on Precipitation Over Central Equatorial Africa
Licensed Content Author	Yan Jiang, Liming Zhou, Paul E. Roundy, et al
Licensed Content Date	Apr 26, 2021
Licensed Content Volume	48
Licensed Content Issue	8
Licensed Content Pages	11
Type of Use	Dissertation/Thesis
Requestor type	Author of this Wiley article
Format	Electronic
Portion	Full article
Will you be translating?	No
Title	Understanding Changes in Precipitation, Wildfire, and Possible Governing Impacts over Central Equatorial Africa
Institution name	University at Albany, SUNY
Expected presentation date	Jan 2022
Requestor Location	University at Albany, SUNY 1220 Washington Avenue ETEC Building, Harriman Campus Department of Atmospheric and Environmen ALBANY, NY 12206 United States Attn: University at Albany, SUNY
Publisher Tax ID	EU826007151
Total	**0.00 USD**
Terms and Conditions	

TERMS AND CONDITIONS

This copyrighted material is owned by or exclusively licensed to John Wiley & Sons, Inc. or one of its group companies (each a"Wiley Company") or handled on behalf of a society with which a Wiley Company has exclusive publishing rights in relation to a particular work (collectively "WILEY"). By clicking "accept" in connection with completing this licensing transaction, you agree that the following terms and conditions apply to this transaction (along with the billing and payment terms and conditions established by the Copyright Clearance Center Inc., ("CCC's Billing and Payment terms and conditions"), at the time that you opened your RightsLink account (these are available at any time at http://myaccount.copyright.com).

Terms and Conditions

- The materials you have requested permission to reproduce or reuse (the "Wiley Materials") are protected by copyright.
- You are hereby granted a personal, non-exclusive, non-sub licensable (on a stand-alone basis), non-transferable, worldwide, limited license to reproduce the Wiley Materials for the purpose specified in the licensing process. This license, **and any**